metals

MDPI

Review

Advancements in Metal Processing Additive Technologies: Selective Laser Melting (SLM)

Neetesh Soni *, Gilda Renna and Paola Leo

Department of Engineering for Innovation, University of Salento, via per Monteroni di Lecce, 73100 Lecce, Italy; gilda.renna@unisalento.it (G.R.); paola.leo@unisalento.it (P.L.)
* Correspondence: neetesh.soni@unisalento.it

Abstract: Nowadays, the use of metal processing additive technologies is a rapidly growing field in the manufacturing industry. These technologies, such as metal 3D printing (also known as additive manufacturing) and laser cladding, allow for the production of complex geometries and intricate designs that would be impossible with traditional manufacturing methods. They also offer the ability to create parts with customized properties, such as improved strength, wear resistance, and corrosion resistance. In other words, these technologies have the potential to revolutionize the way we design and produce products, reducing costs and increasing efficiency to improve product quality and functionality. One of the significant advantages of these metal processing additive technologies is a reduction in waste and environmental impact. However, there are also some challenges associated with these technologies. One of the main challenges is the cost of equipment and materials, which can be prohibitively expensive for small businesses and individuals. Additionally, the quality of parts produced with these technologies can be affected by factors such as printing speed, temperature, and post-processing methods. This review article aims to contribute to a deep understanding of the processing, properties, and applications of ferrous and non-ferrous alloys in the context of SLM to assist readers in obtaining high-quality AM components. Simultaneously, it emphasizes the importance of further research, optimization, and cost-effective approaches to promote the broader adoption of SLM technology in the industry.

Keywords: 3D additive manufacturing; selective laser melting (SLM); metallic alloys; ferrous and non-ferrous alloys

Citation: Soni, N.; Renna, G.; Leo, P. Advancements in Metal Processing Additive Technologies: Selective Laser Melting (SLM). *Metals* **2024**, *14*, 1081. https://doi.org/10.3390/met14091081

Academic Editor: Zhengyi Jiang

Received: 29 July 2024
Revised: 22 August 2024
Accepted: 9 September 2024
Published: 21 September 2024

1. Introduction

In the last decade, one of the most critical advances in industrial research is the development of new manufacturing technologies for producing lightweight, sustainable components that prioritize low waste, weight reduction, and proper design concepts [1–3]. Although cutting-edge high-strength structures and metallic alloy materials have made significant progress for use in core domains such as heavy automobiles (tractors and high-speed car bodies) [4–6], aviation (aerospace structural applications) [7–9], the marine sector (ship propellers and turbine parts) [10–13], building construction (structural components such as non-joint large beams, without support shafts, pillars) [14–17], and medical devices and bio-metallics (artificial parts such as the knee, hip cupping, and elbow joint) [18–28] there is still a need to explore more efficient and effective manufacturing methods. The use of 3D additive manufacturing processes is suitable for processing various materials [29–31].

Among these, selective laser melting (SLM) stands out for its exceptional versatility, the wide range of materials used, and the high density of the parts produced (close to 100%). This technology fulfills the stringent criteria set by today's standards, including waste reduction and environmental sustainability, while delivering exceptional accuracy and quality. The economic importance of saving fuels and promoting green energy adoption

has garnered attention from academic researchers and industry professionals, leading to the widespread adoption of SLM technology in numerous countries.

To date, SLM is used to deposit a wide variety of metal alloys, such as aluminum alloys, magnesium alloys, titanium alloys, steel, etc. Generally, due to their low density and high strength/weight ratio, aluminum alloys are used for all those applications where weight reduction is essential. The existing literature highlights numerous mechanical advantages of using Al–Mg-based alloys in SLM compared with their wrought counterparts. These advantages include higher damping [32–34], increased strength [35], superior corrosion resistance [36,37], and improved creep resistance [38–40]. However, alongside these benefits, there are a few drawbacks to consider when using Al alloys in SLM. These drawbacks include the presence of pinholes, susceptibility to hot cracking, and potential influences on chemical composition.

Other studies have indicated a notable interest in SLM-processed aluminum, steel, and titanium alloy processing due to their ability to encompass various structural and mechanical characteristics [41], such as tensile strength, hardness, and impact energy. Furthermore, utilizing lattice structures in SLM processing enables the fulfillment of weight–ratio requirements, further improving the application of steel and titanium alloys [41–45]. These alloys have extensive applications in the aerospace and biomedical industries [46]. Also, the Ti alloys are used in various constructions and structural applications to replace solid parts using SLM-processed components with appropriate lattice structures [47,48]. Despite the notable drawbacks of higher cost and limited usability in biomedical applications, addressing the efficiency and sustainability of the components' performance and properties can effectively mitigate cost concerns and ultimately enhance overall cost-effectiveness.

In the competition among materials for additive manufacturing (AM) using 3D melting-based processes, steel alloys have emerged as strong contenders due to their mechanical and metallurgical properties, which are relatively similar to titanium alloys. A significant advantage of steel alloys is their lower cost compared to titanium alloys, although they are slightly more expensive than aluminum alloys. However, steel alloys suffer from certain drawbacks, namely anisotropy, surface roughness, and porosity, which must be addressed and improved for optimal performance in AM applications. Applications and comparisons among aluminum, steel, and titanium alloys are shown in Table 1.

Aluminum, titanium, and steel alloys play a crucial role in the global manufacturing industries due to their wide range of applications [46,49–51]. G. Victor showed that steel alloys are extensively used in aerospace and aircraft manufacturing, comprising 6–8% in the Airbus A380 and Boeing 787 and approximately 10–12% in other parts [51]. However, aluminum and titanium alloys also have wide-ranging applications in various sectors. These alloys are employed in various industries such as automotive, marine, oil and gas industries, aerospace [52–54], missile manufacturing [54–56], marine (structural) applications [57,58], and heat exchangers [54–62]. With respect to aluminum alloys, the titanium alloys are characterized by higher corrosion and mechanical properties and by a better density ratio [57,63–66].

One key factor hindering extensive research in SLM applications for metals is the high cost associated with equipment. However, considering the promising outcomes of the SLM process, it is essential to overcome these cost-related challenges to encourage more comprehensive exploration and development in this field. The SLM literature has seen significant quantitative work published in various journals in the last ten years. For instance, analyzed the microstructural and mechanical characteristics of AlSi10Mg alloys produced through SLM. similarly explored these alloys—such as argon and nitrogen—in diverse environments, aiming to comprehend the tensile properties of the produced components. studied the corrosion properties of AlSi10Mg alloys, employing equal channel angular processing techniques exclusively within the SLM manufacturing approach. In another study, utilized the pulsed-SLM process to examine AlSi10Mg alloys, shedding light on their microstructural and mechanical attributes, along with investigating the impact of laser density [67–70].

In recent years, there has been a dramatic increase in approved investments by governments and their respective departments worldwide to actively promote additive manufacturing for the 3D printing process. The European Union (EU) is a major proponent of this technology [71–75]. Indeed, the manufacturing goods sector receives an impressive annual budget of €421 billion [76–78]. The EU has established itself as a leading global platform for the manufacturing sector, particularly in Industry 4.0 and 5.0, encompassing the latest advancements in additive manufacturing, especially the lightweight sustainable structure of the components [79–81].

Moreover, worldwide initiatives focus on reducing CO_2 emissions and promoting green innovation, with manufacturing sectors leading in achieving these goals. This involves leveraging technologies such as robotics [82,83], artificial intelligence [84,85], high-performance computing programming [86,87], simulations, and 3D–4D printing [88–90], among others. These efforts aim to drive efficient outcomes and pave the way for sustainable manufacturing practices.

This review paper provides a comprehensive overview of the SLM process for machining ferrous and non-ferrous alloys. More specifically, the principal results related to process parameters, mechanical properties, microstructural properties, corrosion analysis, and mathematical modeling are reported to provide an overview of the achievements and, simultaneously, to focus on what needs improvement.

Figure 1 provides an overview of the objectives of this study, which are presented in distinct circles. The first circle concerns the technology under study, particularly the SLM process. The second circle highlights the study's focus on specific metals and alloys. Finally, the third and fourth circles encompass the entire review content, capturing all the relevant aspects discussed in the study.

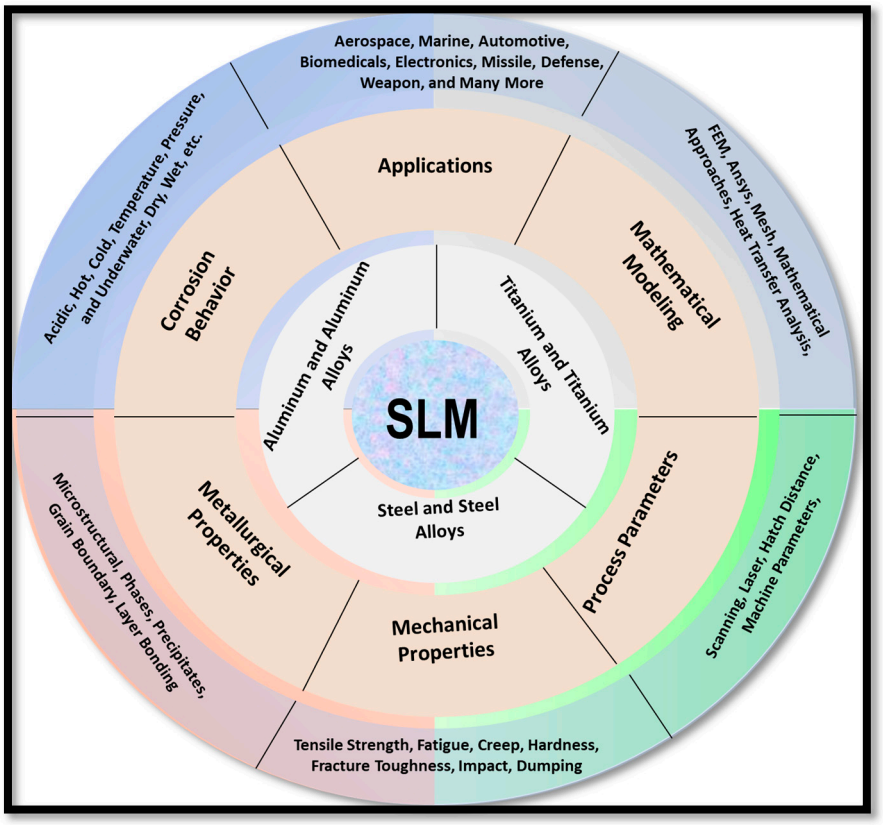

Figure 1. Schematic of the objectives of this review.

Table 1. The advantages and applications of the aluminum, steel, and titanium alloys.

Alloys	AM Process	Area of Applications	Limitations	Advantages	Comments	Ref.
Aluminum	3D SLM process, building direction can be modified as per the consideration of the most appropriate strategy	Thermal insulation, Aircraft wings, Weapon manufacturing, Electrical appliance, Shock damping/Absorption, Storage tanks, Acoustic absorption, Gas turbine engine components, Catalyst support, Automotive applications, and Biomedical implants, Structural, Robotics, Engine blocks	-Limitations of Material selection under the SLM process. -Cost is higher. -Balling effect during the process. -Vertical building is stronger than the horizontal part. -Powder is costly. -Process parameters need more trial experiments.	-Easy to deform with better density. Number of part reduction. Cost reduction for the easy-to-make complex geometry. Lattice structure with reducing 50–60% of the total weight of components.	Need additional time to manufacture supporting structure.	[5,6,54,91–93]
Steel	3D SLM process, building parts can be modified as per the consideration of the scanning scheme	Pump casings, Heat exchanger, Valves impellers, Biomedical implantation, Gears, Engine parts, Aviation industries,				[37,52,94–96]
Titanium	3D SLM process, Manufacturing parts, and Process parameters can vary as per the systematically articulated suitable parameters	Biomedical implant, Space crafts, Automotive, High-speed cars, Structural, Electronics, Robotics,				[43,46,53,97–101]

Historical Background of Metal AM Technologies

Additive manufacturing has had a long journey to develop better-quality products from various methods and techniques. Stereolithography (SLA) [102,103], electron beam melting (EBM) [104–106], direct metal laser sintering (DMLS) [107,108], selective laser melting [109,110], selective laser sintering [111,112], fused deposition modelling (FDM) [113,114], and 3-dimensional rapid prototyping technology (3D–RPT) [115,116] belong to additive manufacturing techniques [117]. Compared to alternative 3D additive manufacturing processes, SLM offers advantages in ease of implementation, cost-effectiveness, and reduced production time.

The first patent filed by Carl R. Deckard in 1986, followed by two others later, explained what is now known as selective laser melting/sintering (SLM/S) [118,119]. Also, in his first patent, C.R. Deckard explains that this method is very advantageous for metals, polymers, and ceramics in powder form [120–122]. The SLM process is well-suited for producing complex geometries and offers several advantages. However, it is crucial to consider various factors that can significantly influence the mechanical and microstructural properties of the processed alloy powder. These factors can be categorized into two main groups: those necessary to meet the requirements of the specific machine being used and those related to the selection and optimization of process parameters [123,124]. Improper selection or optimization of process parameters can lead to various issues in the SLM process. These issues include the formation of cracks, unmelted powder particles, powder segregation [125–127], and the formation of pores in the final parts [128,129]. These defects can harm the mechanical integrity and quality of the produced components. In addition to process parameters, implementing suitable thermal cycles, such as pre-annealing, post-heating, and aging, has been explored to enhance the properties of SLM further processed parts. These thermal treatments can help alleviate residual stresses, improve the microstructure, and enhance the mechanical properties of the final components [130,131].

Moreover, SLM has proved particularly suitable in medical and bioengineering, supplying the opportunity to customize body parts. Most of the produced parts belong to orthopedic surgery, such as the inter-body fusion cage [132–134], scapula prosthesis [91,135], hip prosthesis [136–141], cranial prosthesis [141–143], knee–arms prosthesis [24,144,145], acetabular cup [146–148], and dental implant [149–154]. SLM can form these real-time functional parts by adjusting all the necessary parameters and properties to be safe and lasting for the human body, avoiding the risk of repeated surgeries. Many doctors, researchers, and scientists have been devoted to improving artificial parts' properties and their mutual correlation with the human body [155].

The literature review of the past decade reveals that there have been over 10,000 articles published in respective journals, as evidenced by data from the Web of Science. These articles encompass a wide range of quantitative research, including reviews, research papers, chapters, and patents, all focused on SLM. Figure 2 displays the publication trends of articles on aluminum, steel, and titanium alloys specifically in the last ten years and the cumulative articles related to manufacturing and AM-based research from 1988 to 2022, covering 35 years. The data obtained from a Web of Science search indicate that approximately 9,500 articles have been published on SLM during this period. The data shown in Figure 2 indicate significant growth, particularly in the last three or four years, reflecting a growing interest and increased research activity in this area. This upward trend suggests the potential for surpassing the previous records of additive manufacturing (AM). Many research groups around the world are focused on the AM technique. In the European Union, most industries have partnered with research organizations focused on new advanced and sustainable techniques to make additive manufacturing autonomous without resorting to time- and cost-consuming machining or welding (metal joining) methods.

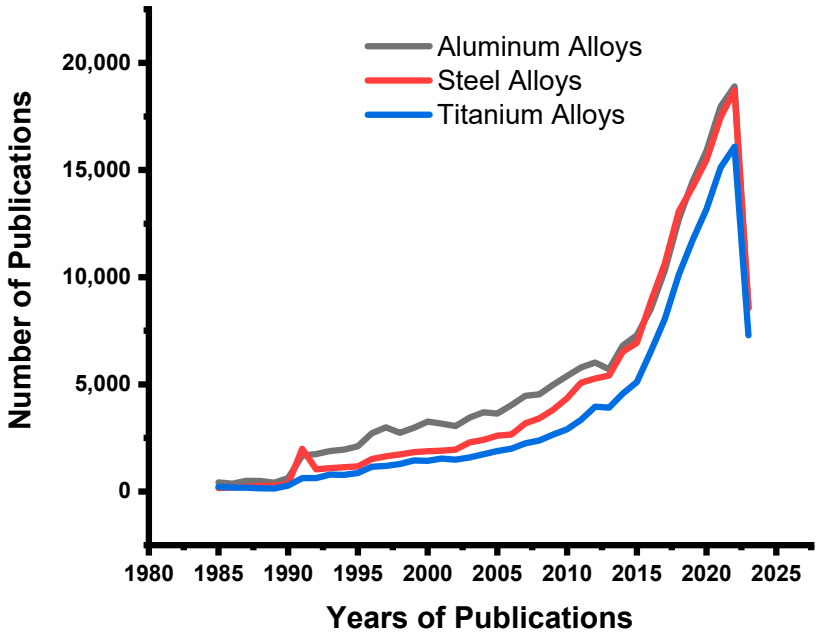

Figure 2. Publications on AM employing various alloys over the preceding decades (source of data: Web of Science, 23 July 2023).

2. Selective Laser Melting Process and Powder

Generally, the SLM process focuses on low-temperature melting materials to achieve better surface quality and near-to-net shape of the desired component [156,157]. Recent research highlights how SLM technology can produce extremely smooth surfaces and complex structures in titanium and steel alloys [94,95].

However, it is necessary to understand laser–powder interactions at low laser energy ranges to process metal materials with SLM processing.

Naveed Ahmed asserts that the SLM process effectively overcomes some of the limitations associated with the use of metal powders during component production [158]. However, the main challenges in this process arise during the transition from the liquid phase to solidification, where rapid cooling and the potential formation of brittle intermetallic compounds occur. These factors can contribute to the appearance of cracks and various defects in the final product [159–161].

Significant efforts are being made to improve components' mechanical and metallurgical properties through the SLM manufacturing of hybrid structures. It involves using different powder compositions to achieve the desired results. Combining multiple materials with different properties allows you to create hybrid components with superior characteristics compared to those made with a single material. However, in these cases, it is of fundamental importance to have an in-depth knowledge of the behavior and characteristics of the powders used, as well as to comply with the standards and references established when mixing the compositions.

Each metal powder has its own time transition period from the liquid to the solid phase. Therefore, compatibility and proper mixing of powder compositions must be carefully verified and validated to ensure success in manufacturing components with optimal mechanical properties. It is important to note that issues such as powder segregation or void spaces between particles can cause significant defects in the final components [162,163].

Figure 3 shows the various factors that impact the quality of products processed by SLM. These factors include [164,165]:

- Requirements of powder material properties, such as size, shape, composition, and melting range;
- Machine parameters, including inert gas atmosphere, chamber temperature, axis configuration, and initial laser heat time;

- Laser and scanning parameters such as scan speed, hatching time, spacing, spot size, and layer thickness significantly influence the machine's operation;
- Pre- and post-processing methods include preheating and residual stress-relieving techniques;
- The knowledge and experience of the operator;
- The interconnection between powder and temperature. Inappropriate matching of a low-melting powder with a high operating temperature can lead to improper execution of desired commands.

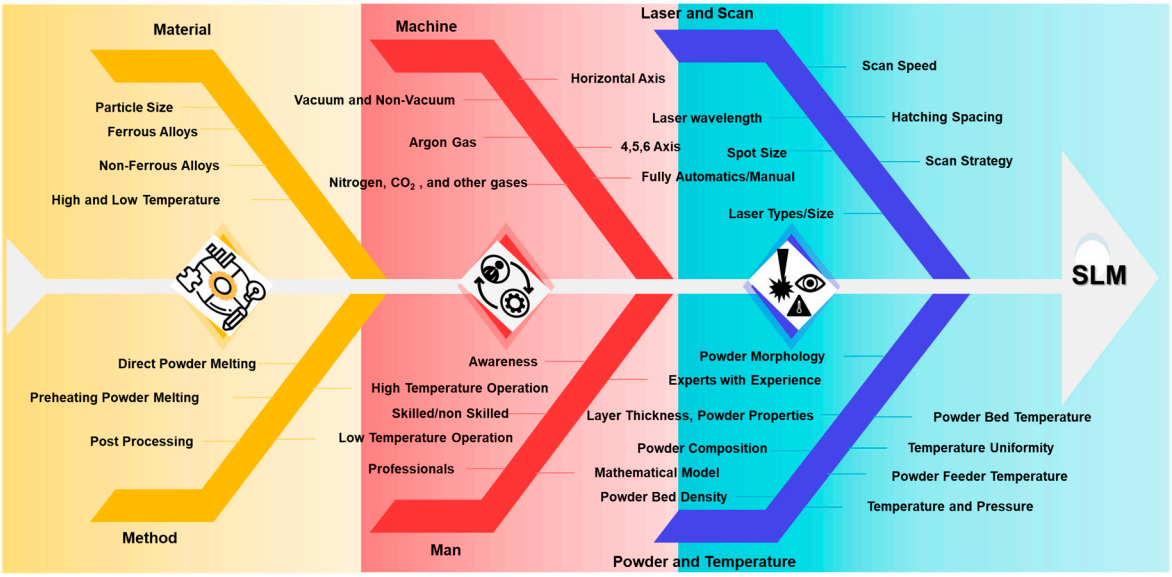

Figure 3. Fishbone diagram illustrating the causal factors and their effects on the quality of components manufactured through SLM.

Therefore, understanding and appropriately controlling these factors are essential for achieving the desired outcomes in the SLM process. Today, approaches such as the Taguchi method, response surface methodology (RSM), and trial-and-error methods help optimize process parameters and better understand the factors that influence the production of components with desired properties [166,167].

The Taguchi method is a design strategy that allows you to identify and optimize the most significant process factors, minimizing the effect of unwanted variations. Response surface methodology, on the other hand, is a statistical technique that helps understand the relationship between process factors and desired responses, allowing the optimal combination of parameters to be found. Furthermore, trial-and-error methods have proved invaluable in understanding the causal factors affecting the manufacturing process. Process parameters can be fine-tuned through iteration, result analysis, and targeted modifications to improve the final components' properties.

2.1. Procedure Description

The SLM can form solid and hollow models or prototypes with complex geometry, metallic and non-metallic, with different lattice structures. Currently, the focus on modifying machine characteristics and parameters is very high in the field of SLM. Previous literature indicates that some companies producing such equipment managed to meet the desired requirements of users. These changes aim to improve the machines' functionality and performance to meet user expectations better. The SLM machine is schematically represented in Figure 4. A layer of powder with a thickness of approximately 20–100 µm is deposited onto a build platform using a recoater with a ceramic, steel, or rubber blade, depending on the powder type and the manufactured component [168]. The fusion of the powders is achieved using a high-power laser beam guided in the x–y direction by

appropriate galvanometric mirrors. Most SLM systems currently available on the market are equipped with active fiber laser sources that emit laser radiation in the near-infrared (approximately 1 µm), typically in a continuous wave mode. Two main techniques are used for powder melting: continuous and modulated laser scanning. The laser energy is continuously released in the first case, while sequential exposures are used in the second case.

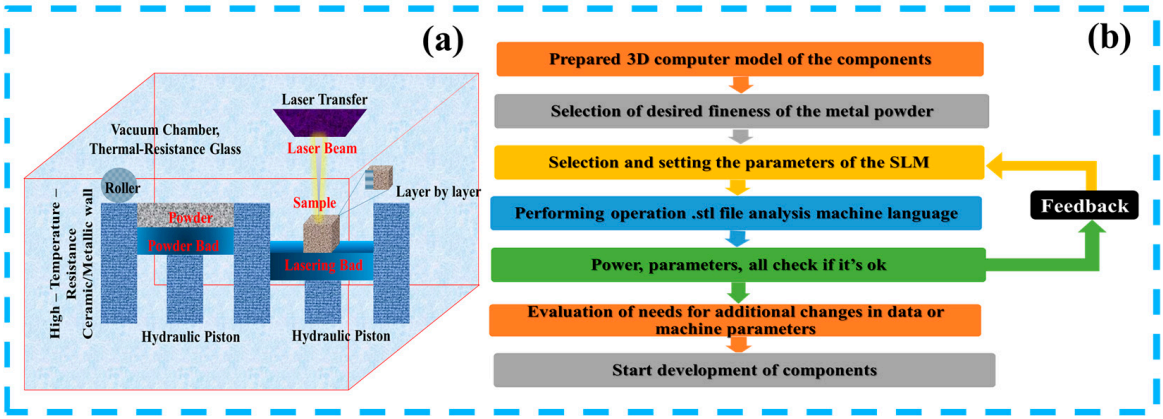

Figure 4. Complete SLM process: (**a**) schematization of the laser layering process using a laser beam and (**b**) steps from software analysis to component completion.

In the SLM process, laser powers generally range from >50 W to 400 W, with the peak power reaching 1 kW. The spot size varies between 50 µm and 200 µm depending on the process conditions. After completing each layer, the build platform is lowered to allow the deposition of the next powder layer. At the end of the process, the unfused powder is removed from the component and reused in subsequent jobs. SLM technology involves using supports to sustain the component during its fabrication. These supports must be removed at the end of the process to avoid damaging the surface. One crucial factor to consider during the SLM process is the oxygen gas in the chamber. Oxidation can occur when oxygen reacts with the powder particles, potentially altering the material properties. To inhibit oxidation, numerous contemporary SLM machines incorporate CO_2, argon, and nitrogen gases within the chamber during processing to establish a controlled environment devoid of oxygen. This vacuum environment helps to prevent oxidation and maintain the integrity of the materials being processed [165,169]. However, it is important to note that the influence of oxygen on materials can be complex and material-dependent. In some cases, oxygen may act as a surface tension reducer, benefiting certain materials and specific applications [170,171].

The simple strategic steps for this process are shown in Figure 4b. In research and design (R & D), advanced software tools such as FEM, Ansys, Matlab, and various design software, including AutoCAD, ProE, SolidWorks, and Catia, are utilized to pre-analyze data and values. These software applications enable the generation of digital models and facilitate the design of components, which are then converted into the widely used STL (standard tessellation language) file format.

The much research focuses on the quality of the starting material (metal powders) and the pre-deposition modifications. Metal powders generally have residual stress that requires preheating to an annealing temperature consistent with the melting temperature range. Preheating can be carried out inside the processing chamber to minimize thermal variations. It helps maintain a thermally stable environment and minimizes temperature differences between the preheated powders and the deposition area. This strategy helps ensure the consistency and quality of the merger process [172–174].

2.2. Process Parameters of SLM

Process parameters are crucial for the successful operation of any automated or manual machine, which also applies to SLM. So, the parameters used in SLM machines play a significant role in achieving desired results. Various parameters are involved in the SLM process, such as laser power, scanning speed, hatch spacing, layer thickness, and powder bed temperature. These parameters determine the energy input, material deposition rate, and overall quality of the printed component. Finding the optimal combination of these parameters is essential for achieving the desired structural integrity, dimensional accuracy, and surface finish of the 3D-printed part. In addition, the processing parameters used in the SLM machine play a crucial role in controlling/minimizing undesirable effects such as oxidation. Several additive manufacturing standards have been established to ensure consistency and quality in the SLM process. Notable standards include ASTM/ISO 52900, which provides guidelines for the layer-by-layer deposition of metallic and non-metallic materials to build 3D components. These standards define testing methods, material requirements, and best practices to ensure reliable and consistent additive manufacturing processes. By adhering to these standards and carefully controlling the process parameters, manufacturers can achieve high-quality and reliable results in SLM, ensuring the production of functional and durable 3D-printed components [175–177].

3. SLM for Non-Ferrous and Ferrous Alloys

From a metallurgical point of view, AM is exciting because it can significantly influence the microstructural properties and, consequently, the mechanical properties of metallic components. AM processes, such as selective laser sintering (SLS), work at the metal powder or filament level and allow to control the distribution of atoms in materials. Moreover, the high cooling rates during the SLM process (in the order of 10^6 °C/s up to 10^8 °C/s) lead to the formation of very fine microstructures. The solidification process involved in SLM is like fusion welding. However, the critical difference lies in the composition of the materials used. In fusion welding, the base metal and filler metal can be similar but not identical.

On the other hand, in the SLM process, the underlying layer and the new layer of metal powder to be melted have the same composition. Like fusion welding, laser energy causes partial re-melting of the underlying layer to ensure a solid metallurgical bond in the SLM process. There is no barrier to nucleation in both fusion welding and the SLM process, and solidification occurs spontaneously through epitaxial growth. The growth occurs thanks to the arrangement of the atoms in the liquid phase on the existing crystalline substrate. After the initiation of the solidification process at the solid–liquid interface, growth continues towards the center of the melt pool, following two criteria. The solid grows in the direction of the thermal gradient, i.e., perpendicular to the solid–liquid interface, as shown in Figure 5.

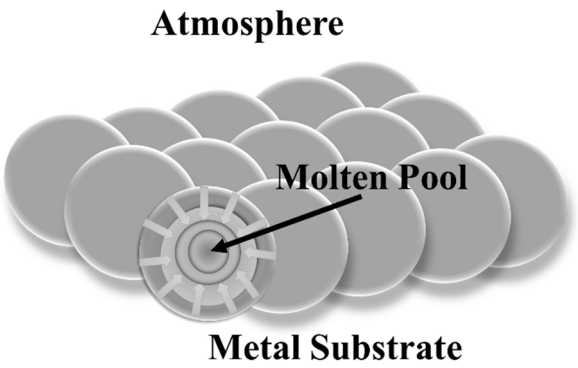

Figure 5. Example of melt pool solidification during the SLM process—Adapted from Ref. [160].

Moreover, growth occurs along the crystallographic direction that offers the least resistance. This phenomenon is referred to as preferential growth. The microstructure obtained through SLM processing is subject to variation based on the laser's energy density and the duration of the interaction between the metal powder and the laser beam. These factors play a role in shaping the geometry of the molten metal pool, ultimately determining the resulting type of microstructure [160].

Solidification is a function of a temperature gradient expressed as $G = dT/dx$, where dT represents the temperature variation along the x direction. The solidification rate is defined as $R = dx/dt$, where dx represents the position variation over time t.

The cooling rate is given by $dT/dt = G \times R$, which is the product of the temperature gradient and the solidification rate. It has been observed that an increase in the ratio between the temperature gradient and the solidification rate (G/R) influences the type of solidification, transitioning from dendritic to cellular and finally to planar. On the other hand, a high cooling rate promotes the formation of smaller grain sizes. The parameters G/R and $G \times R$, therefore, respectively, control the type of microstructure and the grain size in the solidified material [178].

Therefore, the microstructural properties of materials, such as grain size, crystal orientation, and the presence of specific phases, can be tuned and controlled much more precisely through AM. This control of the microstructural properties offers the opportunity to obtain parts with specific and optimized characteristics for particular applications. For example, obtaining parts with high strength and hardness or high corrosion resistance is possible. However, as previously mentioned, it is essential to remember that optimizing microstructural properties requires a thorough understanding of process parameters, the alloys used, and the interaction between the manufacturing technology and the material itself [179–181]. In general, microstructural analysis plays a role of fundamental importance in the study of SLM parts. Advanced characterization techniques, such as scanning electron microscopy (SEM), TEM (transmission electron microscopy), and field emission scanning electron microscopy (FESEM), provide valuable information on the morphology and structure of grains within SLM parts. The solidification mechanism that characterizes the SLM process is comparable to that observed in fusion welding. However, there are some critical differences between the two processes. In fusion welding, the base metal and filler metal may have similar but not necessarily identical compositions. In the case of SLM, on the other hand, the underlying layer of molten material and the new layer of metal powder to be melted have the same composition.

Furthermore, it should be noted that one of the advantages of using the SLM machining technique to produce parts is the ability to adjust their mechanical properties according to the desired application. Furthermore, post-processing techniques like heat treatment or surface finishing may further enhance the mechanical properties of SLM-processed components, depending on the specific application requirements. The mechanical properties of any component serve as evidence of its efficiency and overall quality, going beyond mere samples produced through SLM machining.

The different mechanical properties of SLM components, such as tensile strength, elongation, and micro-hardness, and microstructural characteristics, such as grain distribution and phases formed, play a significant role in the applications of the component. In turn, these properties and the corrosion behavior of the components are closely related to the orientation of the material lattices and the process parameters used. At this point, mathematical simulation modeling proved to be a valid tool for providing the relative expected results for each modification of the product/component.

The following sections highlight the mechanical, microstructural, and corrosion behavior of SLM parts processed with different alloys.

3.1. SLM Parts in Aluminum Alloys

In the past 10 years, there has been a significant demand for lightweight applications, leading to the development and processing of several series of aluminum alloys using SLM technology. Aluminum alloys are particularly suitable for lightweight applications due to their low density and good mechanical properties. Various series of aluminum alloys have been processed using SLM, such as the 2xxx, 5xxx, 6xxx, and 7xxx series. These alloys offer a combination of strength, ductility, and corrosion resistance, making them suitable for various applications. However, among the Al–Si alloys (6xxx series), the most used by aerospace industries is the AlSi10Mg alloy.

Table 2 summarizes the process parameters and highlights the strategies used to process this type of alloy. The existing literature analysis has shown that components with different mechanical and metallurgical properties are obtained by varying the process parameters. Moreover, it has been found that to obtain high-performance components, it is also essential to make an accurate choice on the pre-definition parameters of the powders, such as the size of the particles, composition, melting temperature range, and thermal conductivity.

It is easier to build aluminum alloy SLM components using high laser energy. showed that laser energy mainly influences sample density. Furthermore, the microsecond laser on the powder particles is part of the primary process parameters to be controlled to obtain parts with a low percentage of porosity [92,93,182,183]. Most authors perform a preheating of the component particles, receiving a residual stress-free powder [184]. Conversely, heat treatments are carried out after deposition in other works, such as annealing and aging. These post-deposition treatments have resulted in considerable changes in mechanical properties due to precipitation formation and hardening [185–187].

Table 2. Process parameters considered by researchers during SLM processing for aluminum alloys.

Powder	Laser Beam Diameters [μm]	Laser Power [W]	Layer Thickness [μm]	Hatch Distance [μm]	Laser Type	Scan Speed mm/s	Remarks	Ref.
AlSi10Mg	50–250	100–400	40	112	Ytterbium fiber laser (ʎ = 1070 nm)	600–1400	Under nitrogen atmosphere % 0.4 O_2	[188]
AlSi10Mg	-	240–320	30	80–160	Ytterbium fiber laser 400 W	500–1800	Laser linear densities 90.64–104.16 J/mm^3	[189]
AlSi10Mg	100	370	40	150	Ytterbium fiber laser 400 W	1000–1900	99.9% Argon atmosphere, and E = 32.5–61.7 J/mm^3	[190]
AlSi10Mg +TiB2, TiC	-	270	30	110	Ytterbium-fiber laser 400 W	1600	Without preheating treatment on the powder, the hatch angle is considered 67°	[191]
AlSi10Mg	-	370	30	190	-	1300	Preheating at 80 °C, the process under Argon atmosphere, and 0.1% O_2.	[192]
AlSi10Mg	-	291–459	30	43–77	Fiber laser 200 W	1395–2405	T6 heat treatment cycle and 520 °C for 1 h and 180 °C for 12 h	[193]
AlSi10Mg	75	220–280	30	90	Fiber laser P = 300 W–λ = 1070 nm	800–2000	Argon atmosphere flow with oxygen content < 200 ppm to avoid oxidation	[194]
AlSi10Mg	-	370	30	160–180	Ytterbium-fiber laser 400 W	1161–573	Volume energy density 49–59 J/mm^3, argon atmosphere flow with oxygen content < 100 ppm to avoid oxidation.	[195]
AlSi10Mg	-	300	50	150	Ytterbium-fiber laser 400 W	200	Preheating at 160 °C, with checkerboard scanning strategy, basic block supporting structure	[196]
AlSi10Mg	-	300–400	30	130	laser power of 400 W	1800	Volumetric energy density 32.05–128.21 J/mm^3, preheating at 150 °C, argon atmosphere flow with oxygen content < 500 ppm to avoid oxidation	[197]
AlSi10Mg	80	200–240	30	100	Yb-fiber laser; 400 W	3300–1900	Forming platform temperature 125 °C, energy density 2.0–4.2 J/mm^3	[198]

Table 2. *Cont.*

Powder	Laser Beam Diameters [μm]	Laser Power [W]	Layer Thickness [μm]	Hatch Distance [μm]	Laser Type	Scan Speed mm/s	Remarks	Ref.
AlSi10Mg	-	300	30	150	Yb-fiber laser; 400 W	1700	They were constructed at 0°,45°, and 90° angles, annealing post-heating treatment of 270 °C for 2 h	[199]
AlSi10Mg	-	400	30	170	Yb-fiber laser; 400 W	1300	-	[200]
AlSi10Mg	55	175	20–30	70	Yb-fiber laser; 400 W	800–1025	Pretreatment at 60 °C for 3 h, nitrogen chamber with O_2 content (0.1 vol.%) and energy density 71–137 J/mm^3, scan strategy followed by three angles 0°, 45°, and 90° SS1, SS2, SS3, respectively	[201]
AlSi10Mg	-	300	40	190	Yb-fiber laser; 400 W	1200	Argon atmosphere flow with oxygen content < 200 ppm to avoid oxidation, preheating at 150 °C	[202]

3.1.1. Microstructural Morphology of SLM Parts in Al Alloys

When analyzing SLM-processed specimens, the longitudinal and transverse sections are typically examined to assess the presence of any micro-defects. Although scanning strategies such as crossed, square, circular, alternating, and concentric lines present particularly dense microstructures from a macroscopic point of view, they are not necessarily free from defects and micropores. Consequently, to obtain more detailed information on these aspects, techniques such as SEM (scanning electron microscopy) and optical microscopic (OM) analysis are used [203,204]. Moreover, as mentioned above, the analyses conducted at higher magnifications through SEM and OM clearly define the features of the formed microstructure. Some standard features include lamellae, needle-like structures, and precipitates of different alloying elements, varying significantly depending on the processing conditions and alloying elements present. Each of these microstructural features will impact the component properties differently. For example, the lamellar microstructures improve the strength and toughness of materials by hindering the propagation of cracks, and the needle-like structures help improve the strength along specific crystallographic directions. In contrast, the precipitates of different alloying elements increase the hardness of the component as they create barriers that hinder the movement of the dislocations. Moreover, the presence of finely distributed precipitates leads to an increase in corrosion resistance [180,205].

Figure 6a–d offers a complete overview of the defects that generally form in Al alloy samples produced by SLM. It is worth pointing out that these defects are not limited to this specific type of Al alloys, but they can occur in various SLM parts in metal materials such as steel and titanium alloys. Generally, defect formation is influenced by several factors, including process parameters such as scanning strategy, hatch distance, and laser exposure time. Furthermore, laser defocusing has also been observed to contribute to their formation. The micrographic analysis allows us to reveal the characteristics originating from improper control of the fusion and cooling of the powder particles. The defects mainly encountered are irregular voids, gas pores, balling phenomena, and rough surface finish, spatter, and keyhole pores [206–208]. The irregular voids (Figure 6a) have random shapes and indicate weak bonding between different layers of molten metal within the printed part. The gas pores are the smallest, typically round, and appear like Figure 6b. They form when inert argon gas (used during printing) and leftover gas trapped in the metal powder get trapped inside the molten metal as it solidifies too quickly. While keyhole pores are larger round voids (usually less than 100 micrometers) formed when metal vaporizes in the laser's molten pool. This creates a vapor cavity that can collapse, leaving a void. Slow laser speeds make these cases more likely. Finally, the balling phenomenon (Figure 6c) refers to a situation in which individual dust particles do not completely dissolve and fuse with the substrate but instead form small spherical spheres on the surface. The presence of these defects weakens SLM parts, reducing their tensile strength, fatigue strength, and overall integrity. Furthermore, it is noteworthy that, mainly in the areas where the Al–Si interdendritic lamellar eutectic structure occurs, the formation of microcracks during solidification is observed (Figure 6d). It is known that in materials with a high thermal expansion coefficient, i.e., Al alloys, excessive segregation of solutes during solidification, such as the Si phase in the AlSi10Mg alloy, can increase the susceptibility to solidification cracking of the material, especially in the presence of high residual stresses. This phenomenon is common in parts fabricated using DMLS, as the material experiences extremely high cooling rates [208].

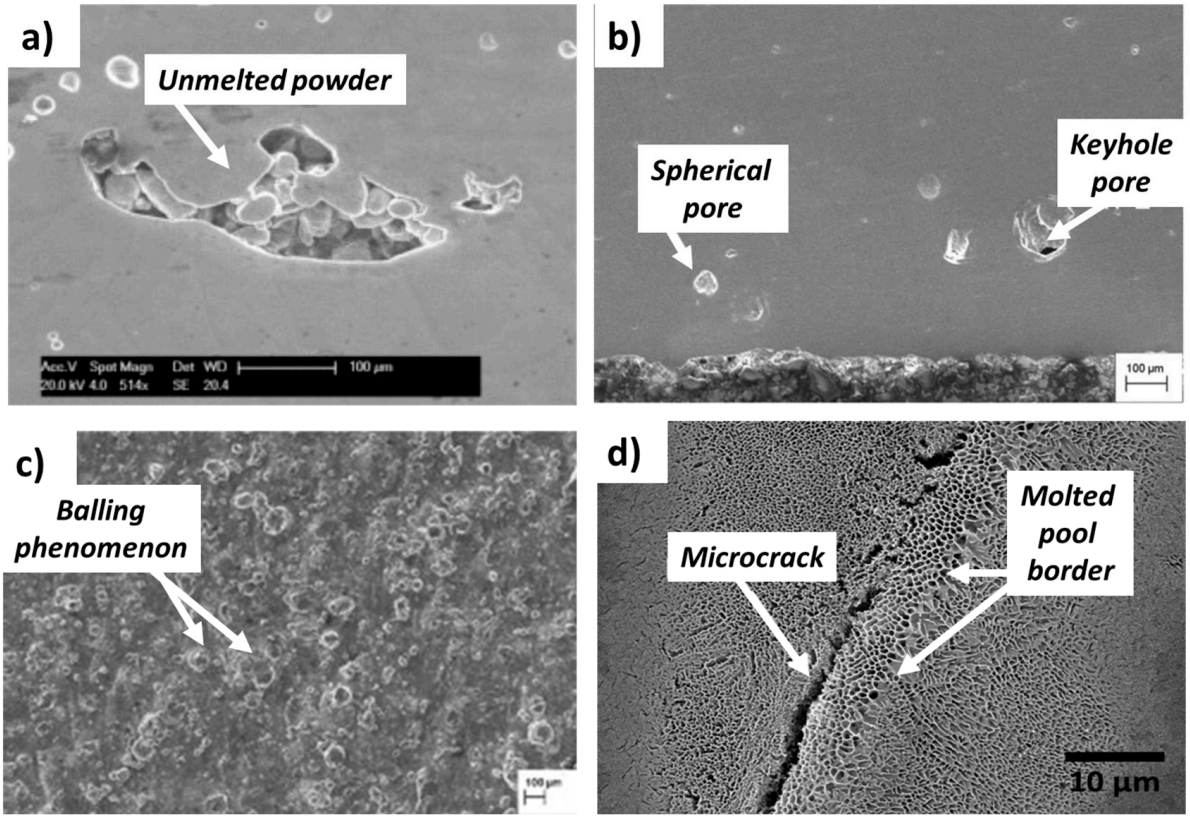

Figure 6. Metallurgical defects formation in SLM parts made of aluminum alloys. SEM micrographs show (**a**) randomly shaped pore enclosing unfused powders (reprinted from Ref. [206], copyright (2014), with permission from Elsevier), (**b**) entrapped gas pore and keyhole pore [reprinted from Ref. [207], (**c**) balling phenomenon and rough surfaces reprinted from Ref. [207], and (**d**) microcrack formation reprinted from Ref. [208].

The effects of higher laser power and scanning speed in the case of the AlSi10Mg alloy. Their experimental findings suggested that these AlSi10Mg alloys exhibit improved mechanical and microstructural properties due to the strong particle-to-particle bonding. Figure 7 illustrates all the parameters investigated in this study and a systematically explained scanning strategy for powder-based Al processing using SLM techniques [209]. These changes can include grain growth (individual crystals becoming larger), phase transformations (altering the crystal structure), recrystallization (creating new, strain-free grains), and the introduction of defects or micro voids. These alterations in microstructure can significantly impact the properties and performance of the material. The regular structure of the melt pool, accompanied by a heat-affected area with fine grain size, can be achieved by using a higher laser power and sufficient energy. These conditions are essential for creating more significant, extensive melt pools during additive manufacturing. Also, more energy is required for the weld pool to ensure a strong bond between the layers. This combination of increased laser power and sufficient energy promotes better melting and bonding between layers, leading to better mechanical and microstructural properties in the final product [210,211].

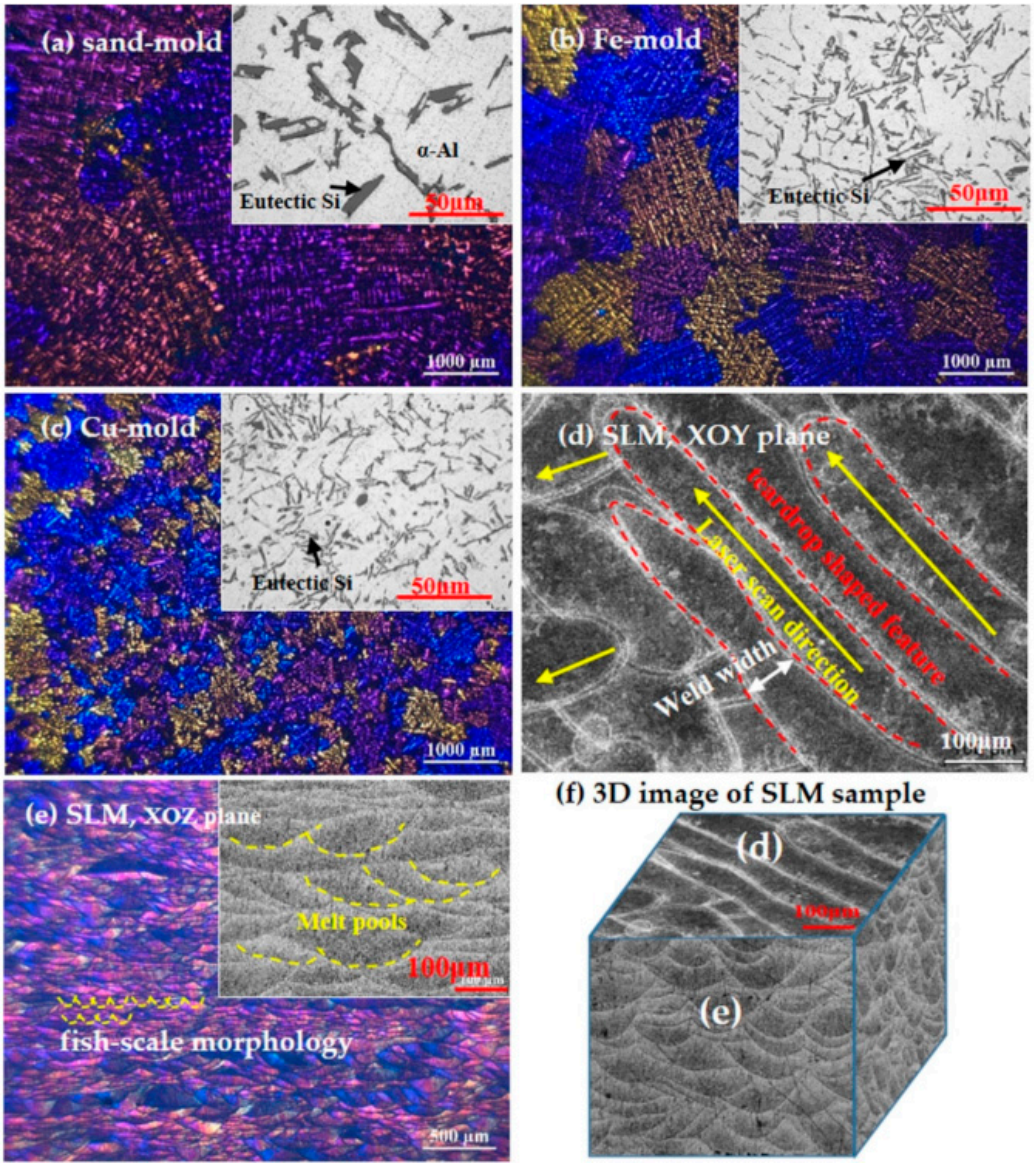

Figure 7. Microstructural evolution of the samples with different cooling rate (**a**–**c**) and the continuous melt pool structure model with fine HAZ. Images (**d**–**f**) correspond to the microstructures in XY- and YZ-planes—Reprinted from Ref. [209].

Moreover, the authors observed that this type of melt pool exhibits enhanced resistance to transverse stress during deformation, achieved through a fast-scanning process using higher laser power. This approach helps maintain stable energy inputs, ensuring the formation of continuous melt pools with fine heat-affected zones (HAZ) [212,213]. The resulting monolithic melt pools exhibit an acceptable structural zone and higher strength [209]. In Figure 7, the processing of the AlSi10Mg alloy using SLM techniques is depicted, showcasing the Al–Si layer boundary acting as a barrier for dislocation motion. In addition, many Al–Si delicate structures are formed within the uniform melt pool, which contributes to improved deformation resistance of the melt pool, ultimately leading to strengthened grain boundaries. In Figure 7a, the author noted that as the cooling rate increased, both the width of the heat-affected zone (HAZ) and the size of defects at the bottom of the melt pool increased. In Figure 7b, a comparison was made with samples subjected to coarse grain, resulting in a finer eutectic Al–Si cell, which was the primary reason for their high strength. Moving on to Figure 7c, the sample exposed to high Si input exhibited a coarser microstructure with α–Al columnar dendrites and spheroidized eutectic Si as dotted

pointed identified. Figure 7d,e also shows the transverse directional surface and lateral direction of the surface which is easily visible the differences in between. The Figure 7f is the combination of the both direction of the samples which is 3D view of the samples microstructure and continuous track and fish kind of the track of the lateral directions are visible and Figure 8 also represent the EBSD maps of a schematic diagram illustrating the continuous melt pool structure with a fine HAZ. High laser power was responsible for generating vast melt pools that tightly overlapped as can be seen in the 3D constructed microstructure image as shows the a′ and b′ [209]. This melt pool structure effectively resisted transverse stress during deformation, enhancing ductility and toughness. Simultaneously, rapid scanning at high laser power maintained stable energy input, facilitating the creation of continuous melt pools with fine HAZ. The excellent monolithic nature of these melt pools resulted in a more significant proportion of the delicate zone, leading to a significant increase in strength. Additionally, rotating each layer by 67° in the highly-dense monolithic structure reduced stress concentration within the sample [209].

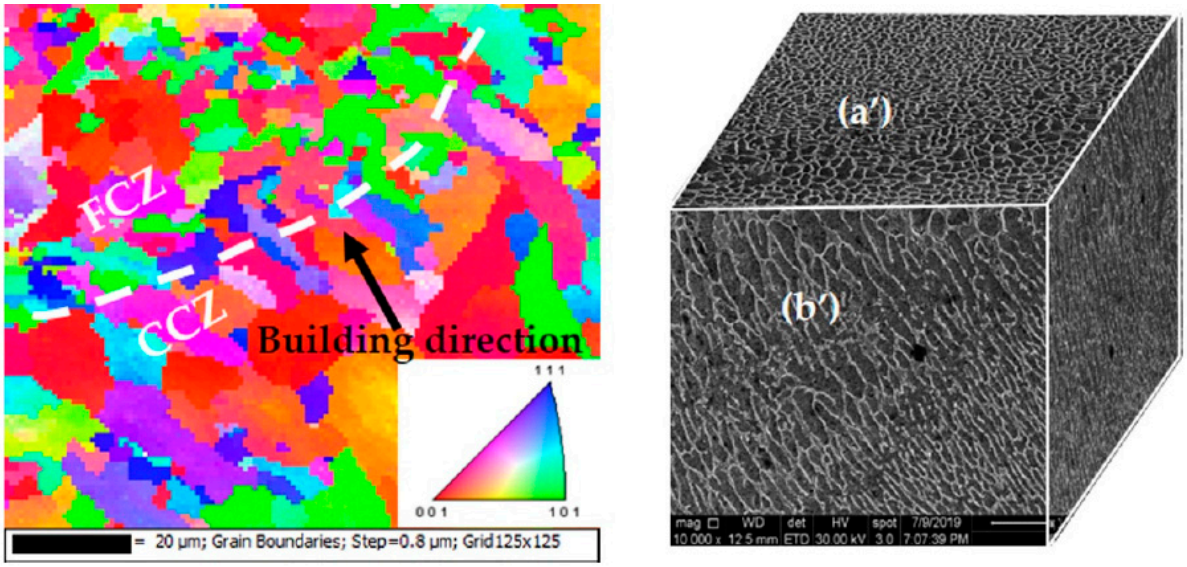

Figure 8. EBSD orientation maps of the sample in an XY-plane grain structure along the longitudinal direction and XYZ plane constructed from the SEM analysis—Reprinted from Ref. [209].

This combination of factors enhances the final product's overall mechanical properties and microstructural characteristics [214].

3.1.2. Mechanical Properties of the SLM Parts in Al Alloys

The mechanical characteristics of aluminum alloys hold significant importance when it comes to the production of components using SLM. This significance is amplified because aluminum alloys are renowned for their lightweight properties [215,216]. Understand that the mechanical properties of a component made with the selective laser printing technique with aluminum alloy powders do not meet the required standards or specifications. In that case, various problems can occur, including compromised structural integrity, limited performance, reduced life, and less reliability. Furthermore, achieving the desired mechanical properties is paramount for these components to strike an appropriate balance between weight reduction and sufficient strength. In general, insufficient quality of mechanical properties limits the effectiveness of weight reduction efforts and hampers overall performance. Table 3 summarizes some of the data in the literature concerning the mechanical properties of the Al alloy parts manufactured via SLM. From the analysis of the results reported in Table 3, it is evident that there are significant differences in tensile strength, percentage of elongation, and ultimate tensile strength (UTS) in MPa among the components built with different process strategies. The researchers observed that the minimum expected tensile

strength is approximately 250 MPa, while the maximum is 500 MPa, with a 50% difference due to the variation of the process parameters. Furthermore, the yield strength and the percentage elongations show similar variations, which the different process strategies can influence. The size of the laser beam and the scanning speed are both critical in producing lightweight components, and the appropriate choice of these parameters can significantly influence the mechanical properties of the components.

Additionally, powder preheating and sample post-heating are essential strategies for improving the mechanical properties of aluminum alloy SLM components, allowing you to optimize the microstructure and achieve the desired performance. Some studies also highlight the importance of choosing the growth direction of the component for its mechanical properties. Following a one-way or multi-directional strategy, growth can generally occur along the XY, XZ, and YZ planes [217,218]. According to researchers' findings, certain causes may remain undisclosed because specific aspects have not been thoroughly investigated. The variations in tensile strength, micro-hardness, and fatigue results observed across different research groups align closely with the data presented in Table 3 particularly concerning the micro-hardness test results. This heterogeneity is primarily attributed to variations in process parameters.

Table 3. Mechanical properties of AlSi10Mg and Al–Li alloy SLM specimens.

Powder Used	UTS (σb) [MPa]	YS (σ0.2) [MPa]	Elongation (δ) [%]	Remarks	Ref.
AlSi10Mg	494	309	6	The author reported that the YS of the horizontal direction is higher than the vertical due to the rapid cooling effect changing the powder's microstructural and mechanical properties.	[219]
AlSi10Mg	(a) 448.0 (b) 241.7 (c) 451.7	(a) 263.0 (b) 180.3 (c) 310.2	(a) 9.8 (b) 9.6 (c) 6.2	They have found three different categories: (a) as built (ab), (b) T6 treatment, and (c) direct aging (DA)	[220]
AlSi10Mg	385 ± 5	-	4.5	The author reported under the argon and nitrogen environment of a closed chamber.	[68]
AlSi10Mg	452 ± 1 (H) 482 ± 1 (V)	264 ± 4 (H) 247 ± 1 (V)	3.6 ± 1 (H) 6.5 ± 0.3 (V)	NA	[221]
AlSi10Mg	420 (H) 400 (V)	245 (H) 220 (V)	5.9 (H) 3.2 (V)	They used an argon environment to process SLM and there was no preheat as described.	[222]
AlSi10Mg	434.24 ± 10.7 282.36 ± 6.1	322.17 ± 8.1 196.58 ± 3.6	5.3 ± 0.22 13.4 ± 0.51	The built sample has higher strength than the solutionized treated samples at 550 °C for 2 h due to Si particles significantly influencing the tensile properties of the used powder Argon with 100 °C preheat environment	[223]
AlSi10Mg	473 (AB) 479 (HT)	263 (AB) 298 (HT)	7.8 (AB) 5.6 (HT)	Relatively little difference is as built AB and Heat-Treated HT	[224]
AlSi10Mg	391 (XY-direction) 343 (XZ-direction)	311(XY-direction) 266 (XZ-direction)	7.2(XY-direction) 5.46(XZ-direction)	The difference between the strength of the cast material and the forging material is because of the acceptable microstructure performance.	[225]
Al–Li alloys	64.66 (parallel direction) to 99.35	-	6.3, 4.6	Investigated results show that, with the decrease in scanning speed, the micro-hardness of parallel to building direction was increased from 105.4 HV to 121.4 HV, and the tensile strength increased, indicating that the decrease of the scanning speed can reduce metallurgical defects of Al–Li alloy	[226]

Table 3. *Cont.*

Powder Used	UTS (σb) [MPa]	YS (σ0.2) [MPa]	Elongation (δ) [%]	Remarks	Ref.
AlSi10Mg	456 (XY-direction) 359.5 (Z-direction) 290 (MPa)	368 (XY-direction) 306.5 (Z-direction) 262	3.0 (XY-direction) 1.7 (Z-direction) 2.5	Samples (a) and (b) are built, and (c) heat is treated with solutionized treatment quenching + artificial aging T6 due to hardening microstructure refinement as a reference of the hall patch equation.	[227]
AlSi10Mg	373 ± 3 369 ± 8 363 ± 7 348 ± 2	230 ± 3 229 ± 6 219 ± 6 210 ± 2	8.3 ± 0.9	Direct aging could increase yield strength 300 MPa and 500 MPa, as cold-built materials resist softening by stress relief treatment.	[228]
AlSi10Mg	260 496	220 296	1.0 5.0	The Si eutectic network globalized into Si particles, continuing to decrease UTS 400 MPa to 290 MPa and increasing ductility; up to 15 of these are cast and T6 treated used alloys.	[229]

3.1.3. Corrosion Behavior of SLM Parts in Al Alloys

It is widely recognized that environmental conditions can also significantly impact the physical properties of SLM-fabricated samples. Several authors demonstrate that in addition to the correct control of process parameters in SLM, managing exposure to oxygen or other corrosive agents is also essential to obtain the desired material properties and ensure components manufactured with SLM are high quality and durable.

The specific manufacturing methods and conditions of aluminum alloys can vary significantly based on the type of aluminum alloy used and the intended application of the end product.

Generally, aluminum alloys are fabricated at elevated temperatures to improve their formability and reduce the energy required for plastic deformation during forming processes (e.g., hot rolling, extrusion, and forging) in a vacuum or an oxygen-existing environment. Note that while some additive manufacturing methods use vacuum or oxygen environments, the SLM of aluminum alloys typically occurs within an inert gas atmosphere. Using an inert gas environment minimizes oxygen content, allowing for successful SLM of aluminum alloys without excessive oxidation.

Corrosion is a potential problem for all metals, but even more so for metal alloys such as aluminum. Furthermore, the SLM process introduces certain factors that can influence the corrosion behavior of manufactured components, such as surface roughness, residual stresses, variations in composition, and porosity.

According to a recent study [230,231] on AlSi10Mg alloys fabricated using SLM, the corrosion phenomena for this alloy are mainly attributed to the presence of Si particles. These particles contribute to the reduction of the energy density of the grain, mainly due to the rapid cooling of the deposited layer during the SLM process. To address this issue, post-manufacturing heat treatments are typically employed. These treatments involve a complete aging heat treatment cycle performed under standardized processing conditions, effectively mitigating the problem of corrosion caused by Si particles. The potentiodynamic polarization test is the one most used for corrosion investigations. A sodium chloride (NaCl) concentration of 3.5 wt% was used to perform this test. In this context, demonstrated that the corrosion resistance of AlSi10Mg alloy samples deteriorates as Si particles grow. This degradation is evident through several indicators, including higher corrosion current density, lower corrosion potential, reduced film strength, and lower charge transfer resistance observed in heat-treated samples [232].

Figure 9 shows the potentiodynamic polarization curves for the SLM as-built samples in Al alloy and casted alloy comparison investigation. The as-built samples showed a potential voltage of approximately 120–150 mV and a corrosion potential varying towards the as-built samples direction. The resulting corrosion resistance values for comparison are as-casted $4.75 \times 10^3\ \Omega\ cm^2$, Al-horizontal direction in an argon environment $9.57 \times 10^3\ \Omega\ cm^2$,

Al-vertical direction in an argon environment 12.1 × 10^3 Ω cm^2, Al-horizontal direction in a N_2 environment 15.9 × 10^3 Ω cm^2, and Al-vertical direction in a N_2 environment 10.3 × 10^3 Ω cm^2 as reported. In particular, as the built environment of the argon to nitrogen increased, the i_{corr} values also increased, indicating a higher corrosion rate for the samples than the as-built ones.

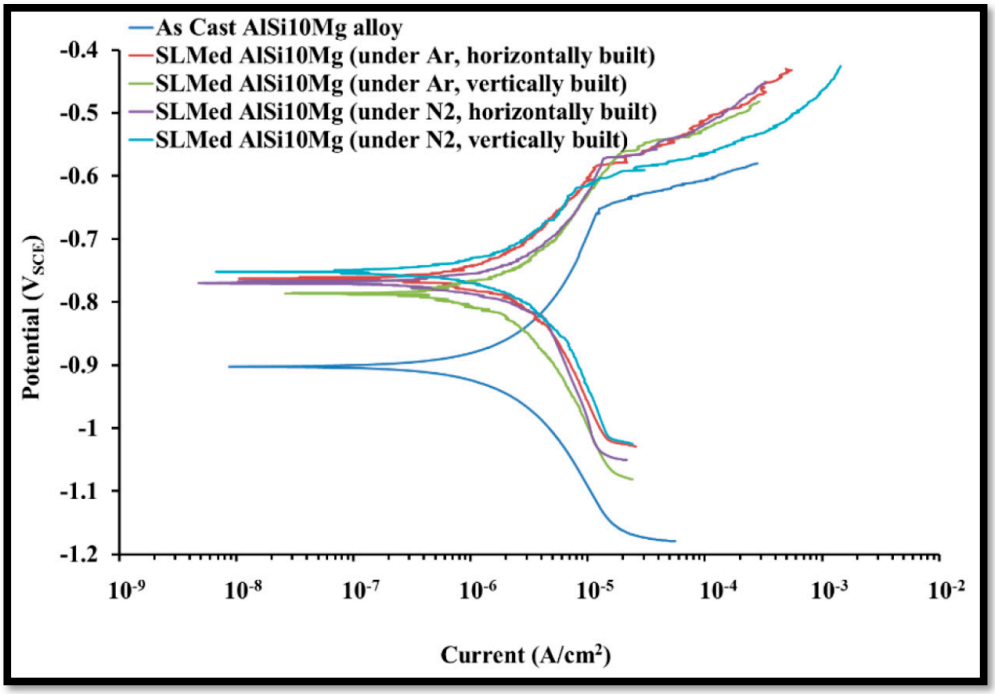

Figure 9. Potentiodynamic polarization curves of SLM-produced AlSi10Mg alloys and non-heat-treated counterparts in 0.1M % NaCl solution at room temperature (E potential; i current density) Reprinted from Ref. [232].

However, in contrast to the i_{corr} values, the potential voltage (corrosion potential) showed a slight difference in the temperature range of –0.7 V to –1.0 V for the Ar and N_2 environment-built samples. Despite the variation of the corrosion rate with increasing temperature, the corrosion potential remained relatively stable and within a similar range for all heat-treated samples. Overall, these results suggest that heat treatment at higher temperatures degrades the corrosion resistance of SLM samples, leading to higher corrosion rates (reflected by i_{corr} values), while the corrosion potential remains relatively constant over the tested temperature range. Instead, Figure 10 presents the results obtained on SLM-processed AlSi10Mg alloys from electrochemical impedance spectroscopy (EIS) using Nyquist and Bode plots. Interestingly, it was observed that all samples, regardless of their heat treatment and particle density, exhibited only a single capacitive loop in their Nyquist plots (Figure 10a–c). The Bode phase degree plots (Figure 10c) also displayed a broad plateau around the middle frequency, with minimal variation across the reported frequency range and low-angle peaks, and Figure 10d represents the perfectly fit circuity during the test of the corrosion behavior of respective Ar and N_2 environment-produced samples [232]. These EIS findings can be attributed to two main factors:

Heat treatment: The heat treatment applied to the specimens might have altered their microstructure, resulting in changes in the corrosion behavior. Only a single capacitive loop in the Nyquist plots suggests a predominant capacitive behavior, which could be associated with forming passive oxide layers on the surface. The heat treatment might have influenced the oxide layer's characteristics, leading to a similar capacitive response in all the heat-treated samples.

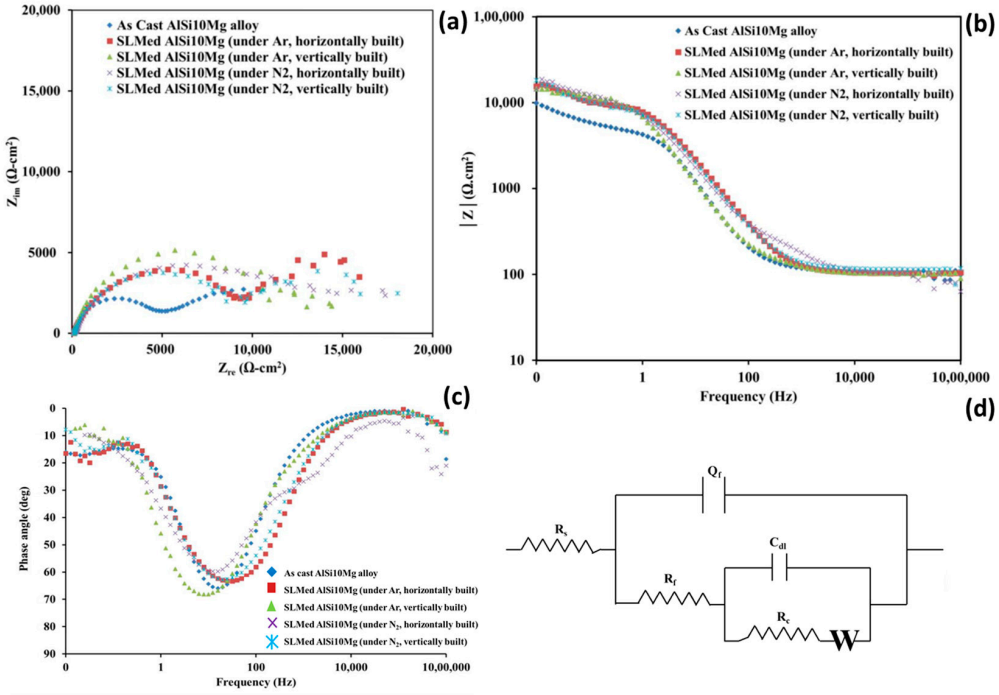

Figure 10. Electrochemical impedance spectra of SLM-produced AlSi10Mg alloys and Ar and N_2 counterparts in a 0.1 M % NaCl solution at room temperature: (**a**) Nyquist plot; (**b**) bode plots (**c**) phase angle results, and (**d**) equivalent circuit diagram Reprinted from Ref. [232].

Insufficiently dense particles: Another factor influencing the EIS results could be related to the density of the particles in the SLM specimens. If the samples had insufficiently dense regions, it could create areas where the corrosion occurs primarily on the layer surface, leading to the observed finite diffusion layers. These localized corrosion phenomena can affect the impedance response, resulting in the observed broad plateau in the Bode phase degree plots [11,231,232].

3.2. SLM Parts in Titanium Alloys

Titanium, including the SLM process, is one of the most used materials in AM technology. The ability to machine titanium using SLM has opened up opportunities for producing complex, lightweight components in this high-performance material. On the other hand, titanium is prized for its resistance to corrosion and high temperatures and is often employed in industries such as aerospace, chemical, and medical implantology. Among the Ti alloys, the most widely used is the Ti6Al4V alloy (ASTM 5 grade). Although it falls into the category of non-ferrous alloys, the SLM processing parameters are different from those used for Al alloys due to different physical properties, thermal conductivity, and surface tension [233–236] demonstrate that the surface morphology and characteristics of SLM components do not depend only on the process parameters but also on the properties of the powder. In particular, it is essential to know three crucial characteristics of each powder particle: its microstructure, morphology, and chemistry (i.e., how it reacts during processing conditions) [237,238]. Table 4 shows the process parameters for the most popular titanium alloy: Ti6Al4V.

While some level of porosity can be advantageous for specific applications in the manufactured components, striking the right balance to retain all desired properties presents a challenge.

The SLM process is adept at striking this balance, but it is critical to make preliminary adjustments independently when configuring final processing parameters [239].

Table 4. Process parameters considered by researchers during SLM process for Ti6Al4V alloy.

Laser Beam Diameters [μm]	Laser Power [W]	Layer Thickness [μm]	Hatch Distance [μm]	Laser Type	Scan Speed [mm/s]	Remarks	Ref.
-	51.84–388.8	30	120	IPG Photonics Ytterbium YLR-400-SM fiber laser	600–1200	Experimentation was done under the Ar atmosphere with O_2 content below 100 ppm, volume energy density 24–90 J/mm^3	[240]
-	140–180	30	60–100	Dimetal-100 SLM	700–1500	Annealing heat treatment for 2 h at 600–1050 °C set for the β phase	[241]
60	50–140	30	60–100	Yb-fiber laser 500 W	300–1200	The Ar atmosphere with high purity of 99.999%, O_2 content below 0.02%, and annealing heat treatment cycles was used to manage under the three different cycles at different temperatures 850 °C/2 h/FC (furnace cooling), 1050 °C/2 h/FC, and 950 °C/ 1 h/AC (air cooling) 550 °C/6 h/AC	[242]
-	120–200	25	100	Laser M2, 400 W	900–1400	Volume energy density 34.29–97.78 J/mm^3, maximum scan speed 7000 mm/s, under protective argon atmosphere	[243]
70	80–180	20–80	30–100	Yb-fiber laser 200 W	800–2500	Under argon gas to maintain an oxygen level below 0.5 volume % (vol.%).	[244]
80–100	346–382	50–100	300	-	900	10 m, (11%) of the laser beam size could lead to over 40% change in the overall volume of the spatter generated.	[245]
300	200	30	140	-	900	Zigzag scanning strategy, the overlap rate is 50%	[246]
-	280–360	30	141	Yb-fiber laser; 400 W	1000–1400	Laser power, the scanning speed, has a more substantial influence on the performance of the part	[247]
-	95–180	30	50–70	300 W-fiber laser	1600–2505	30 °C and <500 ppm O_2 to limit oxidation on each layer maintained Energy Density 23.7–63.0 J/mm^3. They also performed heat treatment at 850 °C, holds for 25 h and 50 h, followed by a 40 °C/min cooling rate to 20 °C	[248]
-	60	25	60	120 W-Yb-fiber laser with a wavelength of 1.07 μm.	1000	Shielding gas argon, and heating 750 °C for 3 h	[249]

Table 4. *Cont.*

Laser Beam Diameters [μm]	Laser Power [W]	Layer Thickness [μm]	Hatch Distance [μm]	Laser Type	Scan Speed [mm/s]	Remarks	Ref.
75	200	30	65	a fiber-modulated pulsed laser having a maximum power of 500 W and a wavelength of 1070 nm	1500	Preheated to 80 °C, argon gas to prevent oxidation	[250]
200	240	30	50	Yb-fiber laser (1064 nm) maximum laser powder of 400 W	240	Argon gas to oxygen concentration below 0.13 Vol%, heated to 900 °C for 2 h under argon atmosphere and furnace cooling	[251]
-	40–500	20–200	22.5–693	Yb-fiber laser 400 W	25–3200	11.11–373.33 Energy density J/mm^3,	[252]
-	240	50	120	500 W Yb: YAG-fiber laser and an F-theta lens	300	Argon until the oxygen volume fraction was below 0.1%, zigzag scanning manner, preheating temperature 200 °C., annealing 950 °C, 1000 °C and 1050 °C for 40 min	[253]
80	500	60	200	500 W, Yb	1000	Operating under a protective argon atmosphere	[254]
-	200	50	100	1.064 μm, Yb: YAG	500, 625, 750, 1000, 1250	0.1% of the Ar higher-purity environment used for the processing of the Ti alloys by SLM, energy density was varying from 32–80 J/mm^3	[255]
40	200	50	100	1.064, Yb: YAG	500	Used alternating scanning vector 90° angle for processing to avoid residual stress and to enhance the bonding of particles.	[256]

3.2.1. Microstructural Morphology of SLM Parts in Ti Alloys

Components of Ti alloys using SLM exhibit diverse microstructures with varying morphologies and phases. In certain instances, the α phase is formed with acicular martensite, while in others, the heating effect results in a lamellae structure within a Ti-matrix of α + β structure. Proper grain size distribution and homogenous phase formation are crucial in controlling microstructural properties, directly influencing mechanical enhancement. There are substantial differences in microstructural and mechanical properties between components in their as-built state and those that undergo artificial aging treatment. The aging treatment leads to significant modifications in microstructure and mechanical behavior, further emphasizing the importance of managing the microstructural features to achieve desired material properties [257].

Porosity has been noted to impact titanium alloy samples. To address these concerns, it is crucial to conduct a comprehensive examination of the processed samples and conduct a thorough evaluation of microstructural behaviors. Figure 11a–f offers an in-depth perspective on a titanium-based alloy sample manufactured using the SLM process. The grain size distribution and formation process play a significant role in the recrystallization of the specimen. In Figure 11, the EBSD analysis reveals the transition from more significant to smaller grain distributions. The average grain sizes, calculated in micrometers (μm), for each case are as follows: (a) 6.70 μm, (b) 7.42 μm, (c) 15.14 μm, (d) 20.71 μm, (e) 23.42 μm, and (f) 67.43 μm [97].

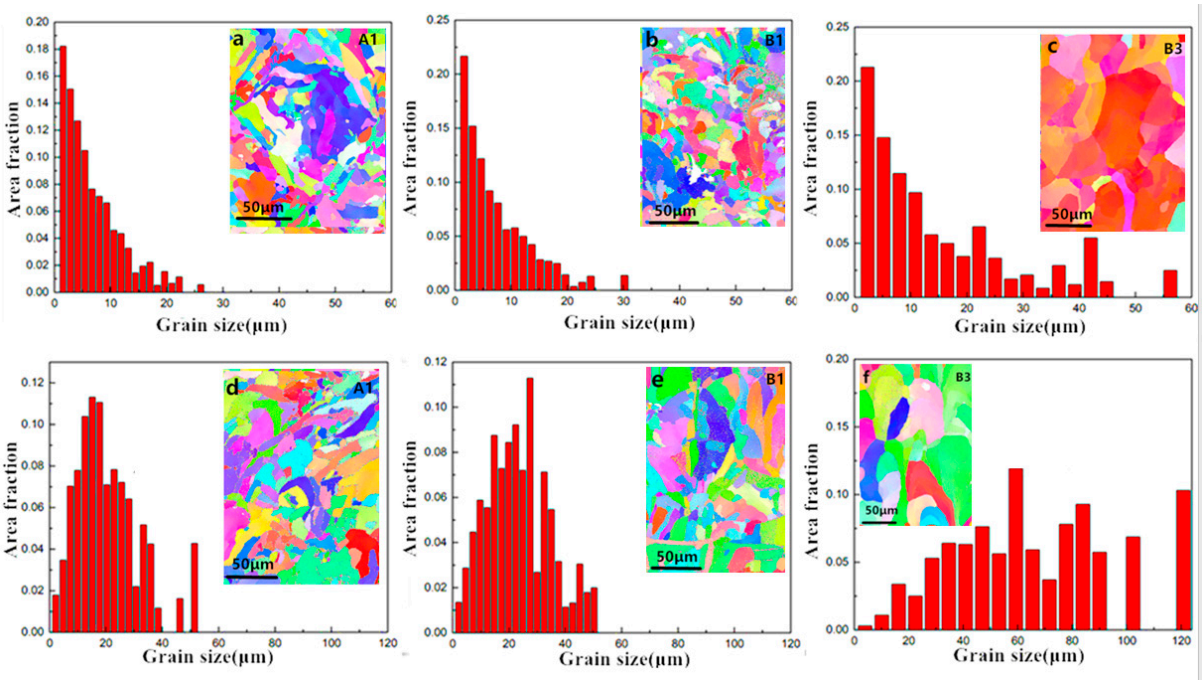

Figure 11. Grain size distributions of specimens and EBSD maps showing the grain morphology of SLM-processed Ti37Nb6Sn samples corresponding to the horizontal (XY) and vertical (YZ) sections: (**a**,**d**) Specimen A1; (**b**,**e**) specimen B1; (**c**,**f**) specimen B3 (reprinted from Ref. [97], copyright (2018), with permission from Elsevier).

3.2.2. Mechanical Properties of the SLM Parts in Ti Alloys

Parts made of titanium or titanium alloys using the SLM technique generally have superior mechanical properties to those made of aluminum alloys [258,259]. Table 5 shows some fundamental mechanical properties, such as tensile strength, of SLM samples in titanium and titanium alloys. As with aluminum alloy SLM specimens, it has been observed that also for titanium or titanium alloy SLM specimens, heat treatment cycles conducted under different conditions can be essential to develop mechanical properties comparable to parts produced with traditional techniques. These heat treatments can

optimize the microstructure of SLM titanium or titanium alloy components, reduce residual stresses, increase fatigue strength, or improve corrosion resistance. Ultimately, they allow for mechanical properties that approach or exceed those of parts manufactured using traditional techniques.

In their work focusing on biomedical applications, emphasized the preference for titanium alloys like Ti6Al4V for medical implants. This choice is attributed to their advantageous features, including a low Young's modulus, excellent biocompatibility, superior corrosion resistance, and remarkable strength compared to stainless steel and CoCr alloys [98]. Within titanium alloys, the microstructural characteristics are influenced by the formation of phases, with changes attributed to the combination of martensitic phase formation and α + β phase formation [260]. For instance, highlighted a notable achievement in bone porosity, reaching 61%, a level nearly equivalent to natural bone porosity. This underscores the remarkable success of the additive manufacturing (AM) process, particularly SLM, in achieving such results [261].

Table 5. Mechanical properties of SLM specimens in Ti alloys.

Powder Material	UTS (σ_b) [MPa]	YS ($\sigma_{0.2}$) [MPa]	Elongation (δ) [%]	Remarks	Ref.
Ti6Al2Zr-1Mo1V	780–1422	-	3–18	α + β phases show a needle-like structure that looks like a martensitic phase, and coarse lamellae structure also formed	[60]
Ti37Nb6Sn	891	850	E-Mod. 66 GPa, Ductility 27.5%, max	This method can aid the design of customized titanium devices with low the elastic modulus for orthopedic implant applications	[97]
Ti6Al4V	1012	932	-	Strain-1.4% after heat treatment	[262]
Ti6Al4V	1195	1118 ± 39	5	Ti6Al4V Samples have higher tensile strength than EBM-produced samples	[263]
Ti6Al4V	1095	955 ± 6MPa	8.1	Its mechanical properties strongly depend on its microstructure	[264]
VT6 and VT20L	(Before Heating) BH-UTS-863 ± 9, (After Heating) AH-UTS- 580 ± 12	(Before heating) BH-YS-840 ± 6, (After Heating) AH-YS-453 ± 2	BH-EL 2.2 ± 1.7%, AH-EL 8.2 ± 1.6%	Bending α 25 ± 4° properties, the impact energy 49 ± 18 kJ/cm^2, heating at 300 °C	[99]
Ti6Al4V	1267 ± 5	1110 ± 9	E-Mod. 109.2 ± 3.1 GPa, EL 7.28 ± 1.12	The SLM-processed specimen was characterized under different heating conditions	[100]
Ti6Al4V	989 ± 10	940 ± 10	-	61% Porosity achieved in this specimen that is almost near to natural bone, Compression YS 1040 ± 13 MP; UCS 1842 ± 17 MPa	[101]
Ti6Al4V	1140	760 ± 1	3.2	Variations in thermophysical properties may arise from differences in the initial metallurgical state, potentially attributed to alterations in the transformation behavior	[265]
Ti6Al4V	975–1120	1350	EL 7.7%, E-Mod. 1150 GPa	Mathematical simulation and experimentation both approximate mechanical analyses carried out using boron content; compressive strength-19.46–416.47 MPa	[266]
Ti6Al4V	-	YS-255.8 MPa to 204.9 MP	14.7	Heat-treated at 750 °C, impact test 233.6 ± 1.5 MJ/m^3, ε = 50%	[267]
Ti6Al4V	AB-UTS-1156 MPa, AHQ- 1124	1228 MPa, AHQ-1032 MPa	E-mod. 130 GPa, EL 8.6%, AHQ-E-Mod. 108 GPa, EL 8.3%	Samples heat-treated at 800 °C and 850 °C for 4 h, s-fabricated samples consist of lamellar α′ and acicular α′; many twins in the lamellar α′ and small α_2 precipitation in the acicular α′ were found	[268]
Ti, Ti–6Ta different % alloys	550–1186	470–1029	E-Mod. 75–550 GPa	By Ta addition ranges from 0 to 25 wt %, there is an improvement on the tensile strength from 641 to 1186 MPa, micro-hardness 240–353 HV, micro-hardness from 257 to 353 HV also increased	[269]

Table 5. *Cont.*

Powder Material	UTS (σ_b) [MPa]	YS ($\sigma_{0.2}$) [MPa]	Elongation (δ) [%]	Remarks	Ref.
Ti–Nb	740 to 685	640 to 574	Ductility 19.5% to 17.3%	Increase of energy density from 70 J/mm^3 to 100 J/mm^3, and then, it increases to the highest at 110 J/mm^3 This variation is determined. by both the coarsening of α' phase and the formation of β (Ti, Nb) solid solution, micro-hardness 261 HV to 245 HV	[270]
Ti10V2Fe3Al	935–939	922–934	>10	α-bearing samples all show poor ductility EL < 1.2%	[271]

3.2.3. Corrosion Behavior of SLM Parts in Ti Alloys

The electrochemical behavior of Ti alloys fabricated using SLM can be tailored to different functionalities by optimizing the alloy composition, microstructure, surface finish, and exposure environment. On the other hand, it is widely known that the presence of various elements, such as aluminum (Al), vanadium (V), chromium (Cr), and others, in addition to titanium, can have a significant impact on the electrochemical behavior of the material, as well as a fine and homogeneous microstructure can lead to better electrochemical performance, as it provides more uniform corrosion resistance.

Moreover, multiple researchers have shown that deposition orientation influences the material's microstructure, crystallographic texture, and surface roughness. These factors, in turn, have a notable effect on the formation and stability of the passive layer [272–275]. Specifically, the passive layer refers to a thin and stable oxide layer that forms on the surface of metals, providing them with corrosion resistance. Investigated the SLM-processed Ti6Al4V alloy in XY and XZ planes. Their findings revealed that the XY plane exhibited superior resistance due to the passive layer's reduced stability compared to the XZ plane [276]. It is identified another contributing factor to the enhanced corrosion resistance in Ti6Al4V alloys: the formation of α''-phase with a martensitic orthorhombic crystal structure. They observed that this phase formation played a crucial role in improving the material's resistance to corrosion. Additionally, the authors found that the lack of pitting corrosion in Ti alloys, especially in β-phase, was due to the stabilizing element Nb, which was present in sufficient amounts to fully retain the bcc β phase up to room temperature. More interestingly, the study's results showed that the as-built specimens exhibited a significantly low E_{corr} voltage of as-built -0.201 V, and polished samples had much lower -0.791 V, and in addition, the i_{corr} values were notably low at 0.621×10^{-7} A/cm^2 in this case. These findings suggest that the martensitic α'-phase and low surface roughness contribute to the excellent corrosion resistance properties of Ti6Al4V alloys in their investigation [277].

The investigated presented interesting results on the corrosion behavior of Ti6Al4V alloy fabricated through the SLM process. This work examined corrosion using standard solutions, such as NaOH, NaCl, H_2SO_4, and SBF, representing different media types: alkaline, neutral, acidic, and physiological. In addition, the work focused on the influence of molarity and pH values, respectively, with the following specific values for each standard electrolyte solution: 1.0, 13.6, 0.6, 6.8, 0.5, 0.6, and 1.0, 7.4. These parameters were carefully chosen to understand the corrosion phenomena in different environments. In Figure 12, the corrosion potential versus corrosion current density (i) is shown, providing insight into how the electrochemical behavior of the alloy varies in different electrolyte environments. The OCP and PDP tests revealed that the passive layer formed immediately upon immersing the samples into the electrolytes. In both cases, the passivation current exhibited an ascending trend: NaOH < SBF < NaCl < H_2SO_4. Similarly, the pitting potential increased: H_2SO_4 < NaCl < SBF < NaOH. Additionally, Figure 13a, b shows a Nyquist, bode plot, and phase angle graphical representations of the experimental results, revealing the impact of various electrolyte environments on the corrosion phenomena observed in the Ti6Al4V alloy. The PDP and EIS findings indicated the existence and breakdown of a dense and porous TiO_2 layer. Among the various electrolytes, NaCl was observed to be more corrosive

than SBF and NaOH, while H_2SO_4 proved to be the most aggressive for both cast and SLM Ti6Al4V. Pitting occurred through the dissolution of the porous layer, triggered by localized pitting in NaCl or extensive cracking in H_2SO_4, with more pronounced damage occurring in SLM when exposed to the harsher electrolyte [278]. Also, explored the corrosion behavior of Ti6al4V samples and found improved corrosion resistance. This increased strength has been attributed to several factors, including the presence of similar grain structures, the rapid initial passivation process, and the protective effect of the bonded reaction layer on the α'-Ti phase against corrosion [279]. Finally, research highlighted the benefits of SLM processing for Ti6Al4V alloys, as it resulted in parts with superior corrosion resistance compared to traditional wrought and heat-treated Ti alloys due to higher hydrophobicity, better grain boundary density, and homogenous alloying elements stimulated in saliva at 37 °C. In particular, the study employed electrochemical testing and contact angle tests to evaluate the corrosion resistance of the different materials [280].

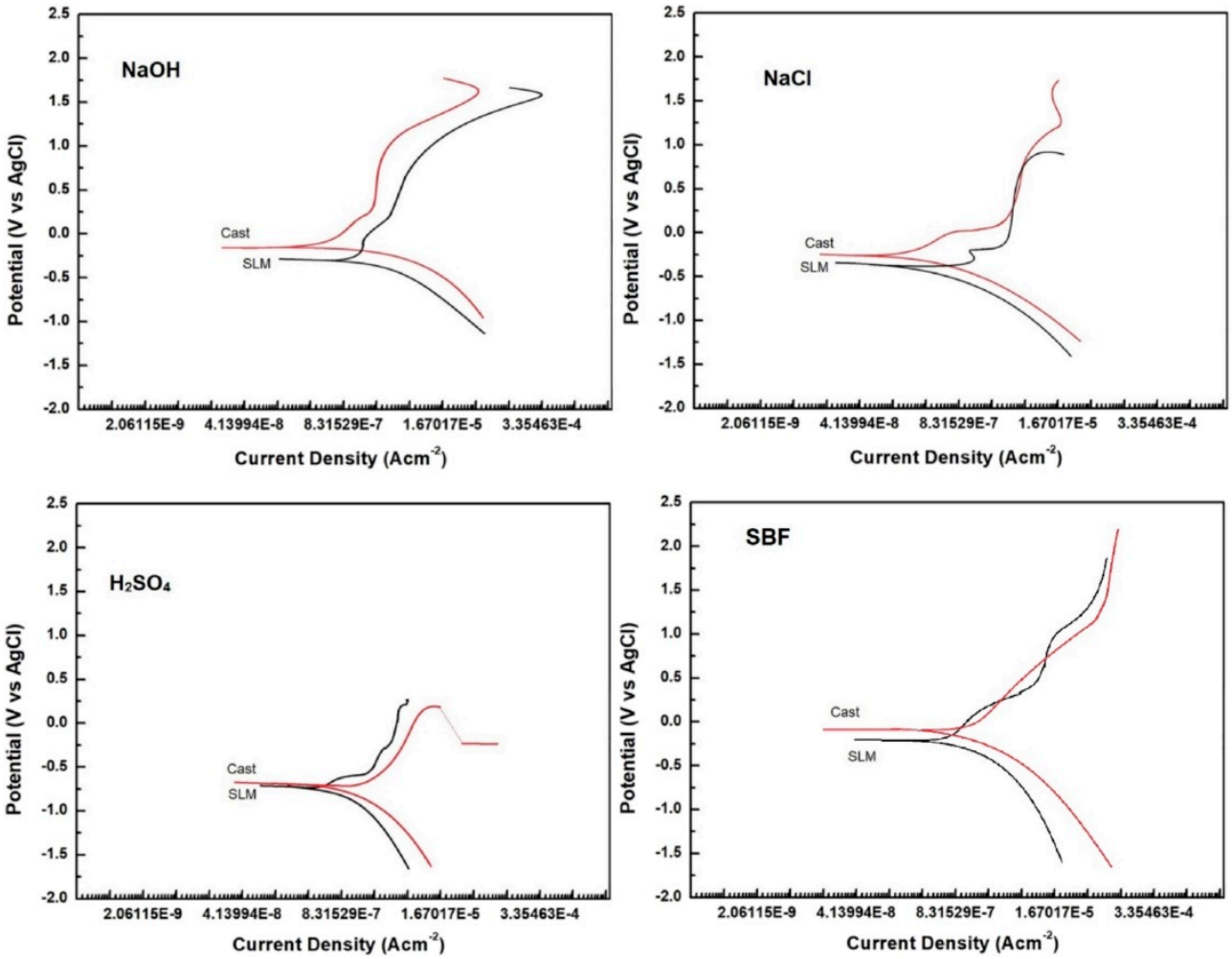

Figure 12. Potentiodynamic polarization curves of the cast and SLM Ti6Al4V alloys obtained with different electrolytes (reprinted from Ref. [278], copyright (2020), with permission from Elsevier).

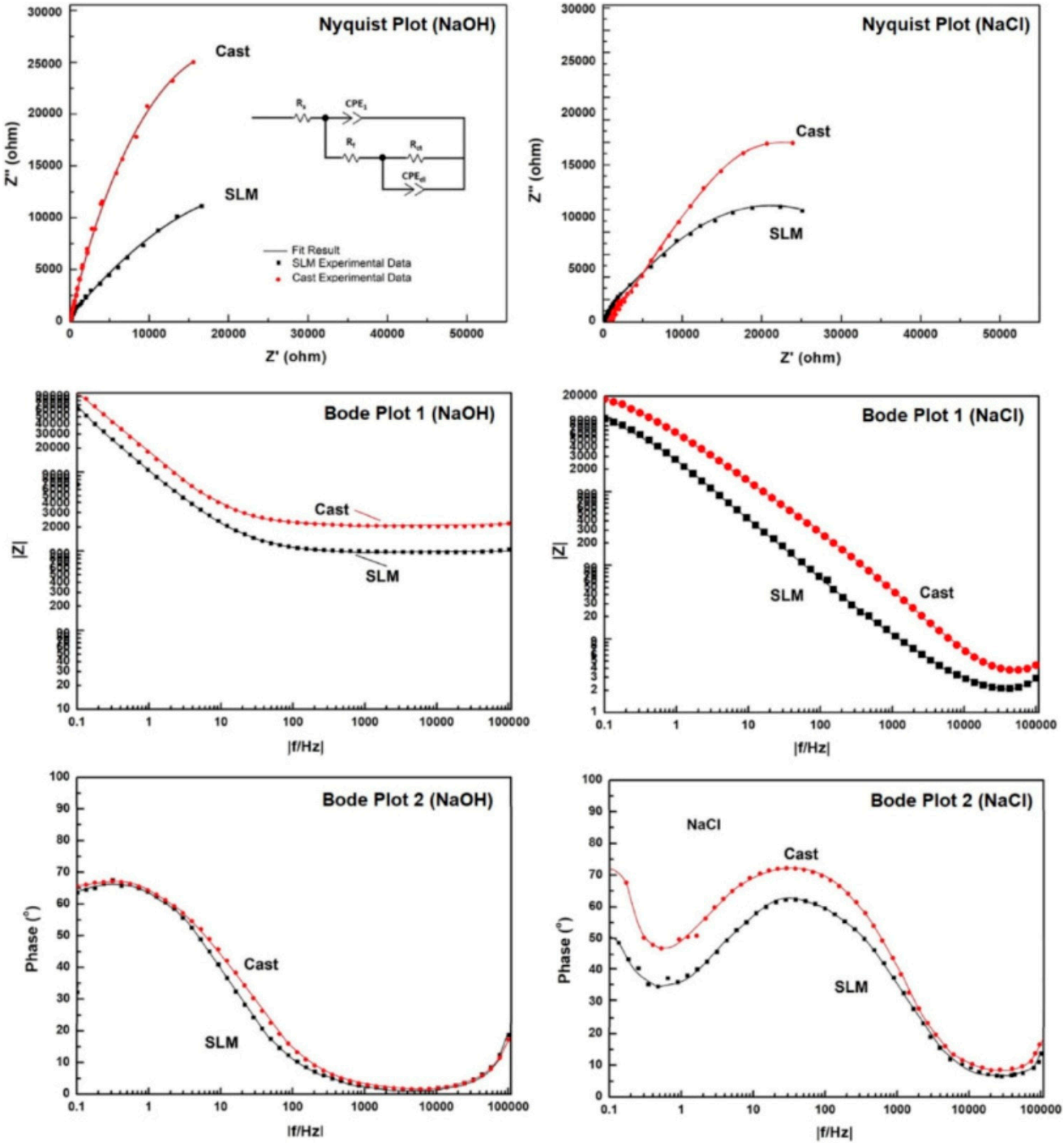

(a)

Figure 13. *Cont*.

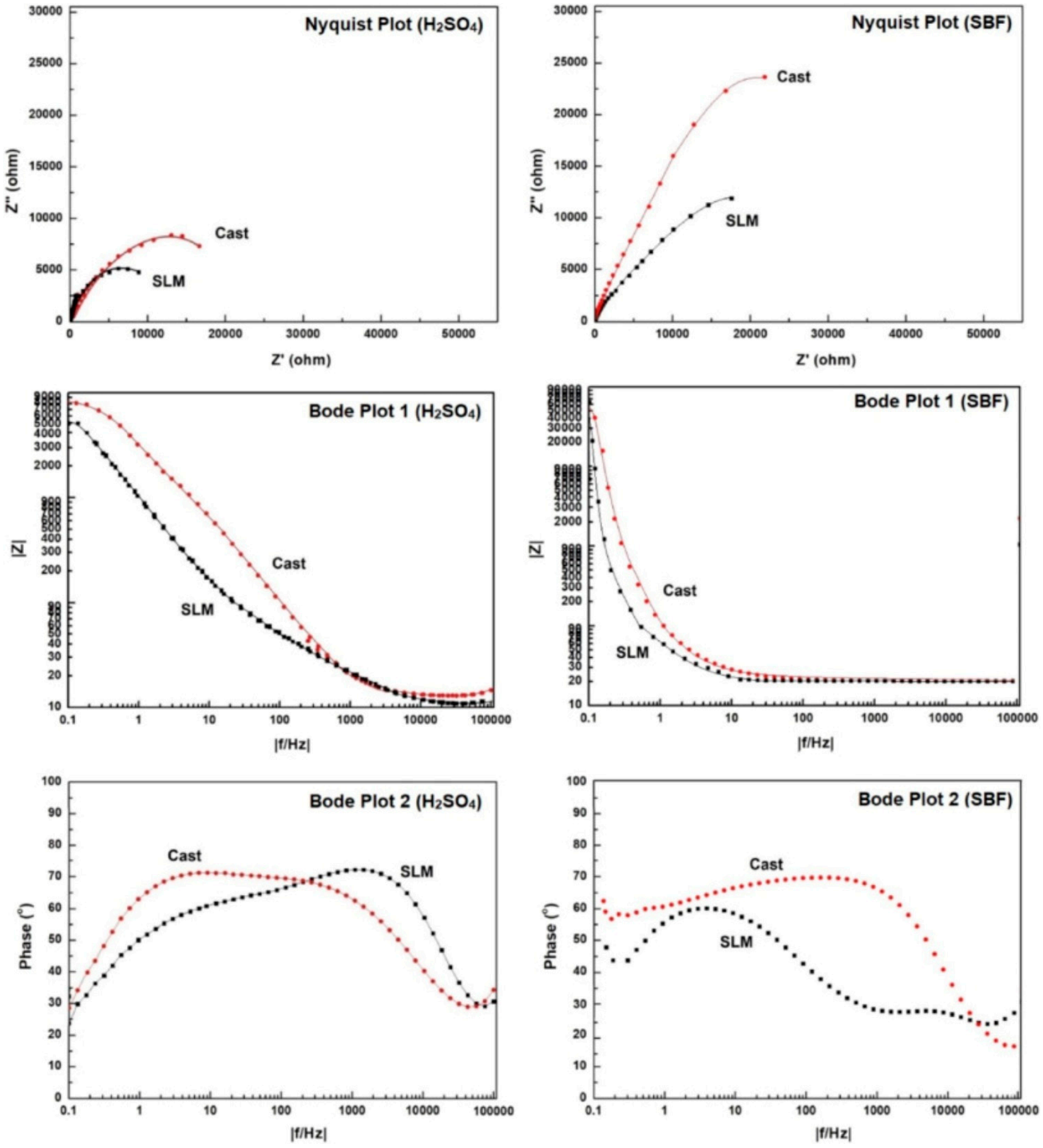

(**b**)

Figure 13. (**a**) EIS plots of the as-cast and SLM Ti6Al4V alloy. These were obtained in NaOH and NaCl electrolytes. The various Nyquist plots, bode impedance plots (Bode Plot 1), and Bode phase plots (Bode Plot 2) are indicated in the corresponding media. The inset shows the corresponding equivalent circuit diagram (**b**) EIS plots of the cast and SLM Ti6Al4V alloy were obtained in H_2SO_4 and SBF electrolytes (reprinted from Ref. [278], copyright (2020), with permission from Elsevier).

3.3. SLM Parts in Steel Alloys

Steel is known for its high mechanical strength, ductility, and ability to withstand high stresses. Furthermore, steel alloys offer a wide range of properties, such as corrosion resistance, toughness, and hardness, making them suitable for many applications. These alloys are obtained by combining iron with other elements, such as carbon, chromium, nickel, and many others, to improve their characteristics. The use of steel in SLM allows the unique properties of this material to be exploited in an additive manufacturing process, offering high performance, precision, and greater design freedom. Table 6 presents a complete picture of SLM machining conditions for ferrous alloys.

When comparing the processing of titanium parts, it becomes evident that it is costly. Titanium can substitute for more cost-effective steel alloys while still meeting the performance requirements of material components. On the contrary, aluminum alloys, although suitable, do not achieve the same level of performance as steel alloys [280–282]. When choosing process parameters for steel alloys, it is crucial to understand the alloying elements, as they significantly influence achieving the desired mechanical properties of the components. The phase equilibrium of steel alloys is not always known, adding complexity to the process. Managing oxidation is also critical during the SLM process for steel alloys. Elevated temperatures can lead to oxidation, which can affect the final properties of the components. Therefore, effective control and optimization of process parameters, such as laser power, scanning speed, and protective atmospheres, are necessary to minimize oxidation and ensure the desired component quality. Furthermore, the high cooling rate in SLM can result in the formation of different phases, including martensite and austenite, which also play a crucial role in determining the mechanical properties of the steel alloy components. Even slight adjustments to the process parameters can trigger phase changes that can noticeably impact the component's performance in specific applications [283,284].

Table 6. Process parameters considered by researchers during SLM processed for ferrous alloys.

Powder	Laser Beam Diameters [μm]	Laser Power [W]	Layer Thickness [μm]	Hatch Distance [μm]	Laser Type	Scan Speed [mm/s]	Remarks	References
316 L	70	350–425	30	30–90	YLR 500 WC, IPG) 500 W 1070 nm wavelength	400–1000	Preheat at 80 °C to reduce thermal stress, linear energy density (LED) range of 0.535–1.0625 J/mm^3	[285]
304 L	70	200	50	85	200 W Nd-YAG-pulsed laser	800	58.8–76.9 J/mm^3, Highest strain rate sensitivity (m = ~0.0261) compared to SLM SS 304 L. For SLM material, the horizontal and inclined orientations possess higher m values compared to the vertical orientation.	[286]
17–4PH	-	195	30	80	EP-M150 SLM	850	After heat treatment at 1040 °C for 2 h (Air Cool, AC) and ageing cycle at 480 °C for 4 h (AC) for the recrystallization of SLM-produced components; checkerboard scanning strategy	[287]
17–4PH	90	195	20	100	Yb-fiber laser 200 W	2–20	Nitrogen atmosphere: percentage of oxygen 0.8%, 20 mm Scan length,	[288]
17–4PH	200	175	40	80	200 W solid-state Yb-fiber laser	1050	Overnight heating at 80 °C for residual stress releasing, working chamber under nitrogen gas, and ά-martensite and retained austenite (γ) phase formed	[289]
316 L	80	300–380	30-70	80–120	Yb-fiber laser 400 W	800–1200	L9 Orthogonal array-based model applied and relative density 99% almost 7 samples out of 9.	[290]
316 L	--	50–300	20	10–200	YAG-fiber laser	500–2000	Temperature changes and heat during the process on Impress the solidification morphology in tracks, CAVILUX HF with power up to 500 W and a wavelength of 810 nm	[291]
24CrNiMo Low-alloy steel	80	320–340	40	110	Yb-fiber laser with a wavelength of 1070 nm	750–950	76–103.03 J/mm^3 Energy Density (ED) was received, 5–40 μm mico defects found due to increase in energy density when 90.91 j/mme defects occurred, like lack of fusion and ED higher 103.03 J/mm^3 then key holes formed	[292]
Fe–Si–B Alloy (1CP)	80	60–120	50	100–200	YLR-laser	800–1200	50–100 Linear energy density J/m, increasing the value of the offset, a decrease in the density of samples due to a violation of its structural unity caused by the separation of the columnar elements from each other; under a nitrogen-atmosphere-operated machine	[293]
18Ni300 Maraging steel	-	215.91–384.09	50	50–150	Single-mode fiber laser (maximum power output of 500 W)	663.64–1336.36	96.90–99.45% Relative density received; treatment was performed at 850 °C for 1h and subsequent aging treatment was carried out at 500 °C for 6 h, both cool in the air	[294]
Maraging steel	80	258	40	110	Yb-fiber laser 400 W	960	Protective nitrogen gas in the atmosphere, both conditions performed heating and without heating; 900 °C/25 min, water quenched to RT, 490 °C/6 h, with time and temperature variation	[295]

Table 6. *Cont.*

Powder	Laser Beam Diameters [μm]	Laser Power [W]	Layer Thickness [μm]	Hatch Distance [μm]	Laser Type	Scan Speed [mm/s]	Remarks	References
Maraging steel	-	400	40	-	Nd: YAG-fiber laser	800	The point method (PM), line method (LM), area method (AM), and volume method (VM), with the first two being most often used	[296]
Maraging steel	200–500	100	-	-	Continuous CO_2 laser (wavelength–1064 nm	500–1200 mm/min	They performed with and without boron particles; heat input ≤ 8 J·mm^{-1}	[297]
H13 Tool Steel		170–260	30	100		600–1400	83.3–111.1 J/mm^3 Volume energy density received, maximum relative density reached 99.6%, and process parameters were optimized	[298]
H13 Steels, Maraging Steel 18Ni300	80	175–250	Marag. St. 50 μm, H13 60 μm,	Marag. St. 75 μm, H13 80 μm,	Four ytterbium-fibre lasers and a reduced build volume	Marag. St. 1000 mm/s H13 600 mm/s,	An overlap between stripes of 0.6 mm, RBV chamber was kept below 31 ppm, and argon steam (189.3 m^3/h) was continuously applied during operation; they carried out a comparison study	[299]

3.3.1. Microstructural Morphology of SLM Parts in Steel Alloys

Steel alloys typically exhibit the presence of martensite and ferrite, which can be identified using optical emission spectroscopy (OEM) and scanning electron microscopy (SEM). When 17–4PH alloys are processed using SLM, the resulting microstructure often shows a mixture of these phases. Conducted a study on 17–4PH alloys produced via SLM. The microstructure results, depicted in Figure 14 [203,300], revealed the formation of both austenite and ferrite phases. Figure 15 provides a clear visualization of the austenite and ferrite phase formation in the SLM-treated sample [170].

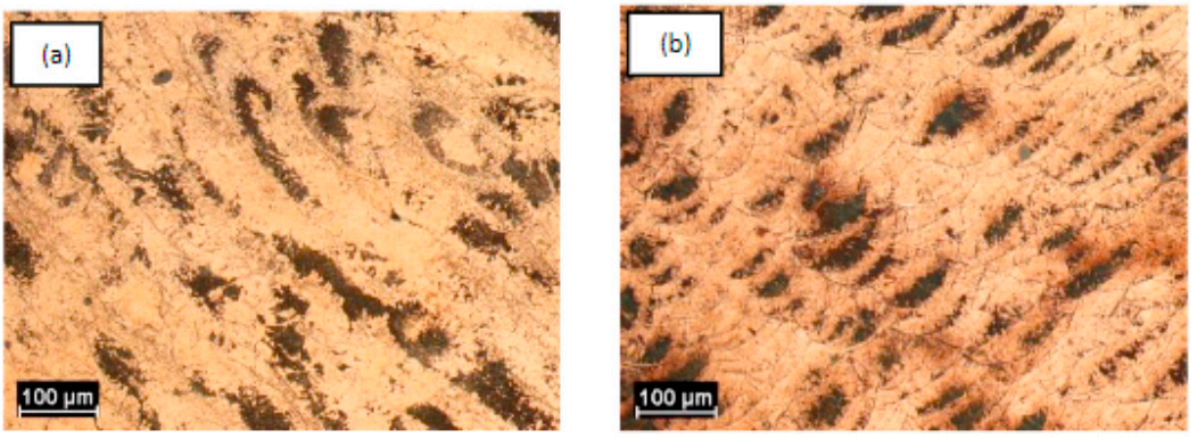

Figure 14. Micrograph representation of 17–4PH alloys (**a**) upper surface; (**b**) longitudinal section (reprinted from Ref. [300], copyright (2019), with permission from Elsevier).

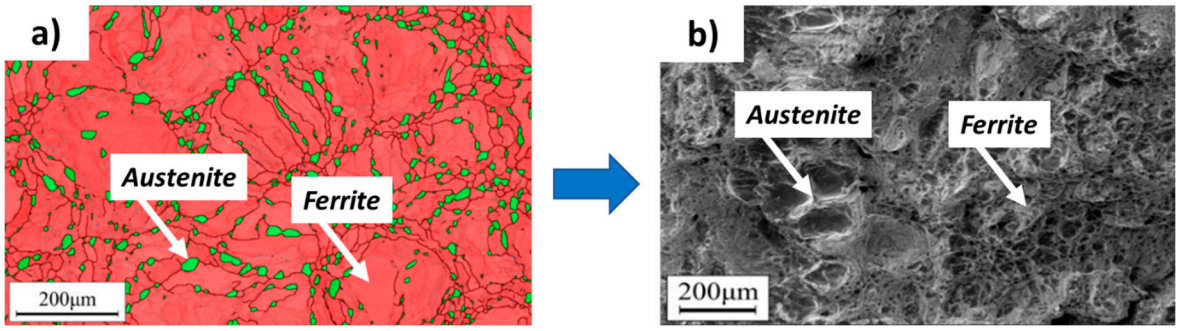

Figure 15. Microstructural features of selective laser melted S32750 duplex stainless steel. (**a**) EBSD Phase distribution of the duplex steel of the sample at side surface (**b**) presented phase at the fracture surface of the sample SEM image Reprinted from Ref. [170].

In contrast, provide valuable insight into the energy density distribution and the effect of laser scanning on microstructure changes in the SLM-treated sample. These results may be necessary for understanding how specific process parameters influence the resulting microstructure of the 17–4PH alloy during the SLM process. In particular, the author also clearly shows grain boundary and phase differences in the microstructure [300]. In Figure 16, It is clear that the volumetric energy input during the LPBF process affects porosity. Each kind of pore was minimized when the hatch distance and scan speed values were close to 100–110 µm and 1100 mm/s, respectively, with `volumetric energy density` (VED) values around 60 J/mm^3. When higher energy densities and reduced scan speeds are employed, the samples are exposed to relatively higher temperatures for extended periods, potentially contributing to the increased development of Widmanstätten austenite. Additionally, Widmanstätten side laths are observed to extend downward into the ferrite grains, originating from the side plate colonies within the vertical substructure laths and extending through the grain boundary austenite [171,214].

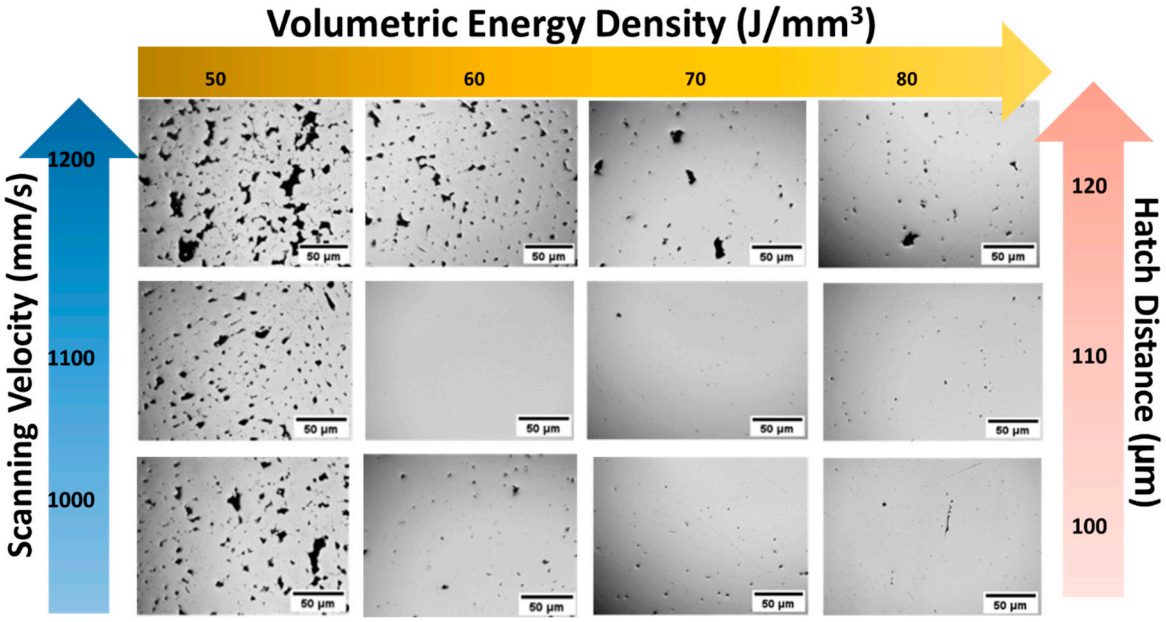

Figure 16. SLM processed of the cross sections of 2205 duplex stainless-steel samples with varying energy densities Reprinted from Ref. [171].

3.3.2. Mechanical Properties of the SLM Parts in Steel Alloys

Ferrous alloys are of great interest worldwide due to their ability to meet mechanical property requirements through different steel alloys [301]. Table 7 presents the mechanical properties of ferrous alloys, such as some stainless steel (SS) and tool steel. The variation in hardness of these samples is mainly attributable to the increase or decrease in the retained austenite volume [302–304]. The highlighted the excellent mechanical properties of 304 L steel produced through the SLM technique, thus generating a strong demand in the biomedical sector [305]. found that a high dislocation density and formation of nitride precipitates contribute to higher yield strength (YS) and tensile strength (UTS). However, the formation of a grain size reduction leads to a decrease in the material's ductility. At the same time, the authors perform a post-deposition heat treatment at elevated temperatures [306]. They found better metallurgical properties.

Other studies demonstrate that a balanced phase is formed following heat treatments, thus generating a balanced distribution of these structures, which can improve their mechanical properties and corrosion behavior [307,308].

Table 7. Mechanical properties of the SLM specimens in ferrous alloys.

Powder Used	UTS (σ_b) [MPa]	YS ($\sigma_{0.2}$) [MPa]	Elongation (δ) [%]	Micro-Hardness [HV]	Remarks	Ref.
PH13–8Mo SS	1282 without Y-direction, 1443 With Y-direction	YS-1264 without Y-direction, YS 1399 with Y-direction	TE 10.2% without Y-direction, TE 12.2% with Y-direction	-	In addition to the yttrium, impact energy, and tensile strength improved significantly due to preventing dislocation movement in plastic deformation	[309]
17–4PH	UTS-AP-751 MPa, UTS-HIP-962 MPa	YS-AP 651 MPa, YS-HIP 858 MPa	-	-	Pore size and morphology can also affect the deformation stability. during plastic deformation; compressive true stress—AP 243.61 MPa, HIP-206.30 MPa	[310]
304 L SS	514.58–694.45	450–650	-	-	Porosity plays a critical factor in fatigue life when porosity is higher than 7–9%, also the roughness is Ra 8.6, 16.27, 21.9, 20.3, and 17.9 µm for different specimens; fatigue strength 500 MPa, (~27.34 mJ/m^2	[311]
304 L SS, 316 L SS	706.7 + −6.2	304 L YS(σy) 454.7 ±11.5 MPa; 316 L, YS 581.1 ± 7.3 MPa	TE 50.3 ± 1.4%; UTS 704.1 ± 2.5 MPa	17.5 ± 3.7 HV 304 L and 239.6 ± 6.6 HV 316 L; TE 54.8 ± 2.3% 304 L	4.9 µm 304 L and 16.7 µm 316 L grain size, impact energy 304 L 2.86 ± 0.17 GPa, 316 L 3.12 ± 0.14 GPa	[312]
17–4 PH	~950–1200	YS-~850–1150 MPa	TE-~15–25%	26–47HRC,	To utilize nano-sized TiN particles both as inoculants to obtain an equiaxed microstructure in an as-built condition and as dislocation barriers to improving mechanical properties	[313]
316 SS	~360–475	YS-~180–200	TE- ~12–35%	-	Vacuum atmosphere during the sintering an increasing of density up to 6%, of real strain up to 150%, and UTS up to 23% is observed	[314]
15–5PH	-	TOP-YS 734 ± 32.5, MIDDLE-YS 836.8 ± 29.4, BOTTOM-YS 944.0 ±12.0	Uniform EL % 8.9 ± 0.1, 9.0 ± 0.1, 9.2 ± 0.1; EL % 19.5 ± 0.4,19.8 ± 1.0, 20.0 ± 0.6	-	The variations in oxide volume fraction led to a decreased yield strength along the height and a high amount of austenite at the specimen bottom contribute to external plasticity and elongation	[315]
316 L SS	610–620	YS-375-510MPa	~40–50	-	HIP heat treatment contributes to a reduction of about 22% percent in the yield strength from 500.1 MPa to 392.2 MPa, and an increase in the ductility and elastic modulus of the modulus material by around 10% percent; Poisson's ratio 0.25–0.30, Yang's elastic modulus, GPa 130–160, fatigue strength-σmax > 250 MP	[316]
316 L SS	TS- 300	~573	48	-	A strength of ~720 MPa and EL of 48% is obtained in the transversal direction; the corresponding properties of the longitudinal counterpart are ~615 MPa and 18% EL.	[317]
17–4 PH	720 MPa; longitudinal 610 MPa	570 MPa; YS of 510 MPa,	EL of approximately 48%; and EL of approximately 18%	~250–290 HV	17–4PH alloys are limited due to defects and anisotropy	[318]

Table 7. *Cont.*

Powder Used	UTS (σ_b) [MPa]	YS ($\sigma_{0.2}$) [MPa]	Elongation (δ) [%]	Micro-Hardness [HV]	Remarks	Ref.
H13 tool steel	Long. Dir.-UTS ~1600 MPa; Trans. Dir.-UTS of 1200 MPa	-	-	elongation to fracture of ~2% along the longitudinal direction; EL of ~1.4% along the transverse direction	The carbon-enriched retained γ (austenite) films amongst martensite blocks transferred to high-carbon twin martensite through stress-induced martensitic transformation upon plastic deformation, leading to high susceptibility to cracking	[319]
CrMn–MS1	~2005 $\pm$ 68 MPa	YS-~1190 $\pm$ 50	6.9 $\pm$ 0.5	362 $\pm$ 9 HV0.05	A good interface transition, CrMn–MS1 steel displays strong metallurgical bonding at the interface,	[320]
SLM–MS1	986 $\pm$ 30	1071 $\pm$ 25	7.9 $\pm$ 0.5	360 $\pm$ 9 HV0.05	High relative density of >99.5%, porosity of less than 0.5 vol.-%	[321]
M3:2 high-speed steel	-	-	-	650–950 HV	Preheating temperatures of 200 °C or 300 °C are necessary for low crack density; the hardness tempering behavior of the SLM-densified material is promising	[322]
H13 tool steel	YS-1400, 1432 MPa,	UTS 1700 MPa; 1715 MPa,	elongation 1.5%	552 HV	The effects of porosities and unmelted powders on mechanical properties are also elucidated by the metallic fractography analysis to understand tensile and fracture behavior	[323]

3.3.3. Corrosion Behavior of SLM Parts in Ferrous Alloys

Like non-ferrous alloys, SLM processing can significantly impact the microstructure, phase composition, and defects of ferrous alloys. These alterations, in turn, play a crucial role in influencing the corrosion behavior of the SLM-processed ferrous alloys. Ferrous alloys have excellent sustainability; adding specific elements can further improve their properties.

Research shows yttrium oxide layers and the treatment of solid solution to enhance the anti-corrosion properties. The results indicated that the composite alloys, with the addition of yttrium oxide, exhibited significantly improved anti-corrosion behavior and formed a more effective passive layer on the surface than pure alloys [324].

It is focused on SLM-processed steel samples to investigate steel alloy corrosion phenomena. They observed that the re-austenitized SLM-processed steel showed a remarkable absence of MnS inclusions, in contrast to the wrought steel, where the presence of MnS inclusions destabilized the passive film on the material's surface [325].

It is found that 316 L stainless steel (SS) samples manufactured by SLM with lack-of-lasering (LOL) micro-holes exhibited significant susceptibility to localized corrosion. This was evident from the lower breakdown potentials observed in the polarization corrosion examination. Figure 17 displayed the corrosion anodic and cathodic reactions, providing valuable insights into the corrosion mechanisms. Moreover, the authors perform heat treatments (HT) at two different temperatures, 950 and 1100 °C [326,327]. The metallographic phase and pits of the as-received and heat-treated samples are shown in Figure 18. It can be observed that Figure 18 illustrates the pitting initiation locations in the samples as follows: In the as-received samples, pitting initiation occurred at the MPBs (Figure 18a). In the HT950 samples, pitting was initiated at the GBs due to the dissolution of MPBs (Figure 18b). Similarly, in HT1100 samples, the primary pitting sites were observed at the GBs (Figure 18c) also in the (Figure 18d) bagraph shows the number of pits formation versus types of the samples as discussed [328].

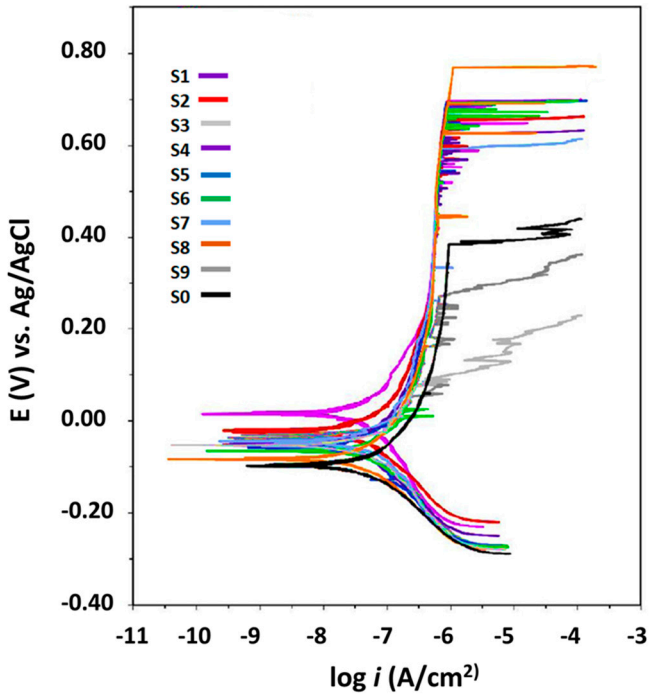

Figure 17. Potentiodynamic polarization curves were obtained for SLM-manufactured and commercially available 316 L stainless steel samples in a 0.6M NaCl solution at room temperature (reprinted from Ref. [326], copyright (2020), with permission from Elsevier).

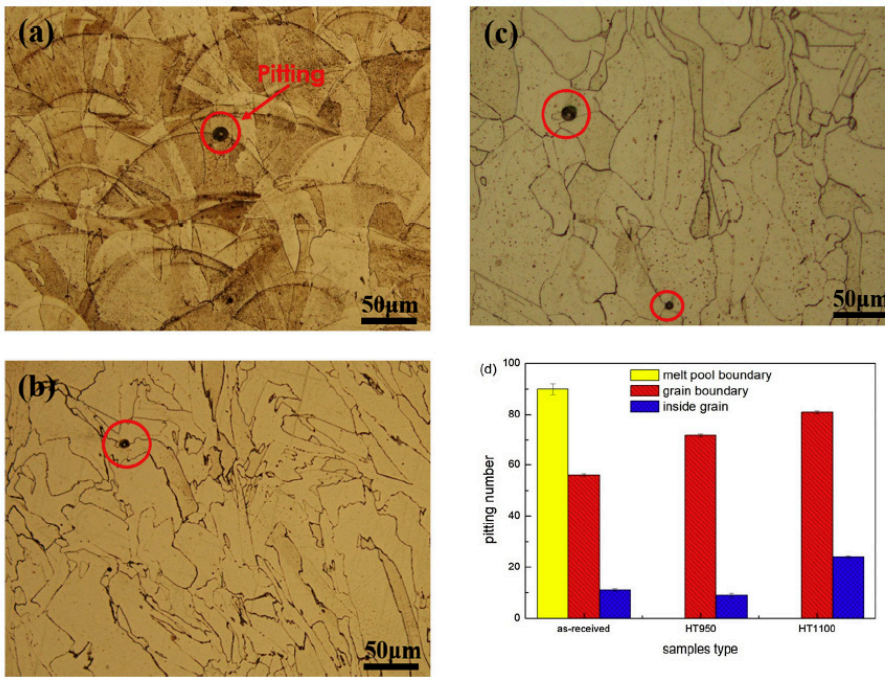

Figure 18. Metallographic phase and pits of the (**a**) as-received, (**b**) HT950, and (**c**) HT1100 samples. (**d**) Statistical chart of the number of pit sites (reprinted from Ref. [328], copyright (2020), with permission from Elsevier).

Furthermore, investigated the corrosion behavior of 30CrMnSiA steel by performing tests in a salt spray chamber, as depicted in Figure 19. This aspect garnered significant attention due to the formation of micro-pits and density changes. With increased exposure hours, pits and surface changes escalated considerably compared to the observations in Figure 19a–d [327]. Also, conducted a similar study, stating that lower grain boundary angle density and the presence of pitting with element segregation and reprecipitates are the main factors contributing to the decrease in corrosion resistance of steel alloys. Microstructure analysis revealed pitting on SLM-machined steel alloys under various conditions, further supporting their findings on the corrosion behavior of these materials [327,328].

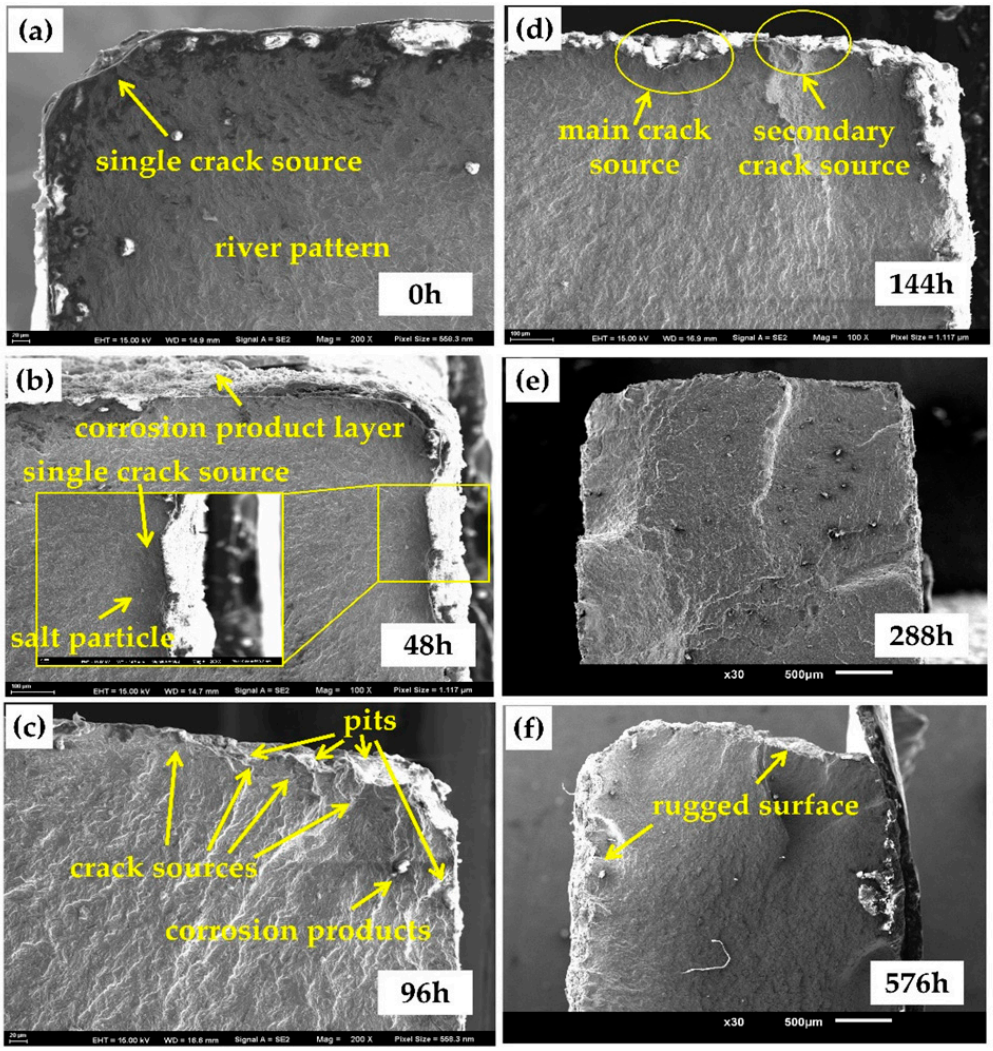

Figure 19. The micromorphology of SLM 30CrMnSiA steel after salt spray test for different periods and the morphology of the fatigue crack initiation (**a**) 00 h (**b**) 48 h (**c**) 96 h (**d**) 144 h (**e**) 288 h (**f**) 576 h; Reprinted from Ref. [327].

4. Mathematical Modelling and Simulation for SLM

In the current context, numerical mathematical modeling has proven highly versatile in different disciplines, especially in additive manufacturing (AM) processes. Its ability to deliver simulated results offers valuable insights into the practical behavior of manufactured components [329]. Through numerical modeling, it is possible to acquire a wide range of information for alloys manufactured via SLM, such as thermal behavior, material flow, and mechanical properties [330], obtaining efficient and accurate results with a margin of error of about ±5%. These analyses can effectively account for various factors, including particle bonding, temperature conditions, laser power, and other minor or significant parameters. However, accurately defining specific powder properties and behavior during melting at elevated temperatures demands careful attention during finalization. Various methods are accessible for efficiently managing process parameters in computer-based analysis. These include utilizing the finite element method (FEM) and software tools like MatLab and Abaqus, which are proficient in high-speed computations [331,332]. Generally, the process involves numerous steps, which can be time-consuming. However, by carefully selecting the appropriate powder and utilizing various mathematical SLM modeling techniques, it is possible to create an artificial environment that closely mimics actual experimental conditions. This allows users to achieve results nearly identical to those of physical experimentation.

The critical mathematical SLM modeling techniques employed in this process include the following:

1. Heat conduction model: To simulate heat transfer during the SLM process.
2. Laser beam model: To replicate the behavior of the laser beam as it interacts with the powder.
3. Fixed domain method: To define and analyze the specific region of interest in the model.
4. Temperature-transforming model: To predict the temperature changes and transformations during the process.
5. Residual stress model: To account for the stress and deformation present in the fabricated components after the process.
6. Finite Element Formulation: To discretize the model and solve complex equations efficiently.

By integrating these techniques, the mathematical SLM modeling process becomes a powerful tool for achieving reliable and comparable results to real-world experimental conditions [333].

4.1. Heat Conduction Model

The heat generation model consists of two distinct parts: the heat conduction equation (which neglects fluid flow conditions) and the Navier–Stokes equation (which considers fluid flow conditions). The heat transmission model ensures thermal energy equilibrium by considering linked boundaries and initial conditions. The Fourier Equation (1) can accurately determine the heat transfer process during the experimental procedure.

$$q = -k\Delta T \tag{1}$$

where q (W/m^2) is the transferred heat amount, k (W/mK) is thermal conductivity, and ΔT (Kelvin K) is the temperature gradient. When the powder particles melt and turn into liquid, they contribute to the heat of convection in the system. The energy equation incorporates this additional heat transfer phenomenon as a transport term. Considering this term, the Navier–Stokes equation can be readily applied to calculate and analyze fluid flow. This approach allows for a more comprehensive and accurate representation of the system's heat transfer and fluid flow dynamics. During the AM process's layer-by-layer heat transfer and cooling process, formation and phase changes can be effectively described using a governing equation known as the Stefan condition. This condition is applied separately for the two phases involved, i.e., solid and liquid. The Stefan condition (2) accounts for mass and thermal diffusion at the interface between the solid and liquid phases, providing a mathematical framework for understanding and modeling the phase transitions that occur during the additive manufacturing process.

$$K_s \frac{\partial T_s}{\partial n} - K_l \frac{\partial T_l}{\partial n} = L_\rho \frac{ds}{dt} \tag{2}$$

where k_s and k_l represent the thermal conductivities, respectively; T_s and T_l are the temperatures of solid and liquid, respectively; ρ is the density, L is the latent heat, and s is the solid–liquid interface location [334]. In addition, the derivation of Fourier thermal conduction helps analyze the evolution of heat transfer and heat in SLM. The boundary conditions for heat flow involve conduction and convection within the gaseous environment, considering the components produced on the base plate and the adjacent powder layers above and below. The transient spatial heat distribution satisfies the governing equation, expressed as T (x, y, z, t). This equation comprehensively explains how temperature varies concerning spatial coordinates (x, y, z) and time (t) during the SLM process. The thermal loss, represented in Figure 20, mainly accounts for the conduction-related issues. The following specified equations are dedicated to the thermal field of the SLM mathematical model and are related to conduction and heat loss. It is presumed that the maximum heat

loss occurring in the powder bed due to conduction, convection, and radiation does not occur significantly; hence, it can be neglected to maintain computational efficiency without compromising accuracy.

$$\rho C_p \frac{\partial T}{\partial t} = \nabla.(K\nabla T) + Q \text{ on } \Omega \quad (3)$$

$$T(x, y, z, 0) = T_0 \frac{\partial T}{\partial t} \text{ on } \Omega \quad (4)$$

$$-k\frac{\partial T}{\partial n} = \varepsilon_0 \sigma\left(T^4 - T_e^4\right) + h(T - T_e) \text{ on } \Gamma_g \quad (5)$$

$$-k\frac{\partial T}{\partial n} = 0 \text{ on } \Gamma \quad (6)$$

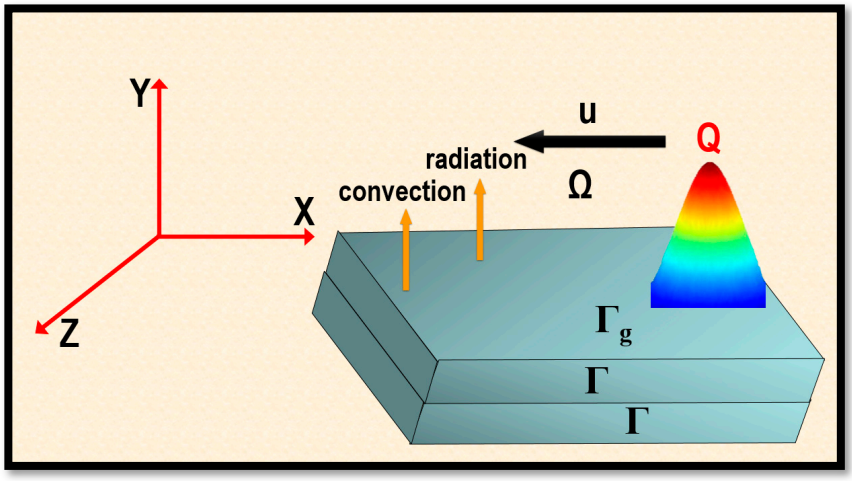

Figure 20. Heat conduction problem formulation Reprinted from Ref. [334].

In the conduction equation (Equation (3)), the laser heat source is represented by the variable Q, which acts as a power source of internal energy. This heat source term Q accounts for the energy input provided by the laser during the SLM process, contributing to the overall thermal field and temperature distribution within the material being processed [334].

4.2. Laser Beam Model

The laser beam model plays a critical role in the SLM process, impacting the temperature variation within the system. It is influenced by various essential characteristics, including laser beam dimensions, traveling speed, power, and the specific laser source used. These parameters can be adjusted based on the chosen materials and powder properties to optimize the SLM process. One of the main concerns in the laser beam model is the irradiation of the powder surface, which is typically measured in watts per square meter (W/m^2). Additionally, the volumetric laser beam unit is measured in watts per cubic meter (W/m^3), while surface measurements are expressed in watts per square meter (W/m^2). These different units are used to understand the energy distribution and intensity of the laser beam during SLM, ensuring precise control over temperature profiles and enabling successful additive manufacturing.

The temperature field distribution of the powder bed is strongly influenced by the characteristics of the laser beam, such as laser power, beam radius, laser speed, etc. Different choices of laser beam irradiation models can be found in the literature, but most of them are surface (W/m^2) rather than volumetric laser beam models (W/m^3) due to the minimum layer thickness of the powder (30–100 μm). The cylindrical model of the laser beam assumes that the laser beam is constant at every point of the spot surface. In this case, the surface heat flux can be written as follows (Equation (7)). The cylindrical model of the laser beam incorporates laser power (P) and laser beam radius (R) as essential parameters. This model

describes how the laser beam interacts with the powder material, and the generated heat flux from the laser is absorbed by the powder during the SLM process.

$$q_{cyl} = \frac{P}{\pi R^2} \tag{7}$$

$$q_{cyl} = \frac{\alpha P}{\pi R^2} \tag{8}$$

where α represents the absorption coefficient of the irradiated material, which is typically heat-dependent. Figure 21 illustrates the temperature changes during the SLM process as simulated by the model. The color-coded representation of the powder particles makes it easy to identify their states. Blue powder particles indicate the normal state, while yellow and red represent highly heated or melted particles due to the laser beam. Light green and sky-blue colors indicate heat-affected particles. The laser beam moves quickly across the surface of the powder bed, making it challenging to observe the process of one complete surface layer being completed in a matter of seconds. The immediate motion of the laser beam and its intense heat cause rapid changes in temperature and material state, contributing to the efficiency and effectiveness of the SLM process [335].

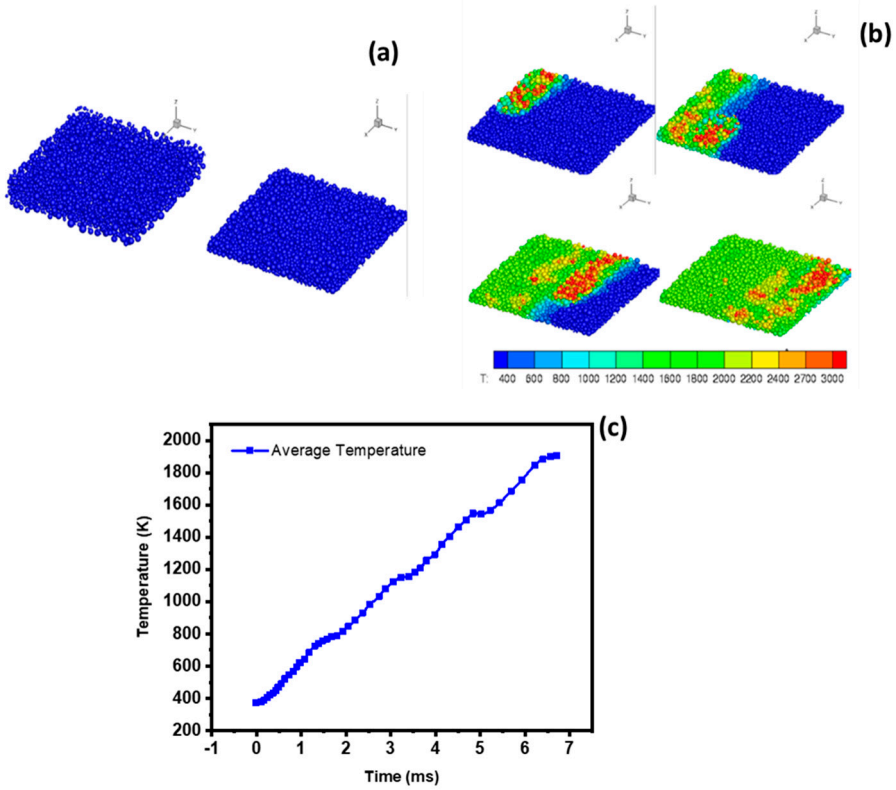

Figure 21. (**a**) Deposition (top row) and (**b**) subsequent laser sintering of a 2 mm × 2 mm box of powdered materials, colors represent temperature (scale ranges from 400 to 3000 K); (**c**) temperature v/s time graphical representation in microseconds (reprinted from Ref. [336], copyright (2014), with permission from Elsevier).

4.3. Simulation for Al Alloys Produced via SLM

Using SLM thermomechanical models and simulations can be very useful to avoid unnecessary experimental failures. These simulations allow researchers to gain valuable insights and optimize process parameters [337]. The simulation of aluminum alloys processed by SLM is relatively complex due to two main factors: volume shrinkage and material evaporation. Manufacturers can achieve the desired balance between processing efficiency and part quality in the SLM process by carefully selecting and optimizing trial

simulation parameters, including scan speed, laser power, and layer thickness. At the same time, it is essential to use specific models to obtain accurate results in line with the desired results for the proposed materials. According to higher laser power and slower scan speeds were associated with increased laser penetration and width. Conversely, lower power settings and faster scan speeds improved penetration and width per unit of energy, which also translates to higher energy efficiency. It is worth noting that simulating a single-stage scanning strategy is comparatively more straightforward than simulating a multistage scanning strategy. Furthermore, the authors were involved in a parametric investigation to understand the correlations between power levels, evaporation, melting, and temperature distribution through analysis. Instead, the study of AlSi10Mg alloys, specifically analyzing part-scale deformations [329,337].

Nowadays, one of the most widely used software programs to simulate complex mechanical behaviors and thermal effects in metal components is the COMSOL Multiphysics™ software.

Specifically, when performing mechanical and thermal simulations of the metal component with COMSOL Multiphysics TM software, distinct governing equations and the appropriate mechanical framework are used for modeling. Below are the governing equations and heat transfer models based on these simulations [329].

$$\rho C_p \frac{\partial T}{\partial t} = \nabla.(-K\nabla T) \tag{9}$$

where t is the time, T is the temperature, ρ the density, $C_{p\ is}$ the specific heat capacity, and K is the material's thermal conductivity. The following equations can effectively represent the phase and temperature variation changes from the above parameters.

$$K = \theta K_{phase1} + (1-\theta)K_{phase2} \tag{10}$$

$$C_p = \theta C_{p.phase1} + (1-\theta)C_{p.phase2} + L_{f/v}\frac{d\alpha}{dT} \tag{11}$$

$$\rho = \frac{\theta\rho_{phase1}C_{p.phase1} + (1-\theta)\rho_{phase2}C_{p.phase2}}{\theta C_{p.phase1} + (1-\theta)C_{p.phase2}} \tag{12}$$

In these mathematical expressions, θ signifies a volumetric parameter with values ranging from 0 to 1. Additionally, the transition interval denoted by α is a smoothed function within COMSOL, representing the fraction of phase post-transition.

In the initial phase, characterized by stages 1 and 2 as outlined in Equations (2)–(4), these stages are associated with the liquid and solid states. In the subsequent phase transition, Equation (10), as previously discussed, accounts for the latent heat of fusion (Lf) and evaporation (Lv).

$$\rho_{power} = (1-\theta)\rho_{bulk} \tag{13}$$

$$K_{power} = K_{bulk}(1-\theta)^n \tag{14}$$

where ρ_{powder} and K_{powder} are the material density and thermal conductivity, respectively, while porosity is zero, θ is the powder porosity, and it is calculated to be 0.43, and n is the empirical parameter taken as 4 [338].

The variables ρ and K refer to the characteristics of the powder layer during the phase change process and are defined in the equations below [338]:

$$\rho = \frac{\rho_{bulk}(T_m) - \rho_{powder}(T_s)}{T_m - T_s}(T - T_s) + \rho_{powder}(T_s), T_s < T < T_m \tag{15}$$

$$k = \frac{k_{bulk}(T_m) - k_{powder}(T_s)}{T_m - T_s}(T - T_s) + k_{powder}(T_s), T_s < T < T_m \tag{16}$$

where, ρ_{bulk} and k_{bulk} denote the bulk density and thermal conductivity, respectively.

These equations analyze aluminum alloys, specifically those in the 6xxx series. In this context, ρ, $C_{p,}$ and k_{bulk} are essential to studying latent heat fusion, melting, and sintering points. These values are determined based on research conducted for the heat radiation from the material surface within the chamber to its surroundings, as illustrated in Equation (16).

$$q_{radiation} = \varepsilon\sigma(T^4_{amb} - T^4) \tag{17}$$

In this context, ε and σ represent surface emissivity and the Stefan–Boltzmann constant. Likewise, the critical computational command involves homogenization through volume averaging analysis to establish the non-linear meso and macro relationships for structural properties. The indicated equations below enable the measurement of macroscopic stress and strain [339,340]:

$$\sigma' = \frac{1}{V_{RVE}} \int_{V_{RVE}} \sigma^* dv \tag{18}$$

$$\varepsilon' = \frac{1}{V_{RVE}} \int_{V_{RVE}} \varepsilon^* dv \tag{19}$$

where σ' and σ^* represent the macroscopic and microscopic stress, while $\varepsilon'$and ε^*correspond to the macroscopic and microscopic strains. Additionally, "V_{RVE}" denotes the representative volume element [341]. Researchers conducted a comprehensive study involving the finite element method (FEM), thermal analyses, and phase transformation analysis. They proposed that the solidus temperature (Ts) undergoes rapid changes concerning the melt pool temperature at a given time. However, as the laser energy increases, the cooling percentage decreases. In the SLM system, this decrease in cooling percentage occurs when the central melt pool is cooled. Furthermore, the deposition of the powder layer by layer is influenced by heating effects, which contribute to phase changes and microstructural alterations [342].

4.4. Modeling and Simulation of Ti Alloys Manufactured Using SLM

The melting temperature within the processing chamber primarily influences part fabrication using titanium and its alloys through SLM. In numerical modeling, simulations can be conducted using Ansys Parametric Design Language (APDL).

The term "systematic" can be synonymous with "governing", but various researchers have focused on deriving different equations to analyze the system. For instance, they have employed Euler backward and the Newton–Raphson iterative approach [343]. In certain aspects of SLM, the system exhibits a rapid thermal mode that can influence slight modifications in the geometry of the laser-induced surface. However, temperature variations occur among powdered surfaces, and convection and radiation occur between particles and trapped air. The author employs the following equation to describe the heat flux generated by the model and the continuous laser beam, which does not depend on a Gaussian distribution.

$$q = \frac{2AP}{\pi r_b^2} \exp\left(\frac{-2r^2}{r_b^2}\right) \tag{20}$$

Equation (20) defines a mathematical expression to quantify the generated heat flux density.

$$q_m = \frac{1}{\pi r_b^2} \int_0^{r_b} q(2\pi r)dr = \frac{0.865AP}{\pi r_b^2} \tag{21}$$

where P represents the laser power, A stands for the absorption coefficient of the preplace layer, which is typically constant within the range of 0.2 to 0.3, and r_b denotes the laser beam diameter, and its values can vary as defined parameters [344].

In addition, latent heat can be expressed as an enthalpy equation in the SLM process,

$$H = \int \rho c(T)dT \tag{22}$$

Various methods exist to analyze this expression, but a well-structured Figure 22 can offer better clarity. In the context of SLM part fabrication, it is important to note that within a few microseconds, the powder particles transform into a solid layer phase with the depicted ultimate properties, as shown in Figure 22 [345,346].

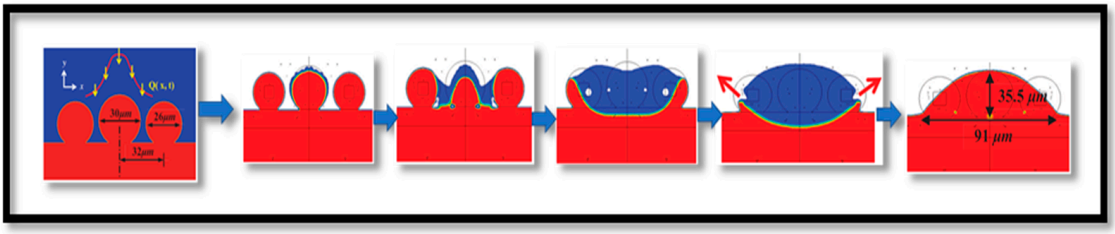

Figure 22. The layout depicts the melting of powder particles, transitioning from individual particles to a molten state through a melting loop under the influence of laser heat (reprinted from Ref. [346], copyright (2016), with permission from Elsevier).

In Figure 23, the simulation illustrates the solid powder particles and their transformation into a molten state. This simulation considers heating parameters and the distribution of powder particles, which are mathematically modeled. conducted a study involving mesoscale modeling and thermal analysis of Ti alloys, where they observed that as the single laser scanning trace developed, it led to non-uniform shapes with increased powder layer thickness and higher laser scanning speeds. Additionally, they noted that heat dissipation increased with a thicker powder layer. It was attributed to the increasing melting and evaporation, which could lead to a greater Marangoni force and recoil pressure, ultimately causing the molten powder flow to become destabilized [347].

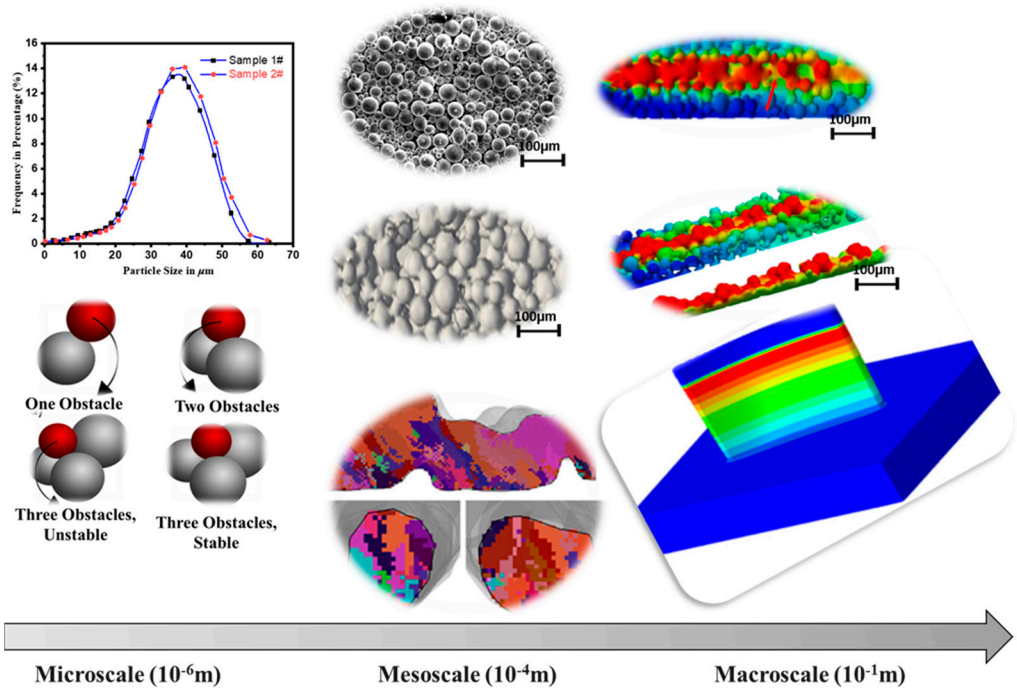

Figure 23. A multi-scale materials approach to modeling SLM in titanium alloys (reprinted from Ref. [347], copyright (2017), with permission from Elsevier).

One of the significant phenomena in the solidification process of melted powder particles in SLM is the alteration of microstructure. These multiple changes in microstructure have an impact on the mechanical and microstructural properties. researched microstruc-

tural modeling of Ti alloys, which involved the utilization of heat conduction equations to investigate these changes [348].

$$\rho C_p \frac{\partial T}{\partial t} = (\lambda_x \frac{\partial T}{\partial x}) + \frac{\partial}{\partial z}(\lambda_z \frac{\partial T}{\partial z}) + q \quad (23)$$

where T is the temperature; ρ is the density; C_p isthespecificheat, λ_x and λ_z are the thermal conductivity is in two directions; and x, z, and q are the volumetric heat. It is a common heat source, considering that most powder laser modeling uses a moving Gaussian heat source.

$$q(x,z) = \frac{2AP}{\pi\omega^2}\exp\left[-2(\frac{x^2+z^2}{\omega^2})\right] \quad (24)$$

where A is the laser absorptivity coefficient of the material, P is the laser power, and ω is the laser beam radius. The period (τ) denotes the laser beam retained in several locations.

Moreover, within Rappaz's proposed numerical model for non-uniform microstructure nucleation, the grain density (ng) is determined as a function of undercooling (ΔT), as expressed in the formula below [349]:

$$\frac{dn_g}{d(\Delta T)} = \frac{n_{max}}{\sqrt{2\pi}.\Delta T_\sigma}\exp\left[-(\frac{(\Delta T - \Delta T_{max})^2}{2\Delta T_\sigma^2})\right] \quad (25)$$

where, ΔT_{max} is the mean nucleation undercooling (ΔT_{max} = 2 °C) ; ΔT_σ is the standard deviation (ΔT_σ = 0.5 °C); and n_{max} signifies the maximum density of nuclei within this integral distribution from 0 to ∞ ($n_{max} = 5 \times 10^{14} m^{-3}$) [349,350]. Additionally, the grain density can be described by:

$$n_g(\Delta T) = \frac{n_{max}}{2}\left[\tanh(\frac{(\Delta T - \Delta T_{max})}{1.25\Delta T_\sigma}) + \tanh(\frac{(\Delta T_{max})}{1.25\Delta T_\sigma})\right], \quad (26)$$

In general, the KGT (Kurz–Giovanola–Trivedi) model can be used to calculate the relationship between the advancement of grain velocity (V(ΔT)) and the degree of system undercooling (ΔT) [349,350]

$$V(\Delta T) = A_\beta \Delta T^2 + B_\beta \Delta T^2 \quad (27)$$

where the constants $A_\beta$and$B_\beta$are equal to the values of 0.544×10^{-4}) [351]. The previously mentioned formulas represent the numerical microstructural model that researchers adopted from [347]. There are several important considerations, including the following:

1. Exclusion of heat transfer via convection and radiation;
2. Consideration of heat generation and rapid solidification within a gaseous environment;
3. Nucleation and growth of grains occurring at the same cooling temperature;
4. Particular attention to martensite formation in Ti alloy specimens, both in the longitudinal and transverse directions [352,353]. These aspects are considered cutting-edge by researchers.

In the context of Ti alloys, numerous research methods and analyses have been explored by various researchers, each focusing on distinct strategies and simulations. It also investigated residual stress profiles using simulations and the contour method. Multiple approaches to stress profile analysis have been explored, emphasizing the inherent-strain-based method, subsequently validated using the contour method [354].

In Figure 24, it can be observed that higher residual stresses tend to form predominantly on the surface edges of the specimens. In Figure 24a, the data presented represent the averaged data of two cut halves, resulting in a sufficiently smooth and relaxed surface profile. Figure 24b displays contour stress maps for two titanium cantilever samples. Figure 24c reveals tensile residual stress occurring in the sample build-up direction, which is from one layer upward to the next and can be observed at its mid-height along the edges

of the samples. Compared to other locations within the sample, high tensile residual stresses are notably present along line 1. Figure 24f highlights the specific locations within the samples where the highest tensile residual stresses were observed, predominantly around the starting and ending points of line 1. In Figure 24d,e,f line profiles of the residual stress are presented, allowing for a comparison between the results obtained through numerical simulation and the contour method for the titanium (Ti6Al4V) coupon, as demonstrated by the author. Additionally, tensile residual stresses are generally more pronounced in the build direction and on the outer surfaces of the Ti alloy specimens [354].

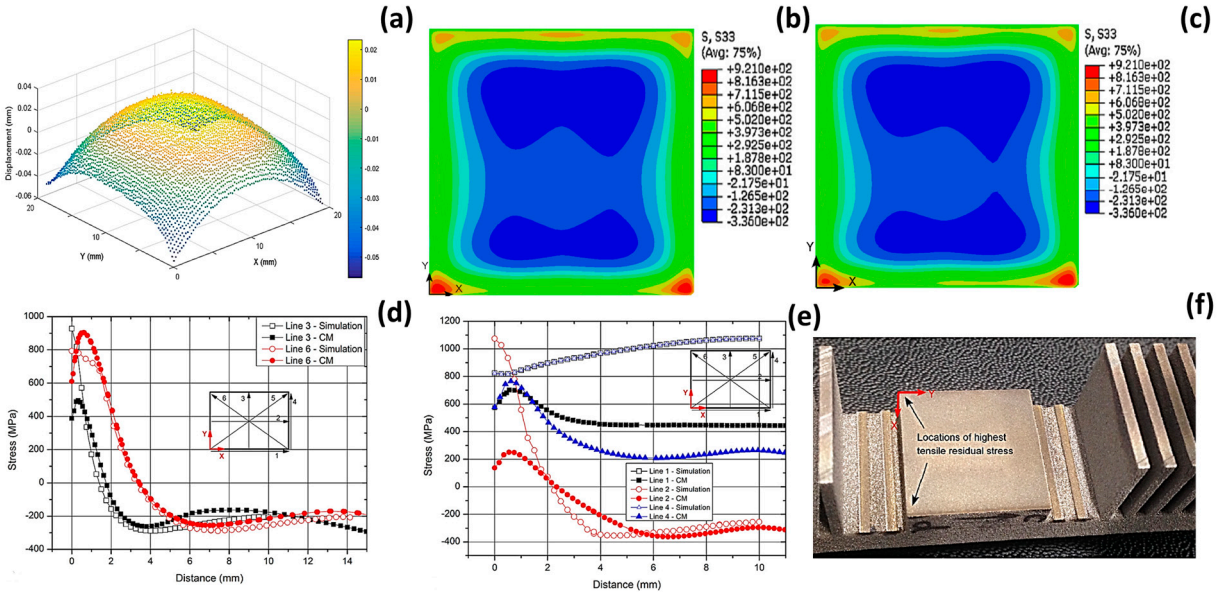

Figure 24. Residual stress profile layer-by-layer analysis of Ti alloys specimens: (**a**) surface displacement Isometric profile of titanium (Ti6Al4V) cantilever specimen, (**b**,**c**) comparison of contour stress maps of titanium (Ti6Al4V) cantilever sample (**d**,**e**) titanium (Ti6Al4V) specimen simulation and contour method of stress profiles for the (different lines) shown figure (**f**) residual stress is higher in the center of the cantilever specimen (reprinted from Ref. [354], copyright (2018), with permission from Elsevier).

4.5. Modelling and Simulation of Ferrous Alloys Manufactured Using SLM

There is a wide range of steel alloys, and numerous publications are available that delve into their mechanical and microstructural properties through numerical modeling analysis. Various avenues exist to gather comprehensive information about steel alloys. One notable approach for fracture analysis of tensile specimens produced via SLM uses the Johnson-Cook damage model. The mathematical analysis results regarding 17–4PH alloys processed using SLM provide valuable insights into the actual properties exhibited by the manufactured specimens. In this context, exploring the thermal properties and structural morphologies is imperative. Figure 25 serves as an adequate representation of the thermal characteristics of the specimens, aiding in the comprehension of the cooling process.

Additionally, the micrograph shows the heating zones, showcasing the layer-by-layer bonding, heat-affected zones, and grain growth, which are well illustrated in both simulated and experimental images [355]. Furthermore, Researcher conducted a study involving a multiphysics numerical model for steel alloys processed through SLM. The governing equations employed in their research resemble the previously discussed ones, highlighting the multidisciplinary nature of investigations in this field [356].

$$\rho C_p \frac{\partial T}{\partial t} + \rho C_p^* u.\nabla T = \nabla.(k\nabla T) + AQ_{Laser} + Q_{Rad} + Q_{ev} \quad (28)$$

where ρ is the density in kg/m^3, C_p^* is the modified specific heat capacity in J/kg.K, T is the temperature in K, t is the time in s, u is the velocity in m/s, k is the absorption coefficient, A is the thermal conductivity in W/(mK), Q_{Laser} is the input laser energy source in W/m^3, Q_{Rad} is the radiated energy source in W/m^2, and Q_{ev} is the evaporation heat loss in W/m^3. A critical aspect to emphasize is selecting an appropriate heat source, which significantly facilitates the validation of thermal properties. These investigations provide insights into mechanical and microstructural properties, which the shape of the build specimen can notably influence, whether in the x–y or y–z direction. For instance, in models like the Gaussian 2D and 3D models, the analysis includes considerations of laser penetration into the powder, offering a comprehensive view of the thermal and structural dynamics during the additive manufacturing process [357,358].

$$Q_{\text{Laser}} = \nabla \frac{I_0}{b} \exp\left(\frac{-2r^2}{r_0^2}\right) \exp\left(\frac{z - z_0}{b}\right) \tag{29}$$

$$I_0 = \frac{2P}{\pi r_0^2} \tag{30}$$

where I_0 is the intensity of the laser beam axis (W/m^2), b is the penetration distance of the laser beam (m), r is the distance from the point to the center of the beam (m), r_0 is the radius of the laser beam (m), z is the vertical position of the power (m), z_0 is the position of the top of the powder (m), and P denotes the laser powder in (W). Researchers in the field of SLM have made significant advancements in their processing techniques. Many have undertaken a thorough examination of various models, with a particular focus on addressing both minor and critical factors. These factors include considerations related to volumetric changes occurring during temperature fluctuations caused by the laser and the influence of energy and gaseous environmental effects on the process. Equations (28)–(30), presented in the research, offer comprehensive elaboration on the Gaussian governing equation (Equation (28)) and the multiphysics model. These equations serve as valuable tools in capturing the intricate dynamics and interactions during SLM processing, allowing researchers to understand the underlying principles and contributing factors.

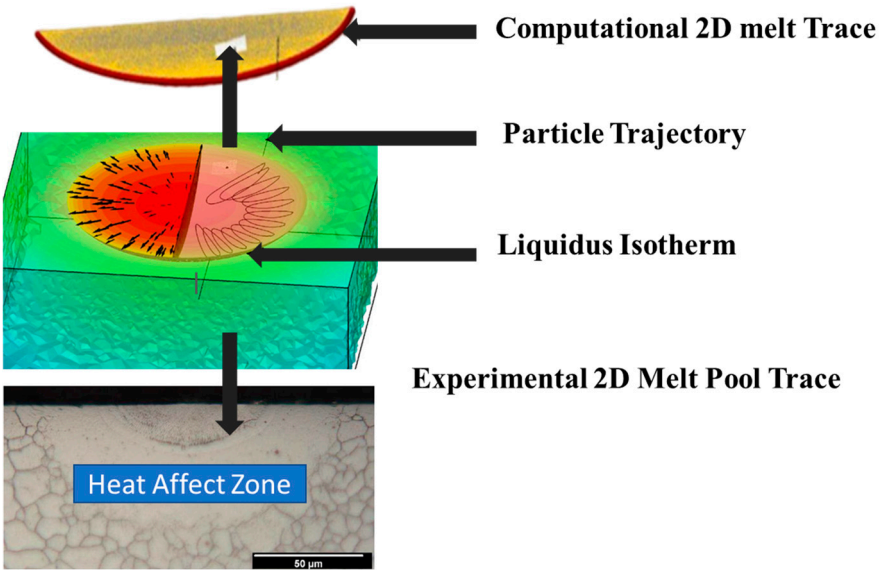

Figure 25. Thermal conditions of the specimen built by SLM-simulated and experimental specimen micrograph view Reprinted from Ref. [355].

5. Applications and Limitations for Various Alloys from the SLM Process

SLM offers immense potential for various applications due to the wide range of alloys available. As already mentioned, each alloy has distinct mechanical and metallurgical characteristics. This diversity in alloy properties provides significant opportunities for using different materials in various fields of application. For example, aluminum alloys emerge as exceptionally versatile materials, suitable for a broad spectrum of applications. As discussed in prior sections, their adaptability stems from their lightweight nature, which does not compromise the necessary strength demanded by various applications. This characteristic allows for maximum utilization of aluminum alloys across diverse industries. Figure 26 visually demonstrates how aluminum alloys can be employed in constructing structural frames and assembly components. The SLM process facilitates the creation of uniform single-frame components, enabling the assembly of intricate structures and systems. In addition, an additive manufacturing process offers the flexibility to perform partial and complete processing. There is a notable shift in the industry towards substituting SLM-processed aluminum alloy components with heavier materials. This transition is motivated by these materials' superior mechanical properties and increased durability for functional applications.

Figure 26. Aluminum alloy-based SLM-processed components for a wide range of applications (photos provided by JR SLM services from China).

Notably, even components used in everyday applications can now be swiftly manufactured within an hour using SLM. This contrasts with the time-consuming processes associated with traditional machining methods.

Instead, titanium alloys offer a wealth of exploration opportunities across various applications. These titanium alloys satisfy many mechanical and metallurgical requirements, making them a pivotal presence in automotive, aerospace, and structural applications. Particularly noteworthy is their prominent role in the biomedical field, where they find extensive use in implanting medical devices within the human body. Figure 27 provides a visual representation of complete human body parts crafted using the SLM process and successfully integrated into the human body. Many artificial body parts developed by various industries are now available, and their demand has surged significantly in just a few years following the inception of this technology [91].

Biomedical applications have greatly benefited from using titanium-based alloy powder in additive manufacturing. Components fabricated from titanium alloys using SLM exhibit exceptional mechanical and metallurgical properties. When assessing the advantages of components produced through additive manufacturing, several vital benefits come to the forefront, including enhanced corrosion resistance, adequate fatigue strength, reduced modulus, and lightweight attributes—essential considerations for biomedical applications. Nonetheless, there are certain drawbacks to acknowledge. These include lower wear resistance, which could pose concerns when components come into contact with body

fluids, necessitating supportive coatings. From an application perspective, Ti alloys are well-suited for external body part restoration and support adjustments. For example, they are utilized in bone fracture replacements, fixtures, screws, plates, caps, and, most recently, in developing hip and knee replacements. It is worth noting that Ti-based alloy components processed by SLM exhibit comparable mechanical properties when comparing skeletal (cortical) and skeletal (cancellous) applications. Due to elevated temperatures, SLM-processed titanium alloys are typically classified as (α + β) types. In particular, (α + β) Ti6Al4V materials are characterized by the presence of acicular martensite phases. The mechanical properties inherent to these (α + β) titanium grades are more than adequate to meet the requirements of bio-metallic components. Research in bio-metallic materials highlights that Ti67Nb alloys, a subset of the Ti–(α + β) category, demonstrate minimal impact on corrosion phenomena within bodily fluids. They showcase a notable increase in corrosion resistance during operational periods. Moreover, multiple sources in the literature propose that acicular martensitic phases in these alloys enhance their mechanical properties.

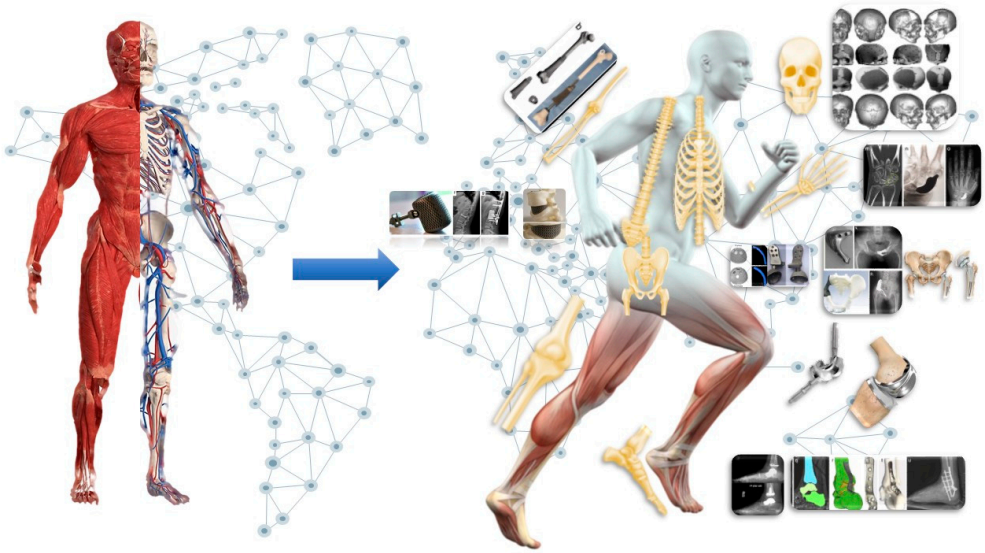

Figure 27. Human body parts made by Ti alloys from the SLM process Reprinted from Ref. [91].

Furthermore, other research indicates that β–Ti alloys hold appeal for biomedical applications. This arises from their remarkably similar elastic modulus, which measures around 49 GPa, closely matching the elastic modulus of cortical bone at approximately 25 GPa. This reduced elastic modulus in β–Ti alloys contrasts with that of conventional Ti6Al4V implants and can consequently mitigate stress-concentration effects, a critical factor in the design and performance of biomedical implants.

Very often, synovial joints, which are highly mobile and found in human fingers, can become a source of immense discomfort in cases of accidents, chronic diseases, or severe fractures involving multiple parts. These conditions can lead to excruciating pain and sometimes carry a recovery probability as low as 60%. In such critical cases, the solution often lies in replacing these synovial joints with artificial metallic counterparts made from titanium alloys. These titanium-based implants offer the added advantage of possessing anti-inflammatory and allergy-resistant properties, ensuring a smoother and more comfortable recovery. This approach significantly reduces the disability percentage in hands or specific joints, allowing individuals to regain mobility and overall quality of life.

Similarly, shoulder, knee, and hip joints, among the most versatile and frequently used moving parts of the human body, can occasionally experience issues, albeit in a relatively small percentage of cases (2–3 people out of 1000). These issues may arise from various causes, including accidents and medical conditions. In such instances, medical bio-metallic implants play a crucial role in improving the lives of those affected. These causes, such as bone cancer affecting a specific area, genetic disorders, or functional limitations, are often

severe. Introducing bio-metallic titanium-based alloys can bring about remarkable transformations in individuals facing these challenges, enabling them to lead more comfortable and functional lives in the years ahead.

Furthermore, the utilization of bio-metallic implants is particularly promising, especially among older individuals who often face challenges related to bodily function and joint health. Issues related to knee joints are prevalent in this demographic. A noteworthy case study in 2006 involved an Italian woman aged 74 or older. She encountered significant difficulties while walking, making it impossible to carry out her daily activities due to excruciating knee joint pain and impaired mobility. Following the recommendation of a medical professional, she decided to undergo a knee joint transplant, opting for a titanium-based powdered metallic knee implant.

Following a successful surgical procedure, her life underwent a remarkable transformation. She regained the ability to walk independently, free from needing assistance, and even engaged in physical exercises involving her legs. Presently, she enjoys a fit and healthy lifestyle. The transformative nature of this complete transplantation is vividly depicted in Figure 28.

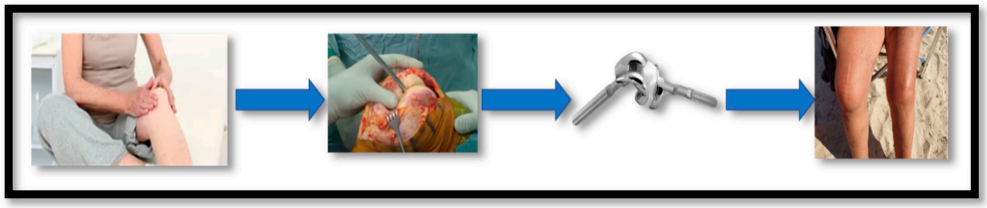

Figure 28. Before and after the knee replacement with a titanium-based alloy knee implant.

Steel offers a practical alternative to titanium, primarily due to its cost-efficiency. In many cases, steel alloys can readily substitute for titanium alloys in various applications, providing comparable performance while being more budget-friendly. Among the ferrous alloys, martensitic precipitation-hardened (PH) 17–4 stainless steel (SS) alloys have garnered significant attention due to their ability to bridge the gap between desired mechanical and metallurgical properties. The 17–4 SS alloys offer a range of advantageous features, including exceptional weldability, corrosion resistance at temperatures of up to approximately 300 °C, resilience to radiation, non-toxicity, oxidation resistance, stable surface finishes, and excellent durability in both open and closed environments. Figure 29 showcases various metallic components crafted from 17–4PH alloys, with and without hot isostatic pressing (HIP). The surface properties of these components are notably impressive. This hybrid scanning strategy has been meticulously developed and fine-tuned to optimize the production of superior, lightweight steel alloy components.

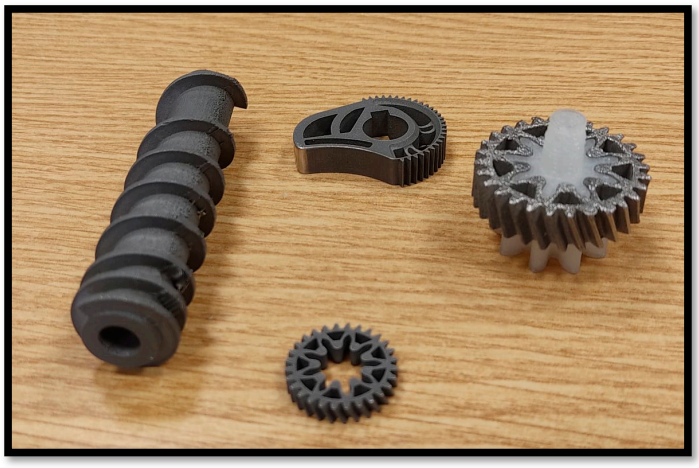

Figure 29. Represents a prepared specimen made from 17–4PH alloys.

6. Future Prospects

The scope and applications of the SLM process are continually expanding without inherent limitations. Every day, new applications and possibilities are being integrated. Recent advancements in additive manufacturing have significantly broadened its horizons, encompassing numerous industries and applications and facilitating the seamless production of metallic 3D-printed parts. The potential areas for further exploration include:

1. Three-dimensional printing of hybrid metallic materials for multiple applications such as aviation parts, spacecraft, microelectronics, chips, sensors, biological applications, and many more.
2. Environmental and sustainability experimental and simulation-based investigations are widely used for saving costs and improving the durability of products.
3. The improved exposure performance presently opens the door to a more profound and intuitive investigation of additional hybrid materials.

Anticipated advancements in SLM technology, including enhancements in laser systems and precise powder bed temperature control, are poised to drive greater utilization of SLM-processed alloys across various industrial applications. These developments herald a bright future for integrating SLM-produced alloys in industrial settings [96].

The aerospace industry is one area where SLM-processed alloys are expected to have a significant impact. SLM-processed alloys have the potential to be used in the manufacturing of aircraft structures, such as wing spars and fuselage panels, due to their high strength and lightweight properties. Additionally, SLM-processed alloys can produce complex geometries and customized parts in a single build, reducing the need for multiple parts and assembly operations.

In the automotive industry, SLM-processed alloys can manufacture lightweight and high-strength parts such as gears, engine components, and suspension parts. Also, using SLM-processed alloys in biomedical applications, such as dental and surgical implants, can be an exciting prospect.

In addition to these areas, SLM-processed alloys are also expected to find use in producing industrial parts, tools, and machinery, where their unique properties and capabilities can provide significant advantages over conventionally produced alloys.

In summary, SLM technology has the potential to revolutionize the manufacturing industry by making it possible to produce complex, highly customized parts in a single build. Aluminum, steel, and titanium alloys have already shown potential in SLM, and as the technology continues to advance, we will likely see an increase in the use of SLM-processed alloys across a wide range of industrial applications.

7. Conclusions

This review article covers the main areas required to understand in depth the SLM process, from the manufacturing stage to the resulting properties of the parts. The role of the process parameters on the mechanical/microstructural features and corrosion properties have been analyzed for aluminum, titanium, and iron alloys extensively used in SLM. The advancements for improving the quality of the parts and the role of the mathematical models have also been considered.

The main conclusions of the study are summarized in the following:

- In the SLM process, high-power lasers and meticulous management of critical parameters, including the laser's focal point, scanning speed, and powder bed temperature, allow to improve the quality of the parts. Enhancements involve, for example, laser systems and powder bed temperature control. Defects such as voids and roughness continue to occur in the SLM parts, indicating the necessity for continued research.
- Mathematical modeling can make a strong contribution to improving the quality of the parts by predicting how the process parameters affect the final product's microstructure, properties, and defects.

- Metallurgical and mechanical properties of aluminum, steel, and titanium SLM-processed have been found to have slightly lower strength and toughness due to the presence of defects. The corrosion behavior of SLM-processed materials is generally more similar to that of conventionally produced materials of the same alloy. In any case, the specific behavior depends on the alloy processing and the post-processing treatments.

In summary, SLM technology has the potential to revolutionize the manufacturing industry by making it possible to produce complex, highly customized parts in a single build. Further exploration and refinement of the process parameters and post-processing treatments are still essential to bridge the gap and align the properties of alloys produced via SLM with those of conventionally manufactured ones.

Author Contributions: Conceptualization, N.S., P.L. and G.R.; methodology, N.S., P.L. and G.R., software, N.S., P.L. and G.R.; validation, N.S., P.L. and G.R. formal analysis, N.S., P.L. and G.R.; investigation, N.S., P.L. and G.R. ; resources, N.S., P.L. and G.R.; data curation, N.S., P.L. and G.R.; writing—original draft preparation, N.S., P.L. and G.R.; writing—review and editing, N.S., P.L. and G.R.; visualization, N.S., P.L. and G.R.; supervision, P.L; project administration, P.L. All authors have read and agreed to the published version of the manuscript.

Funding: This research received no external funding.

Conflicts of Interest: The authors declare no conflict of interest.

References

1. Manfredi, D.; Calignano, F.; Ambrosio, E.P.; Krishnan, M.; Canali, R.; Biamino, S.; Pavese, M.; Atzeni, E.; Fino, P.; Badini, C. Direct Metal Laser Sintering: An additive manufacturing technology ready to produce lightweight structural parts for robotic applications. *La Metall. Ital.* **2013**. Available online: https://www.fracturae.com/index.php/aim/article/view/1210 (accessed on 28 July 2024).
2. Fiocchi, J.; Biffi, C.A.; Scaccabarozzi, D.; Saggin, B.; Tuissi, A. Enhancement of the Damping Behavior of Ti6Al4V Alloy through the Use of Trabecular Structure Produced by Selective Laser Melting. *Adv. Eng. Mater.* **2020**, *22*, 1900722. [CrossRef]
3. Tshephe, T.S.; Akinwamide, S.O.; Olevsky, E.; Olubambi, P.A. Additive manufacturing of titanium-based alloys—A review of methods, properties, challenges, and prospects. *Heliyon* **2022**, *8*, e09041. [CrossRef] [PubMed]
4. Lefebvre, L.-P.; Banhart, J.; Dunand, C. Porous Metals and Metallic Foams: Current Status and Recent Developments. *Adv. Eng. Mater.* **2008**, *10*, 9. [CrossRef]
5. Takata, N.; Kodaira, H.; Sekizawa, K.; Suzuki, A.; Kobashi, M. Change in microstructure of selectively laser melted AlSi10Mg alloy with heat treatments. *Mater. Sci. Eng.* **2017**, *704*, 218–228. [CrossRef]
6. Aboulkhair, N.T.; Simonelli, M.; Parry, L.; Ashcroft, I.; Tuck, C.; Hague, R. 3D printing of Aluminium alloys: Additive Manufacturing of Aluminium alloys using selective laser melting. *Prog. Mater. Sci.* **2019**, *106*, 100578. [CrossRef]
7. Singla, A.K.; Banerjee, M.; Sharma, A.; Singh, J.; Bansal, A.; Gupta, M.K.; Khanna, N.; Shahi, A.S.; Goyal, D.K. Selective laser melting of Ti6Al4V alloy: Process parameters, defects and post-treatments. *J. Manuf. Process.* **2021**, *64*, 161–187. [CrossRef]
8. Zhou, C.; Sun, Q.; Qian, D.; Liu, J.; Sun, J.; Sun, Z. Effect of deep cryogenic treatment on mechanical properties and residual stress of AlSi10Mg alloy fabricated by laser powder bed fusion. *J. Mater. Process. Technol.* **2022**, *303*, 117543. [CrossRef]
9. Li, Z.; Xu, R.; Zhang, Z.; Kucukkoc, I. The influence of scan length on fabricating thin-walled components in selective laser melting. *Int. J. Mach. Tools Manuf.* **2018**, *126*, 1–12. [CrossRef]
10. Tucho, W.M.; Lysne, V.H.; Austbø, H.; Sjolyst-Kverneland, A.; Hansen, V. Investigation of effects of process parameters on microstructure and hardness of SLM manufactured SS316L. *J. Alloys Compd.* **2018**, *740*, 910–925. [CrossRef]
11. Xing, X.; Duan, X.; Jiang, T.; Wang, J.; Jiang, F. Ultrasonic Peening Treatment Used to Improve Stress Corrosion Resistance of AlSi10Mg Components Fabricated Using Selective Laser Melting. *Metals* **2019**, *9*, 103. [CrossRef]
12. Ziółkowski, M.; Dyl, T. Possible Applications of Additive Manufacturing Technologies in Shipbuilding: A Review. *Machines* **2020**, *8*, 84. [CrossRef]
13. Yan, K.; Lin, Z.; Chen, M.; Wang, Y.; Wang, J.; Jiang, H. Fabrication of MnCuNiFe–CuAlNiFeMn Gradient Alloy by Laser Engineering Net Shaping System. *Materials* **2022**, *15*, 2336. [CrossRef]
14. Ilčík, J.; Koutný, D.; Paloušek, D. Geometrical Accuracy of the Metal Parts Produced by Selective Laser Melting: Initial Tests. In *Modern Methods of Construction Design. Lecture Notes in Mechanical Engineering*; Ševčik, L., Lepšík, P., Petrů, M., Mašín, I., Martonka, R., Eds.; Springer: Cham, Switzerland, 2014. [CrossRef]
15. Duan, X.; Chen, X.; Zhu, K.; Long, T.; Huang, S.; Jerry, F.Y.H. The Thermo-Mechanical Coupling Effect in Selective Laser Melting of Aluminum Alloy Powder. *Materials* **2021**, *14*, 1673. [CrossRef]
16. Stern, F.; Kleinhorst, J.; Tenkamp, J.; Walther, F. Investigation of the anisotropic cyclic damage behavior of selective laser melted AISI 316 L stainless steel. *Fatigue Fract. Eng. Mater. Struct.* **2019**, *42*, 2422–2430. [CrossRef]

17. Yan, J.-J.; Chen, M.-T.; Quach, W.-M.; Yan, M.; Young, B. Mechanical properties and cross-sectional behavior of additively manufactured high strength steel tubular sections. *Thin-Walled Struct.* **2019**, *144*, 106158. [CrossRef]
18. Ni, J.; Ling, H.; Zhang, S.; Wang, Z.; Peng, Z.; Benyshek, C.; Zan, R.; Miri, A.K.; Li, Z.; Zhang, X.; et al. Three-dimensional printing of metals for biomedical applications. *Mater. Today Bio* **2019**, *3*, 100024. [CrossRef]
19. Jardini, A.L.; Larosa, M.A.; Macedo, M.F.; Bernardes, L.F.; Lambert, C.S.; Zavaglia, C.A.C.; Filho, R.M.; Calderoni, D.R.; Ghizoni, E.; Kharmandayan, P. Improvement in Cranioplasty: Advanced Prosthesis Biomanufacturing. *Procedia CIRP* **2016**, *49*, 203–208. [CrossRef]
20. Ibrahim, M.Z.; Sarhan, A.A.; Yusuf, F.; Hamdi, M. Biomedical materials and techniques to improve the tribological, mechanical and biomedical properties of orthopedic implants—A review article. *J. Alloys Compd.* **2017**, *714*, 636–667. [CrossRef]
21. Tischler, M.; Patch, C.; Bidra, A.S. Rehabilitation of edentulous jaws with zirconia complete-arch fixed implant-supported prostheses: An up to 4-year retrospective clinical study. *J. Prosthet. Dent.* **2018**, *120*, 204–209. [CrossRef]
22. Saikko, V.; Ahlroos, T.; Revitzer, H.; Ryti, O.; Kuosmanen, P. The effect of acetabular cup position on wear of a large-diameter metal-on-metal prosthesis studied with a hip joint simulator. *Tribol. Int.* **2013**, *60*, 70–76. [CrossRef]
23. Hedlundh, U.; Karlsson, L. Combining a hip arthroplasty stem with trochanteric reattachment bolt and a polyaxial locking plate in the treatment of a periprosthetic fracture below a well-integrated implant. *Arthroplast. Today* **2016**, *2*, 141–145. [CrossRef] [PubMed]
24. Haan, J.; Asseln, M.; Zivcec, M.; Eschweiler, J.; Radermacher, R.; Broeckmann, C. Effect of subsequent Hot Isostatic Pressing on mechanical properties of ASTM F75 alloy produced by Selective Laser Melting. *Powder Met.* **2015**, *58*, 161–165. [CrossRef]
25. Song, C.; Yang, Y.; Wang, Y.; Yu, J.-K.; Wang, D. Personalized femoral component design and its direct manufacturing by selective laser melting. *Rapid Prototyp. J.* **2016**, *22*, 330–337. [CrossRef]
26. Wang, J.; Zhu, R.; Liu, Y.; Zhang, L. Understanding melt pool characteristics in laser powder bed fusion: An overview of single- and multi-track melt pools for process optimization. *Adv. Powder Mater.* **2023**, *2*, 100137. [CrossRef]
27. Ma, H.; Wang, J.; Qin, P.; Liu, Y.; Chen, L.; Wang, L.; Zhang, L. Advances in additively manufactured titanium alloys by powder bed fusion and directed energy deposition: Microstructure, defects, and mechanical behavior. *J. Mater. Sci. Technol.* **2024**, *183*, 32–62. [CrossRef]
28. Cui, Y.-W.; Wang, L.; Zhang, L.-C. Towards load-bearing biomedical titanium-based alloys: From essential requirements to future developments. *Prog. Mater. Sci.* **2024**, *144*, 101277. [CrossRef]
29. Ramirez-Cedillo, E.; Sandoval-Robles, J.A.; Ruiz-Huerta, L.; Caballero-Ruiz, A.; Rodriguez, C.A.; Siller, H.R. Process planning guidelines in selective laser melting for the manufacturing of stainless steel parts. *Procedia Manuf.* **2018**, *26*, 973–982. [CrossRef]
30. Bartolo, P.; Kruth, J.-P.; Silva, J.; Levy, G.; Malshe, A.; Rajurkar, K.; Mitsuishi, M.; Ciurana, J.; Leu, M. Biomedical production of implants by additive electro-chemical and physical processes. *CIRP Ann.* **2012**, *61*, 635–655. [CrossRef]
31. Faludi, J.; Baumers, M.; Maskery, I.; Hague, R. Environmental Impacts of Selective Laser Melting: Do Printer, Powder, Or Power Dominate? *J. Ind. Ecol.* **2016**, *21*, s44–s56. [CrossRef]
32. Yap, C.Y.; Chua, C.K.; Dong, Z.L.; Liu, Z.H.; Zhang, D.Q.; Loh, L.E.; Sing, S.L. Review of selective laser melting: Materials and applications. *Appl. Phys. Rev.* **2015**, *2*, 041101. [CrossRef]
33. Nespoli, A.; Bettini, P.; Villa, E.; Sala, G.; Passaretti, F.; Grande, A.M. A Study on Damping Property of NiTi Elements Produced by Selective Laser-Beam Melting. *Adv. Eng. Mater.* **2021**, *23*, 2001246. [CrossRef]
34. Liang, K.; Zhang, Q.; Cao, Y.; Tang, L. Design and performance analysis of a flexible unit based on selective laser melting. *Adv. Mech. Eng.* **2022**, *14*. [CrossRef]
35. Ullsperger, T.; Matthäus, G.; Kaden, L.; Engelhardt, H.; Rettenmayr, M.; Risse, S.; Tünnermann, A.; Nolte, S. Selective laser melting of hypereutectic Al-Si40-powder using ultra-short laser pulses. *Appl. Phys. A* **2017**, *123*, 798. [CrossRef]
36. Ding, H.; Tang, Q.; Zhu, Y.; Zhang, C.; Yang, H. Cavitation erosion resistance of 316 L stainless steel fabricated using selective laser melting. *Friction* **2020**, *9*, 1580–1598. [CrossRef]
37. Laleh, M.; Hughes, A.E.; Xu, W.; Gibson, I.; Tan, M.Y. Unexpected erosion-corrosion behaviour of 316 L stainless steel produced by selective laser melting. *Corros. Sci.* **2019**, *155*, 67–74. [CrossRef]
38. Bae, J.H.; Yu, J.M.; Dao, V.H.; Lok, V.; Yoon, K.B. Effects of processing parameters on creep behavior of 316 L stainless steel produced using selective laser melting. *J. Mech. Sci. Technol.* **2021**, *35*, 3803–3812. [CrossRef]
39. Wang, L.; Wang, Y.; Zhou, Z.; Wan, H.; Li, C.; Chen, G.; Zhang, G. Small punch creep performance of heterogeneous microstructure dominated Inconel 718 fabricated by selective laser melting. *Mater. Des.* **2020**, *195*, 109042. [CrossRef]
40. Wang, L.; Zhou, Z.; Li, C.; Chen, G.; Zhang, G. Comparative investigation of small punch creep resistance of Inconel 718 fabricated by selective laser melting. *Mater. Sci. Eng. A* **2019**, *745*, 31–38. [CrossRef]
41. Wu, Z.; Liu, Y.; Wu, X.; Liu, X.; Wang, J.; Wang, Q. Fatigue performance of beta titanium alloy topological porous structures fabricated by laser powder bed fusion. *J. Mater. Res. Technol.* **2024**, *29*, 4772–4780. [CrossRef]
42. Wu, Z.-Y.; Liu, Y.-J.; Bai, H.-W.; Wu, X.; Gao, Y.-H.; Liu, X.-C.; Wang, J.-C.; Wang, Q. Microstructure and mechanical behavior of rhombic dodecahedron-structured porous β-Ti composites fabricated via laser powder bed fusion. *J. Mater. Res. Technol.* **2024**, *31*, 298–310. [CrossRef]
43. Qu, F.; Hao, S.; Wang, D.; Guo, Y.; Shen, B.; Li, H. Research on Selective Laser Sintering Process of Limestone/Polyethersulfone Composites. *J. Mater. Eng. Perform.* **2022**, *31*, 9411–9424. [CrossRef]

44. Baek, M.-S.; Kreethi, R.; Park, T.-H.; Sohn, Y.; Lee, K.-A. Influence of heat treatment on the high-cycle fatigue properties and fatigue damage mechanism of selective laser melted AlSi10Mg alloy. *Mater. Sci. Eng. A* **2021**, *819*, 14148. [CrossRef]
45. Colombo, C.; Biffi, C.A.; Fiocchi, J.; Scaccabarozzi, D.; Saggin, B.; Tuissi, A.; Vergani, L.M. Modulating the damping capacity of SLMed AlSi10Mg trough stress-relieving thermal treatments. *Theor. Appl. Fract. Mech.* **2020**, *107*, 102537. [CrossRef]
46. Bartsch, K.; Herzog, D.; Bossen, B.; Emmelmann, C. Material modeling of Ti–6Al–4V alloy processed by laser powder bed fusion for application in macro-scale process simulation. *Mater. Sci. Eng. A* **2021**, *814*, 141237. [CrossRef]
47. Lu, J.; Zhuo, L. Additive manufacturing of titanium alloys via selective laser melting: Fabrication, microstructure, post-processing, performance and prospect. *Int. J. Refract. Met. Hard Mater.* **2023**, *111*, 106110. [CrossRef]
48. Sing, S.L.; Wiria, F.E.; Yeong, W.Y. Selective laser melting of lattice structures: A statistical approach to manufacturability and mechanical behavior. *Robot. Comput. Manuf.* **2018**, *49*, 170–180. [CrossRef]
49. Karaoglu, S.Y.; Karaoglu, S.; Unal, I. Aerospace Industry and Aluminum Metal Matrix Composites. *Int. J. Aviat. Sci. Technol.* **2021**, *2*, 73–81. [CrossRef]
50. Casalino, G.; Campanelli, S.L.; Contuzzi, N.; Ludovico, A.D. Experimental investigation and statistical optimisation of the selective laser melting process of a maraging steel. *Opt. Laser Technol.* **2015**, *65*, 151–158. [CrossRef]
51. Casati, R.; Lemke, J.N.; Tuissi, A.; Vedani, M. Aging Behaviour and Mechanical Performance of 18-Ni 300 Steel Processed by Selective Laser Melting. *Metals* **2016**, *6*, 218. [CrossRef]
52. Giurgiutiu, V. Chapter 1—Introduction. In *Structural Health Monitoring of Aerospace Composites*; Giurgiutiu, V., Ed.; Academic Press: Cambridge, MA, USA, 2016; pp. 1–23. [CrossRef]
53. Madikizela, C.; Cornish, L.; Chown, L.; Möller, H. Microstructure and mechanical properties of selective laser melted Ti-3Al-8V-6Cr-4Zr-4Mo compared to Ti-6Al-4V. *Mater. Sci. Eng. A* **2019**, *747*, 225–231. [CrossRef]
54. Ran, J.; Sun, X.; Wei, S.; Chen, Z.; Zhao, H. Achieving Ti-5Al-4Sn-2Zr-1Mo-0.25Si-1Nb Alloys with High Strength and Moderate Ductility through Selective Laser Melting. *Materials* **2020**, *13*, 5527. [CrossRef] [PubMed]
55. Jiang, J.; Ren, Z.; Ma, Z.; Zhang, T.; Zhang, P.; Zhang, D.Z.; Mao, Z. Mechanical properties and microstructural evolution of TA15 Ti alloy processed by selective laser melting before and after annealing. *Mater. Sci. Eng. A* **2020**, *772*, 138742. [CrossRef]
56. Das, S.; Wohlert, M.; Beaman, J.J.; Bourell, D.L. Producing Metal Parts with Selective Laser Sintering/Hot Isostatic Pressing. *JOM* **1998**, *50*, 17–20. [CrossRef]
57. Lu, H.; Wang, Z.; Cai, J.; Xu, X.; Luo, K.; Wu, L.; Lu, J. Effects of laser shock peening on the hot corrosion behaviour of the selective laser melted Ti6Al4V titanium alloy. *Corros. Sci.* **2021**, *188*, 109558. [CrossRef]
58. Gunasekaran, J.; Sevvel, P.; Solomon, I.J. Metallic materials fabrication by selective laser melting: A review. *Mater. Today Proc.* **2021**, *37*, 252–256. [CrossRef]
59. Palmeri, D.; Buffa, G.; Pollara, G.; Fratini, L. Sample building orientation effect on porosity and mechanical properties in Selective Laser Melting of Ti6Al4V titanium alloy. *Mater. Sci. Eng. A* **2022**, *830*, 142306. [CrossRef]
60. Calignano, F.; Cattano, G.; Iuliano, L.; Manfredi, D. Controlled Porosity Structures in Aluminum and Titanium Alloys by Selective Laser Melting. In *Industrializing Additive Manufacturing—Proceedings of Additive Manufacturing in Products and Applications—AMPA2017*; Meboldt, M., Klahn, C., Eds.; Springer: Cham, Switzerland, 2018. [CrossRef]
61. Jafari, D.; Wits, W.W. The utilization of selective laser melting technology on heat transfer devices for thermal energy conversion applications: A review. *Renew. Sustain. Energy Rev.* **2018**, *91*, 420–442. [CrossRef]
62. Romei, F.; Grubišić, A.N.; Gibbon, D. Manufacturing of a high-temperature resistojet heat exchanger by selective laser melting. *Acta Astronaut.* **2017**, *138*, 356–368. [CrossRef]
63. Schwab, H.; Palm, F.; Kühn, U.; Eckert, J. Microstructure and mechanical properties of the near-beta titanium alloy Ti-5553 processed by selective laser melting. *Mater. Des.* **2016**, *105*, 75–80. [CrossRef]
64. Zhang, L.; Attar, H. Selective Laser Melting of Titanium Alloys and Titanium Matrix Composites for Biomedical Applications: A Review. *Adv. Eng. Mater.* **2016**, *18*, 463–475. [CrossRef]
65. Cai, C.; Wu, X.; Liu, W.; Zhu, W.; Chen, H.; Qiu, J.C.D.; Sun, C.-N.; Liu, J.; Wei, Q.; Shi, Y. Selective laser melting of near-α titanium alloy Ti-6Al-2Zr-1Mo-1V: Parameter optimization, heat treatment and mechanical performance. *J. Mater. Sci. Technol.* **2020**, *57*, 51–64. [CrossRef]
66. Malý, M.; Höller, C.; Skalon, M.; Meier, B.; Koutný, D.; Pichler, R.; Sommitsch, C.; Paloušek, D. Effect of Process Parameters and High-Temperature Preheating on Residual Stress and Relative Density of Ti6Al4V Processed by Selective Laser Melting. *Materials* **2019**, *12*, 930. [CrossRef] [PubMed]
67. Awd, M.; Stern, F.; Kampmann, A.; Kotzem, D.; Tenkamp, J.; Walther, F. Microstructural Characterization of the Anisotropy and Cyclic Deformation Behavior of Selective Laser Melted AlSi10Mg Structures. *Metals* **2018**, *8*, 825. [CrossRef]
68. Rakesh, C.S.; Raja, A.; Nadig, P.; Jayaganthan, R.; Vasa, N.J. Influence of working environment and built orientation on the tensile properties of selective laser melted AlSi10Mg alloy. *Mater. Sci. Eng. A* **2019**, *750*, 141–151. [CrossRef]
69. Snopiński, P.; Woźniak, A.; Łukowiec, D.; Matus, K.; Tański, T.; Rusz, S.; Hilšer, O. Evolution of Microstructure, Texture and Corrosion Properties of Additively Manufactured AlSi10Mg Alloy Subjected to Equal Channel Angular Pressing (ECAP). *Symmetry* **2022**, *14*, 674. [CrossRef]
70. Wang, L.-Z.; Wang, S.; Hong, X. Pulsed SLM-manufactured AlSi10Mg alloy: Mechanical properties and microstructural effects of designed laser energy densities. *J. Manuf. Process.* **2018**, *35*, 492–499. [CrossRef]

71. Teixeira, J.E.; Tavares-Lehmann, A.T.C. Industry 4.0 in the European union: Policies and national strategies. *Technol. Forecast. Soc. Change* **2022**, *180*, 121664. [CrossRef]
72. Ghobakhloo, M.; Iranmanesh, M.; Grybauskas, A.; Vilkas, M.; Petraitė, M. Industry 4.0, innovation, and sustainable development: A systematic review and a roadmap to sustainable innovation. *Bus. Strat. Environ.* **2021**, *30*, 4237–4257. [CrossRef]
73. Shipp, S.S.; Gupta, N.; Lal, B.; Scott, J.A.; Weber, C.L.; Finnin, M.S.; Blake, M.; Newsome, S.; Thomas, S. Emerging Global Trends in Advanced Manufacturing; ADA558616; Institute for Defense Analyses Alexandria Va; 1 March 2012. Available online: https://apps.dtic.mil/sti/pdfs/ADA558616.pdf (accessed on 2 August 2022).
74. Liu, Z.; Liu, J.; Osmani, M. Integration of Digital Economy and Circular Economy: Current Status and Future Directions. *Sustainability* **2021**, *13*, 7217. [CrossRef]
75. Vafadar, A.; Guzzomi, F.; Rassau, A.; Hayward, K. Advances in Metal Additive Manufacturing: A Review of Common Processes, Industrial Applications, and Current Challenges. *Appl. Sci.* **2021**, *11*, 1213. [CrossRef]
76. Thomas, D.S.; Gilbert, S.W. Costs and Cost Effectiveness of Additive Manufacturing. *NIST Speical Publ.* **2014**, *1176*. [CrossRef]
77. Kapitonov, I.A.; Voloshin, V.I.; Zhukovskaya, I.V.; Shulus, A.A. Small and Medium-Sized Enterprises as a Driver of Innovative Development of the Russian Fuel and Energy Complex. *Int. J. Energy Econ. Policy* **2017**, *7*, 231–239.
78. De Negri, J.F.; Pezzutto, S.; Gantioler, S.; Moser, D.; Sparber, W. A Comprehensive Analysis of Public and Private Funding for Photovoltaics Research and Development in the European Union, Norway, and Turkey. *Energies* **2020**, *13*, 2743. [CrossRef]
79. Delic, M.; Eyers, D.R. The effect of additive manufacturing adoption on supply chain flexibility and performance: An empirical analysis from the automotive industry. *Int. J. Prod. Econ.* **2020**, *228*, 107689. [CrossRef]
80. Zhong, R.Y.; Xu, X.; Klotz, E.; Newman, S.T. Intelligent Manufacturing in the Context of Industry 4.0: A Review. *Engineering* **2017**, *3*, 616–630. [CrossRef]
81. Büchi, G.; Cugno, M.; Castagnoli, R. Smart factory performance and Industry 4.0. *Technol. Forecast. Soc. Change* **2020**, *150*, 119790. [CrossRef]
82. Ingarao, G. Manufacturing strategies for efficiency in energy and resources use: The role of metal shaping processes. *J. Clean. Prod.* **2017**, *142*, 2872–2886. [CrossRef]
83. Ren, L.; Zhou, S.; Peng, T.; Ou, X. A review of CO_2 emissions reduction technologies and low-carbon development in the iron and steel industry focusing on China. *Renew. Sustain. Energy Rev.* **2021**, *143*, 110846. [CrossRef]
84. Sun, Y.; Bi, K.; Yin, S. Measuring and Integrating Risk Management into Green Innovation Practices for Green Manufacturing under the Global Value Chain. *Sustainability* **2020**, *12*, 545. [CrossRef]
85. Müller, J.M.; Voigt, K.-I. Sustainable Industrial Value Creation in SMEs: A Comparison between Industry 4.0 and Made in China 2025. *Int. J. Precis. Eng. Manuf. Technol.* **2018**, *5*, 659–670. [CrossRef]
86. Rissman, J.; Bataille, C.; Masanet, E.; Aden, N.; Morrow, W.R.; Zhou, N.; Elliott, N.; Dell, R.; Heeren, N.; Huckestein, B.; et al. Technologies and policies to decarbonize global industry: Review and assessment of mitigation drivers through 2070. *Appl. Energy* **2020**, *266*, 114848. [CrossRef]
87. Jabbour, C.J.C.; Neto, A.S.; Gobbo, J.A.; Ribeiro, M.d.S.; Jabbour, A.B.L.d.S. Eco-innovations in more sustainable supply chains for a low-carbon economy: A multiple case study of human critical success factors in Brazilian leading companies. *Int. J. Prod. Econ.* **2015**, *164*, 245–257. [CrossRef]
88. Haleem, A.; Javaid, M.; Singh, R.P.; Suman, R. Significant roles of 4D printing using smart materials in the field of manufacturing. *Adv. Ind. Eng. Polym. Res.* **2021**, *4*, 301–311. [CrossRef]
89. Kafle, A.; Luis, E.; Silwal, R.; Pan, H.M.; Shrestha, P.L.; Bastola, A.K. 3D/4D Printing of Polymers: Fused Deposition Modelling (FDM), Selective Laser Sintering (SLS), and Stereolithography (SLA). *Polymers* **2021**, *13*, 3101. [CrossRef]
90. Mitchell, A.; Lafont, U.; Hołyńska, M.; Semprimoschnig, C. Additive manufacturing—A review of 4D printing and future applications. *Addit. Manuf.* **2018**, *24*, 606–626. [CrossRef]
91. Palmquist, A.; Jolic, M.; Hryha, E.; Shah, F.A. Complex geometry and integrated macro-porosity: Clinical applications of electron beam melting to fabricate bespoke bone-anchored implants. *Acta Biomater.* **2023**, *156*, 125–145. [CrossRef]
92. Aversa, A.; Marchese, G.; Saboori, A.; Bassini, E.; Manfredi, D.; Biamino, S.; Ugues, D.; Fino, P.; Lombardi, M. New Aluminum Alloys Specifically Designed for Laser Powder Bed Fusion: A Review. *Materials* **2019**, *12*, 1007. [CrossRef] [PubMed]
93. Wang, Z.; Ummethala, R.; Singh, N.; Tang, S.; Suryanarayana, C.; Eckert, J.; Prashanth, K.G. Selective Laser Melting of Aluminum and Its Alloys. *Materials* **2020**, *13*, 4564. [CrossRef]
94. Li, R.; Shi, Y.; Wang, Z.; Wang, L.; Liu, J.; Jiang, W. Densification behavior of gas and water atomized 316 L stainless steel powder during selective laser melting. *Appl. Surf. Sci.* **2010**, *256*, 4350–4356. [CrossRef]
95. Strano, G.; Hao, L.; Everson, R.M.; Evans, K.E. Surface roughness analysis, modelling and prediction in selective laser melting. *J. Mech. Work. Technol.* **2013**, *213*, 589–597. [CrossRef]
96. Fayazfar, H.; Salarian, M.; Rogalsky, A.; Sarker, D.; Russo, P.; Paserin, V.; Toyserkani, E. A critical review of powder-based additive manufacturing of ferrous alloys: Process parameters, microstructure and mechanical properties. *Mater. Des.* **2018**, *144*, 98–128. [CrossRef]
97. Chen, W.; Chen, C.; Zi, X.; Cheng, X.; Zhang, X.; Lin, Y.C.; Zhou, K. Controlling the microstructure and mechanical properties of a metastable β titanium alloy by selective laser melting. *Mater. Sci. Eng. A* **2018**, *726*, 240–250. [CrossRef]
98. Zhang, L.-C.; Liu, Y.; Li, S.; Hao, Y. Additive Manufacturing of Titanium Alloys by Electron Beam Melting: A Review. *Adv. Eng. Mater.* **2018**, *20*, 1700842. [CrossRef]

99. Travyanov, A.Y.; Petrovsky, P.V.; Cheverikin, V.V.; Lagutin, A.O.; Khomutov, M.G.; Luk'yanov, V.V. Microstructure and Mechanical Properties of Titanium Alloy VT6 and VT20L Diffusion Joints. *Metallurgist* **2022**, *65*, 1133–1141. [CrossRef]
100. Vrancken, B.; Thijs, L.; Kruth, J.-P.; Van Humbeeck, J. Heat treatment of Ti6Al4V produced by Selective Laser Melting: Microstructure and mechanical properties. *J. Alloys Compd.* **2012**, *541*, 177–185. [CrossRef]
101. Fousová, M.; Vojtěch, D.; Kubásek, J.; Jablonská, E.; Fojt, J. Promising characteristics of gradient porosity Ti-6Al-4V alloy prepared by SLM process. *J. Mech. Behav. Biomed. Mater.* **2017**, *69*, 368–376. [CrossRef]
102. Yang, Y.; Li, L.; Pan, Y.; Sun, Z. Energy Consumption Modeling of Stereolithography-Based Additive Manufacturing Toward Environmental Sustainability. *J. Ind. Ecol.* **2017**, *21*, S168–S178. [CrossRef]
103. Huang, J.; Qin, Q.; Wang, J. A Review of Stereolithography: Processes and Systems. *Process.* **2020**, *8*, 1138. [CrossRef]
104. Baumers, M.; Tuck, C.; Wildman, R.; Ashcroft, I.; Hague, R. Shape Complexity and Process Energy Consumption in Electron Beam Melting: A Case of Something for Nothing in Additive Manufacturing? *J. Ind. Ecol.* **2017**, *21*, S157–S167. [CrossRef]
105. Uçak, N.; Çiçek, A.; Aslantas, K. Machinability of 3D printed metallic materials fabricated by selective laser melting and electron beam melting: A review. *J. Manuf. Process.* **2022**, *80*, 414–457. [CrossRef]
106. Ameen, W.; Mohammed, M.K.; Al-Ahmari, A.; Ahmed, N.; Dabwan, A.; Kaid, H. Optimization of perforated support structures for electron beam additive manufacturing. *Int. J. Adv. Manuf. Technol.* **2022**, *120*, 7305–7323. [CrossRef]
107. Pradhan, S.R.; Singh, R.; Banwait, S.S. On 3D printing of dental crowns with direct metal laser sintering for canine. *J. Mech. Sci. Technol.* **2022**, *36*, 4197–4203. [CrossRef]
108. Rontescu, C.; Amza, C.-G.; Bogatu, A.-M.; Cicic, D.-T.; Anania, F.D.; Burlacu, A. Reconditioning by Welding of Prosthesis Obtained through Additive Manufacturing. *Metals* **2022**, *12*, 1177. [CrossRef]
109. Dwivedi, S.; Dixit, A.R.; Das, A.K. Wetting behavior of selective laser melted (SLM) bio-medical grade stainless steel 316 L. *Mater. Today Proc.* **2022**, *56*, 46–50. [CrossRef]
110. Razaviye, M.K.; Tafti, R.A.; Khajehmohammadi, M. An investigation on mechanical properties of PA12 parts produced by a SLS 3D printer: An experimental approach. *CIRP J. Manuf. Sci. Technol.* **2022**, *38*, 760–768. [CrossRef]
111. Thakar, C.M.; Parkhe, S.S.; Jain, A.; Phasinam, K.; Murugesan, G.; Ventayen, R.J.M. 3d Printing: Basic principles and applications. *Mater. Today Proc.* **2022**, *51*, 842–849. [CrossRef]
112. Salifu, S.; Desai, D.; Ogunbiyi, O.; Mwale, K. Recent development in the additive manufacturing of polymer-based composites for automotive structures—A review. *Int. J. Adv. Manuf. Technol.* **2022**, *119*, 6877–6891. [CrossRef]
113. Baechle-Clayton, M.; Loos, E.; Taheri, M.; Taheri, H. Failures and Flaws in Fused Deposition Modeling (FDM) Additively Manufactured Polymers and Composites. *J. Compos. Sci.* **2022**, *6*, 202. [CrossRef]
114. Warke, S.; Puranik, V. Comparison of energy consumption of ABS and PLA while 3 D printing with fused deposition modeling process. *Mater. Today Proc.* **2022**, *66*, 2098–2103. [CrossRef]
115. Onuh, S.O.; Yusuf, Y.Y. Rapid prototyping technology: Applications and benefits for rapid product development. *J. Intell. Manuf.* **1999**, *10*, 301–311. [CrossRef]
116. Campbell, I.; Bourell, D.; Gibson, I. Additive manufacturing: Rapid prototyping comes of age. *Rapid Prototyp. J.* **2012**, *18*, 255–258. [CrossRef]
117. Kumar, M.B.; Sathiya, P. Methods and materials for additive manufacturing: A critical review on advancements and challenges. *Thin-Walled Struct.* **2021**, *159*, 107228. [CrossRef]
118. Deckard, C.R. Method and Apparatus for Producing Parts by Selective Sintering. U.S. Patent 4863538-A, 5 September 1989. Available online: https://patents.google.com/patent/US4863538A/en (accessed on 8 August 2022).
119. Beaman, J.J.; Deckard, C.R. 1990-07-03 Board of Regents, The University of Texas; System Selective Laser Sintering with Assisted Powder Handling. U.S. Patent 4938816A, 17 October 1986. Available online: https://patents.google.com/patent/US4938816A/en (accessed on 8 August 2022).
120. Grossin, D.; Montón, A.; Navarrete-Segado, P.; Özmen, E.; Urruth, G.; Maury, F.; Maury, D.; Frances, C.; Tourbin, M.; Lenormand, P.; et al. A review of additive manufacturing of ceramics by powder bed selective laser processing (sintering/melting): Calcium phosphate, silicon carbide, zirconia, alumina, and their composites. *Open Ceram.* **2021**, *5*, 100073. [CrossRef]
121. Gross, B.C.; Erkal, J.L.; Lockwood, S.Y.; Chen, C.; Spence, D.M. Evaluation of 3D Printing and Its Potential Impact on Biotechnology and the Chemical Sciences. *Anal. Chem.* **2014**, *86*, 3240–3253. [CrossRef]
122. Jemghili, R.; Taleb, A.A.; Mansouri, K. Additive Manufacturing Progress as a New Industrial Revolution. In Proceedings of the 2020 IEEE 2nd International Conference on Electronics, Control, Optimization and Computer Science (ICECOCS), Kenitra, Morocco, 2–3 December 2020; pp. 1–8.
123. Fu, J.; Li, H.; Song, X.; Fu, M. Multi-scale defects in powder-based additively manufactured metals and alloys. *J. Mater. Sci. Technol.* **2022**, *122*, 165–199. [CrossRef]
124. Teng, F.; Sun, Y.; Guo, S.; Gao, B.; Yu, G. Topological and Mechanical Properties of Different Lattice Structures Based on Additive Manufacturing. *Micromachines* **2022**, *13*, 1017. [CrossRef]
125. Ahmadi, M.; Tabary, S.B.; Rahmatabadi, D.; Ebrahimi, M.; Abrinia, K.; Hashemi, R. Review of selective laser melting of magnesium alloys: Advantages, microstructure and mechanical characterizations, defects, challenges, and applications. *J. Mater. Res. Technol.* **2022**, *19*, 1537–1562. [CrossRef]

126. Abd-Elaziem, W.; Elkatatny, S.; Abd-Elaziem, A.-E.; Khedr, M.; El-Baky, M.A.A.; Hassan, M.A.; Abu-Okail, M.; Mohammed, M.; Järvenpää, A.; Allam, T.; et al. On the current research progress of metallic materials fabricated by laser powder bed fusion process: A review. *J. Mater. Res. Technol.* **2022**, *20*, 681–707. [CrossRef]
127. Fang, Y.; Kim, M.-K.; Zhang, Y.; Duan, Z.; Yuan, Q.; Suhr, J. Particulate-reinforced iron-based metal matrix composites fabricated by selective laser melting: A systematic review. *J. Manuf. Process.* **2022**, *74*, 592–639. [CrossRef]
128. Rezaeifar, H.; Elbestawi, M. Porosity formation mitigation in laser powder bed fusion process using a control approach. *Opt. Laser Technol.* **2022**, *147*, 107611. [CrossRef]
129. Chekotu, J.C.; Goodall, R.; Kinahan, D.; Brabazon, D. Control of Ni-Ti phase structure, solid-state transformation temperatures and enthalpies via control of L-PBF process parameters. *Mater. Des.* **2022**, *218*, 110715. [CrossRef]
130. Marques, A.; Cunha, Â.; Silva, M.R.; Osendi, M.I.; Silva, F.S.; Bartolomeu, C.F. Inconel 718 produced by laser powder bed fusion: An overview of the influence of processing parameters on microstructural and mechanical properties. *Int. J. Adv. Manuf. Technol.* **2022**, *121*, 5651–5675. [CrossRef]
131. Wang, S.; Tao, S.; Peng, H. Influence of Powder Characteristics on the Microstructure and Mechanical Behaviour of GH4099 Superalloy Fabricated by Electron Beam Melting. *Metals* **2022**, *12*, 1301. [CrossRef]
132. Przekora, A.; Kazimierczak, P.; Wojcik, M.; Chodorski, E.; Kropiwnicki, J. Mesh Ti6Al4V Material Manufactured by Selective Laser Melting (SLM) as a Promising Intervertebral Fusion Cage. *Int. J. Mol. Sci.* **2022**, *23*, 3985. [CrossRef]
133. Ryabykh, S.; Silant'Eva, T.; Dyuryagina, O.; D'Iachkov, K.; Stogov, M.; Antonov, N.; Tushina, N.; Reznik, A. Development of porous titanium implants for interbody fusion. *Genij Ortop.* **2021**, *27*, 773–781. [CrossRef]
134. Wang, H.; Wan, Y.; Li, Q.; Liu, X.; Yu, M.; Zhang, X.; Xia, Y.; Sun, Q.; Liu, Z. Multiscale design and biomechanical evaluation of porous spinal fusion cage to realize specified mechanical properties. *Bio-Des. Manuf.* **2022**, *5*, 277–293. [CrossRef]
135. Davies, R.; Cascarini, L. The temporo-mandibular joint: Reconstruction of the condyle post-ablation. *J. Oral Biol. Craniofac. Res.* **2022**, *12*, 593–598. [CrossRef]
136. Huang, X.; Liu, H.; Wang, Z.; Qiao, L.; Su, Y.; Yan, Y. Effect of surface oxidation on wear and tribocorrosion behavior of forged and selective laser melting-based TC4 alloys. *Tribol. Int.* **2022**, *174*, 107780. [CrossRef]
137. Miranda, G.; Faria, S.; Bartolomeu, F.; Pinto, E.; Alves, N.; Silva, F.S. The Influence of Laser Power and Scan Speed on the Dimensional Accuracy of Ti6Al4V Thin-Walled Parts Manufactured by Selective Laser Melting. *Metals* **2022**, *12*, 1226. [CrossRef]
138. Aufa, A.; Hassan, M.Z.; Ismail, Z. Recent advances in Ti-6Al-4V additively manufactured by selective laser melting for biomedical implants: Prospect development. *J. Alloys Compd.* **2022**, *896*, 163072. [CrossRef]
139. Păcurar, R.; Berce, P.; Petrilak, A.; Nemeş, O.; Borzan, C.M.; Harničárová, M.; Păcurar, A. Selective Laser Sintering of PA 2200 for Hip Implant Applications: Finite Element Analysis, Process Optimization, Morphological and Mechanical Characterization. *Materials* **2021**, *14*, 4240. [CrossRef]
140. Okazaki, Y.; Mori, J. Mechanical Performance of Artificial Hip Stems Manufactured by Hot Forging and Selective Laser Melting Using Biocompatible Ti-15Zr-4Nb Alloy. *Materials* **2021**, *14*, 732. [CrossRef]
141. Ghosh, S.; Abanteriba, S.; Wong, S.; Houshyar, S. Selective laser melted titanium alloys for hip implant applications: Surface modification with new method of polymer grafting. *J. Mech. Behav. Biomed. Mater.* **2018**, *87*, 312–324. [CrossRef] [PubMed]
142. A Lykov, P.; Baitimerov, R.M.; Panfilov, A.V.; O Guz, A. The manufacturing of TiAl6V4 implants using selective laser melting technology. *IOP Conf. Series Mater. Sci. Eng.* **2017**, *248*, 012004. [CrossRef]
143. Rotaru, H.; Schumacher, R.; Kim, S.-G.; Dinu, C. Selective laser melted titanium implants: A new technique for the reconstruction of extensive zygomatic complex defects. *Maxillofac. Plast. Reconstr. Surg.* **2015**, *37*, 1–6. [CrossRef]
144. Murr, L.; Amato, K.; Li, S.; Tian, Y.; Cheng, X.; Gaytan, S.; Martinez, E.; Shindo, P.; Medina, F.; Wicker, R. Microstructure and mechanical properties of open-cellular biomaterials prototypes for total knee replacement implants fabricated by electron beam melting. *J. Mech. Behav. Biomed. Mater.* **2011**, *4*, 1396–1411. [CrossRef]
145. Fischer, D.; Cheng, K.-Y.; Neto, M.Q.; Hall, D.; Bijukumar, D.; Orías, A.A.E.; Pourzal, R.; van Arkel, R.J.; Mathew, M.T. Corrosion Behavior of Selective Laser Melting (SLM) Manufactured Ti6Al4V Alloy in Saline and BCS Solution. *J. Bio- Tribo-Corros.* **2022**, *8*, 63. [CrossRef]
146. Wang, N.; Meenashisundaram, G.K.; Kandilya, D.; Fuh, J.Y.H.; Dheen, S.T.; Kumar, A.S. A biomechanical evaluation on Cubic, Octet, and TPMS gyroid Ti6Al4V lattice structures fabricated by selective laser melting and the effects of their debris on human osteoblast-like cells. *Mater. Sci. Eng. C* **2022**, *137*, 212829. [CrossRef]
147. Bartolomeu, F.; Gasik, M.; Silva, F.S.; Miranda, G. Mechanical Properties of Ti6Al4V Fabricated by Laser Powder Bed Fusion: A Review Focused on the Processing and Microstructural Parameters Influence on the Final Properties. *Metals* **2022**, *12*, 986. [CrossRef]
148. Harun, W.S.W.; Kadirgama, K.; Samykano, M.; Ramasamy, D.; Ahmad, I.; Moradi, M. Mechanical behavior of selective laser melting-produced metallic biomaterials. In *Wood-Head Publishing Series in Biomaterials, Mechanical Behaviour of Biomaterials*; Davim, J.P., Ed.; Woodhead Publishing: Sawston, UK, 2019; pp. 101–116, ISBN 9780081021743. [CrossRef]
149. Alabdullah, S.A.; Hannam, A.G.; Wyatt, C.C.; McCullagh, A.P.; Aleksejuniene, J.; Mostafa, N.Z. Comparison of digital and conventional methods of fit evaluation of partial removable dental prosthesis frameworks fabricated by selective laser melting. *J. Prosthet. Dent.* **2022**, *127*, 478.e1–478.e10. [CrossRef] [PubMed]

150. D'ercole, S.; Mangano, C.; Cellini, L.; Di Lodovico, S.; Ozkaya, C.A.; Iezzi, G.; Piattelli, A.; Petrini, M. A Novel 3D Titanium Surface Produced by Selective Laser Sintering to Counteract *Streptococcus oralis* Biofilm Formation. *Appl. Sci.* **2021**, *11*, 11915. [CrossRef]
151. Yu, X.; Xu, R.; Zhang, Z.; Jiang, Q.; Liu, Y.; Yu, X.; Deng, F. Different Cell and Tissue Behavior of Micro-/Nano-Tubes and Micro-/Nano-Nets Topographies on Selective Laser Melting Titanium to Enhance Osseointegration. *Int. J. Nanomed.* **2021**, *16*, 3329–3342. [CrossRef] [PubMed] [PubMed Central]
152. Kuryło, P.; Cykowska-Błasik, M.; Tertel, E.; Pałka, Ł.; Pruszyński, P.; Klekiel, T. Novel Development of Implant Elements Manufactured through Selective Laser Melting 3D Printing. *Adv. Eng. Mater.* **2021**, *23*, 2001488. [CrossRef]
153. Manea, A.; Bran, S.; Baciut, M.; Armencea, G.; Pop, D.; Berce, P.; Vodnar, D.-C.; Hedesiu, M.; Dinu, C.; Petrutiu, A.; et al. Sterilization protocol for porous dental implants made by Selective Laser Melting. *Med. Pharm. Rep.* **2018**, *91*, 452–457. [CrossRef] [PubMed] [PubMed Central]
154. Li, L.; Chen, Y.; Lu, Y.; Qin, S.; Huang, G.; Huang, T.; Lin, J. Effect of heat treatment on the corrosion resistance of selective laser melted Ti6Al4V3Cu alloy. *J. Mater. Res. Technol.* **2021**, *12*, 904–915. [CrossRef]
155. Ho, C.M.B.; Ng, S.H.; Yoon, Y.-J. A review on 3D printed bioimplants. *Int. J. Precis. Eng. Manuf.* **2015**, *16*, 1035–1046. [CrossRef]
156. Sergi, A.; Khan, R.H.; Attallah, M.M. The role of powder atomisation route on the microstructure and mechanical properties of hot isostatically pressed Inconel 625. *Mater. Sci. Eng. A* **2021**, *808*, 140950. [CrossRef]
157. Thermal and Thermomechanical Structuring Processes. In *Microstructuring of Glasses. Springer Series in Materials Science*; Springer: Berlin/Heidelberg, Germany, 2008. [CrossRef]
158. Gaget, L. 3D Printing in the Medical Industry: The 3D Printed Knee Replacement. Sculpteo. Available online: https://www.sculpteo.com/blog/2018/05/04/3d-printing-in-the-medical-industry-the-3d-printed-knee-replacement/ (accessed on 3 August 2022).
159. Moniri, S.; Xiao, X.; Shahani, A.J. The mechanism of eutectic modification by trace impurities. *Sci. Rep.* **2019**, *9*, 3381. [CrossRef]
160. Taylor, J.A. Iron-Containing Intermetallic Phases in Al-Si Based Casting Alloys. *Procedia Mater. Sci.* **2012**, *1*, 19–33. [CrossRef]
161. Yadav, P. Drift Detection in L-PBF Process Using In-Situ Monitoring Instrumentation and Data Analytic Techniques. Doctoral Dissertation, Université de Bordeaux, 2022. Available online: https://theses.hal.science/tel-03741173 (accessed on 28 July 2024).
162. Gong, J.; Wei, K.; Liu, M.; Song, W.; Li, X.; Zeng, X. Microstructure and mechanical properties of AlSi10Mg alloy built by laser powder bed fusion/direct energy deposition hybrid laser additive manufacturing. *Addit. Manuf.* **2022**, *59*, 103160. [CrossRef]
163. Olakanmi, E.O.T.; Cochrane, R.F.; Dalgarno, K.W. A review on selective laser sintering/melting (SLS/SLM) of aluminium alloy powders: Processing, microstructure, and properties. *Prog. Mater. Sci.* **2015**, *74*, 401–477. [CrossRef]
164. Dey, A.; Yodo, N. A Systematic Survey of FDM Process Parameter Optimization and Their Influence on Part Characteristics. *J. Manuf. Mater. Process.* **2019**, *3*, 64. [CrossRef]
165. Kokareva, V.V.; Smelov, V.G.; Agapovichev, A.V.; Sotov, A.V.; Sufiiarov, V.S. Development of SLM quality system for gas turbines engines parts production. *IOP Conf. Series Mater. Sci. Eng.* **2018**, *441*, 012024. [CrossRef]
166. Wang, G.; Huang, L.; Liu, Z.; Qin, Z.; He, W.; Liu, F.; Chen, C.; Nie, Y. Process optimization and mechanical properties of oxide dispersion strengthened nickel-based superalloy by selective laser melting. *Mater. Des.* **2020**, *188*, 108418. [CrossRef]
167. Fish, S.; Booth, J.C.; Kubiak, S.T.; Wroe, W.W.; Bryant, A.D.; Moser, D.R.; Beaman, J.J. Design and subsystem development of a high temperature selective laser sintering machine for enhanced process monitoring and control. *Addit. Manuf.* **2015**, *5*, 60–67. [CrossRef]
168. Lu, X.; Chiumenti, M.; Cervera, M.; Slimani, M.; Gonzalez, I. Recoater-Induced Distortions and Build Failures in Selective Laser Melting of Thin-Walled Ti6Al4V Parts. *J. Manuf. Mater. Process.* **2023**, *7*, 64. [CrossRef]
169. Kleemeyer, S.D. Determining the Influence of the Type of Shielding Gas during Additive Manufacturing of an Aluminum Alloy by Monitoring the Process Qualitatively and Analyzing Process Byproducts Quantitatively. *Dissertation*. 2021. Available online: http://www.diva-portal.org/smash/record.jsf?pid=diva2:1611847&dswid=3152 (accessed on 9 September 2022).
170. He, J.; Lv, J.; Song, Z.; Wang, C.; Feng, H.; Wu, X.; Zhu, Y.; Zheng, W. Maintaining Excellent Mechanical Properties via Additive Manufacturing of Low-N 25Cr-Type Duplex Stainless Steel. *Materials* **2023**, *16*, 7125. [CrossRef]
171. Gargalis, L.; Karavias, L.; Graff, J.S.; Diplas, S.; Koumoulos, E.P.; Karaxi, E.K. A Comparative Investigation of Duplex and Super Duplex Stainless Steels Processed through Laser Powder Bed Fusion. *Metals* **2023**, *13*, 1897. [CrossRef]
172. Opprecht, M.; Garandet, J.-P.; Roux, G.; Flament, C.; Soulier, M. A solution to the hot cracking problem for aluminium alloys manufactured by laser beam melting. *Acta Mater.* **2020**, *197*, 40–53. [CrossRef]
173. Waqar, S.; Guo, K.; Sun, J. Evolution of residual stress behavior in selective laser melting (SLM) of 316 L stainless steel through preheating and in-situ re-scanning techniques. *Opt. Laser Technol.* **2022**, *149*, 107806. [CrossRef]
174. Fang, Z.-C.; Wu, Z.-L.; Huang, C.-G.; Wu, C.-W. Review on residual stress in selective laser melting additive manufacturing of alloy parts. *Opt. Laser Technol.* **2020**, *129*, 106283. [CrossRef]
175. *ISO/ASTM DIS 52900:2021*; Additive Manufacturing—General Principles—Terminology. International Organization for Standardization: Geneva, Switzerland, 2021. Available online: https://www.iso.org/standard/74514.html (accessed on 9 September 2022).
176. Delgado, J.; Ciurana, J.; Rodríguez, C.A. Influence of process parameters on part quality and mechanical properties for DMLS and SLM with iron-based materials. *Int. J. Adv. Manuf. Technol.* **2012**, *60*, 601–610. [CrossRef]
177. Kaufmann, N.; Imran, M.; Wischeropp, T.M.; Emmelmann, C.; Siddique, S.; Walther, F. Influence of Process Parameters on the Quality of Aluminium Alloy EN AW 7075 Using Selective Laser Melting (SLM). *Phys. Procedia* **2016**, *83*, 918–926. [CrossRef]

178. Karthik, G.M.; Kim, H.S. Heterogeneous Aspects of Additive Manufactured Metallic Parts: A Review. *Met. Mater. Int.* **2021**, *27*, 1–39. [CrossRef]
179. Cooke, S.; Ahmadi, K.; Willerth, S.; Herring, R. Metal additive manufacturing: Technology, metallurgy and modelling. *J. Manuf. Process.* **2020**, *57*, 978–1003. [CrossRef]
180. Zhang, B.; Dembinski, L.; Coddet, C. The study of the laser parameters and environment variables effect on mechanical properties of high compact parts elaborated by selective laser melting 316 L powder. *Mater. Sci. Eng. A* **2013**, *584*, 21–31. [CrossRef]
181. Liverani, E.; Toschi, S.; Ceschini, L.; Fortunato, A. Effect of selective laser melting (SLM) process parameters on microstructure and mechanical properties of 316 L austenitic stainless steel. *J. Mech. Work. Technol.* **2017**, *249*, 255–263. [CrossRef]
182. Tang, X.; Zhang, S.; Zhang, C.; Chen, J.; Zhang, J.; Liu, Y. Optimization of laser energy density and scanning strategy on the forming quality of 24CrNiMo low alloy steel manufactured by SLM. *Mater. Charact.* **2020**, *170*, 110718. [CrossRef]
183. Donik, Č.; Kraner, J.; Paulin, I.; Godec, M. Influence of the Energy Density for Selective Laser Melting on the Microstructure and Mechanical Properties of Stainless Steel. *Metals* **2020**, *10*, 919. [CrossRef]
184. Zhang, P.; Tan, J.; Tian, Y.; Yan, H.; Yu, Z. Research progress on selective laser melting (SLM) of bulk metallic glasses (BMGs): A review. *Int. J. Adv. Manuf. Technol.* **2022**, *118*, 2017–2057. [CrossRef]
185. Gupta, A.; Lloyd, D.; Court, S. Precipitation hardening in Al–Mg–Si alloys with and without excess Si. *Mater. Sci. Eng. A* **2001**, *316*, 11–17. [CrossRef]
186. Zhen, L.; Kang, S.B.; Kim, H.W. Effect of natural aging and preaging on subsequent precipitation process of an AI-Mg-Si alloy with high excess silicon. *Mater. Sci. Technol.* **1997**, *13*, 905–911. [CrossRef]
187. Wang, Y.; Li, R.; Yuan, T.; Zou, L.; Wang, M.; Yang, H. Microstructure and mechanical properties of Al-Fe-Sc-Zr alloy additively manufactured by selective laser melting. *Mater. Charact.* **2021**, *180*, 111397. [CrossRef]
188. Ansari, P.; Salamci, M.U. On the selective laser melting based additive manufacturing of AlSi10Mg: The process parameter investigation through multiphysics simulation and experimental validation. *J. Alloys Compd.* **2022**, *890*, 161873. [CrossRef]
189. Zhang, D.; Yi, D.; Wu, X.; Liu, Z.; Wang, W.; Poprawe, R.; Schleifenbaumc, J.H.; Zieglerd, S. SiC reinforced AlSi10Mg composites fabricated by selective laser melting. *J. Alloys Compd.* **2022**, *894*, 162365. [CrossRef]
190. Dong, Z.; Xu, M.; Guo, H.; Fei, X.; Liu, Y.; Gong, B.; Ju, G. Microstructural evolution and characterization of AlSi10Mg alloy manufactured by selective laser melting. *J. Mater. Res. Technol.* **2022**, *17*, 2343–2354. [CrossRef]
191. Cheng, W.; Liu, Y.; Xiao, X.; Huang, B.; Zhou, Z.; Liu, X. Microstructure and mechanical properties of a novel (TiB_2+TiC)/AlSi10Mg composite prepared by selective laser melting. *Mater. Sci. Eng. A* **2022**, *834*, 142435. [CrossRef]
192. Kuai, Z.; Li, Z.; Liu, B.; Liu, W.; Yang, S. Effects of remelting on the surface morphology, microstructure and mechanical properties of AlSi10Mg alloy fabricated by selective laser melting. *Mater. Chem. Phys.* **2022**, *285*, 125901. [CrossRef]
193. Hu, Z.; Zhao, Z.; Deng, X.; Lu, Z.; Liu, J.; Qu, Z. Microstructure and mechanical behavior of TiCN reinforced AlSi10Mg composite fabricated by selective laser melting. *Mater. Chem. Phys.* **2022**, *283*, 125996. [CrossRef]
194. Xiao, Y.; Chen, H.; Bian, Z.; Sun, T.; Ding, H.; Yang, Q.; Wu, Y.; Lian, Q.; Chen, Z.; Wang, H. Enhancing strength and ductility of AlSi10Mg fabricated by selective laser melting by TiB2 nanoparticles. *J. Mater. Sci. Technol.* **2022**, *109*, 254–266. [CrossRef]
195. Pan, W.; Ye, Z.; Zhang, Y.; Liu, Y.; Liang, B.; Zhai, Z. Research on Microstructure and Properties of AlSi10Mg Fabricated by Selective Laser Melting. *Materials* **2022**, *15*, 2528. [CrossRef] [PubMed]
196. Xiaohui, J.; Chunbo, Y.; Honglan, G.; Shan, G.; Yong, Z. Effect of supporting structure design on residual stresses in selective laser melting of AlSi10Mg. *Int. J. Adv. Manuf. Technol.* **2022**, *118*, 1597–1608. [CrossRef]
197. Mei, J.; Han, Y.; Zu, G.; Zhu, W.; Zhao, Y.; Chen, H.; Ran, X. Achieving Superior Strength and Ductility of AlSi10Mg Alloy Fabricated by Selective Laser Melting with Large Laser Power and High Scanning Speed. *Acta Met. Sin. (Engl. Lett.)* **2022**, *35*, 1665–1672. [CrossRef]
198. Meyer, G.; Musekamp, J.; Göbel, F.; Gardian, F.; Mittelstedt, C. Manufacturability investigation of inclined AlSi10Mg lattice struts by means of selective laser melting. *Manuf. Lett.* **2021**, *31*, 101–105. [CrossRef]
199. Zhang, Y.; Li, X.; Yuan, S.; Sun, R.; Sakai, T.; Lashari, M.I.; Hamid, U.; Li, W. High-cycle-fatigue properties of selective-laser-melted AlSi10Mg with multiple building directions. *Int. J. Mech. Sci.* **2022**, *224*, 107336. [CrossRef]
200. Cai, X.; Pan, C.; Wang, J.; Zhang, W.; Fan, Z.; Gao, Y.; Xu, P.; Sun, H.; Li, J.; Yang, W. Mechanical behavior, damage mode and mechanism of AlSi10Mg porous structure manufactured by selective laser melting. *J. Alloys Compd.* **2022**, *897*, 162933. [CrossRef]
201. Liverani, E.; Li, Y.; Ascari, A.; Zhao, X.; Fortunato, A. The effect of femto-second laser shock peening on the microstructures and surface roughness of AlSi10Mg samples produced with selective laser melting (SLM). *Procedia CIRP* **2022**, *108*, 77–81. [CrossRef]
202. Cui, L.; Peng, Z.; Chang, Y.; He, D.; Cao, Q.; Guo, X.; Zeng, Y. Porosity, microstructure and mechanical property of welded joints produced by different laser welding processes in selective laser melting AlSi10Mg alloys. *Opt. Laser Technol.* **2022**, *150*, 107952. [CrossRef]
203. Giganto, S.; Martínez-Pellitero, S.; Barreiro, J.; Leo, P.; Castro-Sastre, M. Impact of the laser scanning strategy on the quality of 17-4PH stainless steel parts manufactured by selective laser melting. *J. Mater. Res. Technol.* **2022**, *20*, 2734–2747. [CrossRef]
204. Neikter, M.; Huang, A.; Wu, X. Microstructural characterization of binary microstructure pattern in selective laser-melted Ti-6Al-4V. *Int. J. Adv. Manuf. Technol.* **2019**, *104*, 1381–1391. [CrossRef]
205. Zhang, H.; Xu, M.; Kumar, P.; Li, C.; Dai, W.; Liu, Z.; Li, Z.; Zhang, Y. Enhancement of fatigue resistance of additively manufactured 304 L SS by unique heterogeneous microstructure. *Virtual Phys. Prototyp.* **2021**, *16*, 125–145. [CrossRef]

206. Aboulkhair, N.T.; Everitt, N.M.; Ashcroft, I.; Tuck, C. Reducing porosity in AlSi10Mg parts processed by selective laser melting. *Addit. Manuf.* **2014**, *1–4*, 77–86. [CrossRef]
207. Barile, C.; Casavola, C.; Kannan, V.P.; Renna, G. The influence of AlSi10Mg recycled powder on corrosion-resistance behaviour of additively manufactured components: Mechanical aspects and acoustic emission investigation. *Arch. Civ. Mech. Eng.* **2022**, *22*, 52. [CrossRef]
208. Revilla, R.I.; Verkens, D.; Rubben, T.; De Graeve, I. Corrosion and Corrosion Protection of Additively Manufactured Aluminium Alloys—A Critical Review. *Materials* **2020**, *13*, 4804. [CrossRef]
209. Guo, M.; Sun, M.; Huang, J.; Pang, S. A Comparative Study on the Microstructures and Mechanical Properties of Al-10Si-0.5Mg Alloys Prepared under Different Conditions. *Metals* **2022**, *12*, 142. [CrossRef]
210. Ahmed, N.; Barsoum, I.; Haidemenopoulos, G.; Abu Al-Rub, R. Process parameter selection and optimization of laser powder bed fusion for 316 L stainless steel: A review. *J. Manuf. Process.* **2022**, *75*, 415–434. [CrossRef]
211. Dong, S.; Zhang, X.; Ma, F.; Jiang, J.; Yang, W.; Lin, Z.; Chen, C. Research on metallurgical bonding of selective laser melted AlSi10Mg alloy. *Mater. Res. Express* **2020**, *7*, 025801. [CrossRef]
212. Bobel, A.; Hector, L.G.; Chelladurai, I.; Sachdev, A.K.; Brown, T.; Poling, W.A.; Kubic, R.; Gould, B.; Zhao, C.; Parab, N.; et al. In situ synchrotron X-ray imaging of 4140 steel laser powder bed fusion. *Materialia* **2019**, *6*, 100306. [CrossRef]
213. Michi, R.A.; Plotkowski, A.; Shyam, A.; Dehoff, R.R.; Babu, S.S. Towards high-temperature applications of aluminium alloys enabled by additive manufacturing. *Int. Mater. Rev.* **2021**, *67*, 298–345. [CrossRef]
214. Yang, X.; Cai, R.; Chen, C.; Araby, S.; Li, Y.; Wang, W.; Meng, Q. High-performance aluminum alloy with fully equiaxed grain microstructure fabricated by laser metal deposition. *J. Mater. Res.* **2022**, *37*, 3658–3667. [CrossRef]
215. Buchbinder, D.; Schleifenbaum, H.; Heidrich, S.; Meiners, W.; Bültmann, J. High Power Selective Laser Melting (HP SLM) of Aluminum Parts. *Phys. Procedia* **2011**, *12*, 271–278. [CrossRef]
216. Spierings, A.; Dawson, K.; Kern, K.; Palm, F.; Wegener, K. SLM-processed Sc- and Zr- modified Al-Mg alloy: Mechanical properties and microstructural effects of heat treatment. *Mater. Sci. Eng. A* **2017**, *701*, 264–273. [CrossRef]
217. Shamsaei, N.; Yadollahi, A.; Bian, L.; Thompson, S.M. An overview of Direct Laser Deposition for additive manufacturing; Part II: Mechanical behavior, process parameter optimization and control. *Addit. Manuf.* **2015**, *8*, 12–35. [CrossRef]
218. Wang, Y. Microstructure and Mechanical Properties of Laser Additively Manufactured Nickle based Alloy with External Nano Reinforcement: A Feasibility Study. Ph.D. Thesis, University of Cincinnati, Cincinnati, OH, USA, 2018. Available online: http://rave.ohiolink.edu/etdc/view?acc_num=ucin1535703630944044 (accessed on 29 July 2024).
219. Ou, Y.; Zhang, Q.; Wei, Y.; Hu, Y.; Sui, S.; Chen, J.; Wang, X.; Li, W. Evolution of Heterogeneous Microstructure and its Effects on Tensile Properties of Selective Laser Melted AlSi10Mg Alloy. *J. Mater. Eng. Perform.* **2021**, *30*, 4341–4355. [CrossRef]
220. Park, T.-H.; Baek, M.-S.; Hyer, H.; Sohn, Y.; Lee, K.-A. Effect of direct aging on the microstructure and tensile properties of AlSi10Mg alloy manufactured by selective laser melting process. *Mater. Charact.* **2021**, *176*, 111113. [CrossRef]
221. Girelli, L.; Tocci, M.; Gelfi, M.; Pola, A. Study of heat treatment parameters for additively manufactured AlSi10Mg in comparison with corresponding cast alloy. *Mater. Sci. Eng. A* **2018**, *739*, 317–328. [CrossRef]
222. Buchbinder, D.; Meiners, W.; Wissenbach, K.; Poprawe, R. Selective laser melting of aluminum die-cast alloy—Correlations between process parameters, solidification conditions, and resulting mechanical properties. *J. Laser Appl.* **2015**, *27*. [CrossRef]
223. Li, W.; Li, S.; Liu, J.; Zhang, A.; Zhou, Y.; Wei, Q.; Yan, C.; Shi, Y. Effect of heat treatment on AlSi10Mg alloy fabricated by selective laser melting: Microstructure evolution, mechanical properties and fracture mechanism. *Mater. Sci. Eng. A* **2016**, *663*, 116–125. [CrossRef]
224. Rosenthal, I.; Shneck, R.; Stern, A. Heat treatment effect on the mechanical properties and fracture mechanism in AlSi10Mg fabricated by additive manufacturing selective laser melting process. *Mater. Sci. Eng. A* **2018**, *729*, 310–322. [CrossRef]
225. Wang, L.; Jiang, X.; Guo, M.; Zhu, X.; Yan, B. Characterisation of structural properties for AlSi10Mg alloys fabricated by selective laser melting. *Mater. Sci. Technol.* **2017**, *33*, 2274–2282. [CrossRef]
226. Li, L.; Meng, X.; Huang, S.; Wang, H.; Li, P.; Zhou, J. Investigating the effect of the scanning speed on the characteristics of Al-Li alloy fabricated by selective laser melting. *J. Manuf. Process.* **2022**, *75*, 719–728. [CrossRef]
227. Mauduit, A.; Pillot, S.; Frascati, F. Application study of AlSi10Mg alloy by selective laser melting: Physical and mechanical properties, microstructure, heat treatments and manufacturing of aluminium metallic matrix composite (MMC). *Met. Res. Technol.* **2015**, *112*, 605. [CrossRef]
228. Ghio, E.; Cerri, E. Work Hardening of Heat-Treated AlSi10Mg Alloy Manufactured by Selective Laser Melting: Effects of Layer Thickness and Hatch Spacing. *Materials* **2021**, *14*, 4901. [CrossRef]
229. Kleiner, S.; Zürcher, J.; Bauer, O.; Margraf, P. Heat Treatment Response of Selectively Laser Melted AlSi10Mg. *HTM J. Heat Treat. Mater.* **2020**, *75*, 327–341. [CrossRef]
230. Zuback, J.; DebRoy, T. The Hardness of Additively Manufactured Alloys. *Materials* **2018**, *11*, 2070. [CrossRef] [PubMed]
231. Gu, X.-H.; Zhang, J.-X.; Fan, X.-L.; Zhang, L.-C. Corrosion Behavior of Selective Laser Melted AlSi10Mg Alloy in NaCl Solution and Its Dependence on Heat Treatment. *Acta Met. Sin. (Engl. Lett.)* **2020**, *33*, 327–337. [CrossRef]
232. Tiwari, A.; Singh, G.; Jayaganthan, R. Improved Corrosion Resistance Behaviour of AlSi10Mg Alloy due to Selective Laser Melting. *Coatings* **2023**, *13*, 225. [CrossRef]
233. Liu, S.; Shin, Y.C. Additive manufacturing of Ti6Al4V alloy: A review. *Mater. Des.* **2018**, *164*, 107552. [CrossRef]

234. Yan, M.; Yu, P. *An Overview of Densification, Microstructure and Mechanical Property of Additively Manufactured Ti-6Al-4V —Comparison among Selective Laser Melting, Electron Beam Melting, Laser Metal Deposition and Selective Laser Sintering, and with Conventional Powder; Sintering Techniques of Materials*; IntechOpen: London, UK, 2015; pp. 77–106. [CrossRef]
235. Pal, S.; Finšgar, M.; Bončina, T.; Lojen, G.; Brajlih, T.; Drstvenšek, I. Effect of surface powder particles and morphologies on corrosion of Ti-6Al-4 V fabricated with different energy densities in selective laser melting. *Mater. Des.* **2021**, *211*, 110184. [CrossRef]
236. Colombo-Pulgarín, J.C.; Biffi, C.A.; Vedani, M.; Celentano, D.; Sánchez-Egea, A.; Boccardo, A.D.; Ponthot, J.P. Beta Titanium Alloys Processed by Laser Powder Bed Fusion: A Review. *J. Mater. Eng. Perform.* **2021**, *30*, 6365–6388. [CrossRef]
237. Sutton, A.T.; Kriewall, C.S.; Leu, M.C.; Newkirk, J.W. Powders for Additive Manufacturing Process: Characterization Techniques and Effects on Part Properties. In Proceedings of the 2016 International Solid Freeform Fabrication Symposium, University of Texas, Austin, TX, USA, 8–10 August 2016; Available online: https://repositories.lib.utexas.edu/handle/2152/89651 (accessed on 28 July 2024).
238. Sun, Y.Y.; Gulizia, S.; Oh, C.H.; Doblin, C.; Yang, Y.F.; Qian, M. Manipulation and Characterization of a Novel Titanium Powder Precursor for Additive Manufacturing Applications. *JOM* **2015**, *67*, 564–572. [CrossRef]
239. Suresh, S.; Sun, C.-N.; Tekumalla, S.; Rosa, V.; Nai, S.M.L.; Wong, R.C.W. Mechanical properties and in vitro cytocompatibility of dense and porous Ti–6Al–4V ELI manufactured by selective laser melting technology for biomedical applications. *J. Mech. Behav. Biomed. Mater.* **2021**, *123*, 104712. [CrossRef]
240. Jin, P.; Tang, Q.; Li, K.; Feng, Q.; Ren, Z.; Song, J.; Nie, Y.; Ma, S. The relationship between the macro- and microstructure and the mechanical properties of selective-laser-melted Ti6Al4V samples under low energy inputs: Simulation and experiment. *Opt. Laser Technol.* **2022**, *148*, 7713. [CrossRef]
241. Wang, D.; Wang, H.; Chen, X.; Liu, Y.; Lu, D.; Liu, X.; Han, C. Densification, Tailored Microstructure, and Mechanical Properties of Selective Laser Melted Ti–6Al–4V Alloy via Annealing Heat Treatment. *Micromachines* **2022**, *13*, 331. [CrossRef] [PubMed]
242. Sun, Q.-D.; Sun, J.; Guo, K.; Waqar, S.; Liu, J.-W.; Wang, L.-S. Influences of processing parameters and heat treatment on microstructure and mechanical behavior of Ti-6Al-4V fabricated using selective laser melting. *Adv. Manuf.* **2022**, *10*, 520–540. [CrossRef]
243. Meng, L.; Yang, H.; Ben, D.; Ji, H.; Lian, D.; Ren, D.; Li, Y.; Bai, T.; Cai, Y.; Chen, J.; et al. Effects of defects and microstructures on tensile properties of selective laser melted Ti6Al4V alloys fabricated in the optimal process zone. *Mater. Sci. Eng. A* **2022**, *830*, 142294. [CrossRef]
244. Park, H.S.; Nguyen, D.S.; Le-Hong, T.; Van Tran, X. Machine learning-based optimization of process parameters in selective laser melting for biomedical applications. *J. Intell. Manuf.* **2022**, *33*, 1843–1858. [CrossRef]
245. Young, Z.A.; Coday, M.M.; Guo, Q.; Qu, M.; Hojjatzadeh, S.M.H.; Escano, L.I.; Fezzaa, K.; Sun, T.; Chen, L. Uncertainties Induced by Processing Parameter Variation in Selective Laser Melting of Ti6Al4V Revealed by In-Situ X-ray Imaging. *Materials* **2022**, *15*, 530. [CrossRef]
246. Lv, J.; Luo, K.; Lu, H.; Wang, Z.; Liu, J.; Lu, J. Achieving high strength and ductility in selective laser melting Ti-6Al-4V alloy by laser shock peening. *J. Alloys Compd.* **2022**, *899*, 163335. [CrossRef]
247. Xiang, S.; Yuan, Y.; Zhang, C.; Chen, J. Effects of Process Parameters on the Corrosion Resistance and Biocompatibility of Ti6Al4V Parts Fabricated by Selective Laser Melting. *ACS Omega* **2022**, *7*, 5954–5961. [CrossRef] [PubMed]
248. Traxel, K.D.; Bandyopadhyay, A. Selective laser melting of Ti6Al4V-B4C-BN in situ reactive composites. *J. Mater. Res. Technol.* **2022**, *18*, 2654–2671. [CrossRef]
249. Karimi, J.; Antonov, M.; Kollo, L.; Prashanth, K. Role of laser remelting and heat treatment in mechanical and tribological properties of selective laser melted Ti6Al4V alloy. *J. Alloys Compd.* **2022**, *897*, 163207. [CrossRef]
250. Zheng, Z.; Jin, X.; Bai, Y.; Yang, Y.; Ni, C.; Lu, W.F.; Wang, H. Microstructure and anisotropic mechanical properties of selective laser melted Ti6Al4V alloy under different scanning strategies. *Mater. Sci. Eng. A* **2022**, *831*, 142236. [CrossRef]
251. Yan, X.; Yue, S.; Ge, J.; Chen, C.; Lupoi, R.; Yin, S. Microstructural and mechanical optimization of selective laser melted Ti6Al4V lattices: Effect of hot isostatic pressing. *J. Manuf. Process.* **2022**, *77*, 151–162. [CrossRef]
252. Maitra, V.; Shi, J.; Lu, C. Robust prediction and validation of as-built density of Ti-6Al-4V parts manufactured via selective laser melting using a machine learning approach. *J. Manuf. Process.* **2022**, *78*, 183–201. [CrossRef]
253. Zhang, J.; Song, B.; Cai, C.; Zhang, L.; Shi, Y. Tailorable microstructure and mechanical properties of selective laser melted TiB/Ti–6Al–4V composite by heat treatment. *Adv. Powder Mater.* **2021**, *1*, 100010. [CrossRef]
254. Yang, X.; Li, Y.; Duan, M.-G.; Jiang, W.; Chen, D.; Li, B. An investigation of ductile fracture behavior of Ti6Al4V alloy fabricated by selective laser melting. *J. Alloys Compd.* **2022**, *890*, 161926. [CrossRef]
255. Wang, J.; Liu, Y.; Rabadia, C.D.; Liang, S.-X.; Sercombe, T.B.; Zhang, L.-C. Microstructural homogeneity and mechanical behavior of a selective laser melted Ti-35Nb alloy produced from an elemental powder mixture. *J. Mater. Sci. Technol.* **2021**, *61*, 221–233. [CrossRef]
256. Wang, J.; Liu, Y.; Liang, S.; Zhang, Y.; Wang, L.; Sercombe, T.; Zhang, L. Comparison of microstructure and mechanical behavior of Ti-35Nb manufactured by laser powder bed fusion from elemental powder mixture and prealloyed powder. *J. Mater. Sci. Technol.* **2021**, *105*, 1–16. [CrossRef]
257. Wei, K.; Wang, Z.; Zeng, X. Effect of heat treatment on microstructure and mechanical properties of the selective laser melting processed Ti-5Al-2.5Sn α titanium alloy. *Mater. Sci. Eng. A* **2018**, *709*, 301–311. [CrossRef]

258. Mohanavel, V.; Ravichandran, M.; Anandakrishnan, V.; Pramanik, A.; Meignanamoorthy, M.; Karthick, A.; Muhibbullah, M. Mechanical Properties of Titanium Diboride Particles Reinforced Aluminum Alloy Matrix Composites: A Comprehensive Review. *Adv. Mater. Sci. Eng.* **2021**, *2021*, 18. [CrossRef]
259. Wu, Q.; Wang, Z.; Zheng, T.; Chen, D.; Yang, Z.; Li, J.; Kai, J.-J.; Wang, J. A casting eutectic high entropy alloy with superior strength-ductility combination. *Mater. Lett.* **2019**, *253*, 268–271. [CrossRef]
260. Kenel, C.; Grolimund, D.; Li, X.; Panepucci, E.; Samson, V.A.; Sanchez, D.F.; Marone, F.; Leinenbach, C. In situ investigation of phase transformations in Ti-6Al-4V under additive manufacturing conditions combining laser melting and high-speed micro-X-ray diffraction. *Sci. Rep.* **2017**, *7*, 16358. [CrossRef] [PubMed]
261. Kanwar, S.; Al-Ketan, O.; Vijayavenkataraman, S. A novel method to design biomimetic, 3D printable stochastic scaffolds with controlled porosity for bone tissue engineering. *Mater. Des.* **2022**, *220*, 110857. [CrossRef]
262. Waqas, M.; He, D.; Liu, Y.; Riaz, S.; Afzal, F. Effect of Heat Treatment on Microstructure and Mechanical Properties of Ti6Al4V Alloy Fabricated by Selective Laser Melting. *J. Mater. Eng. Perform.* **2022**, *32*, 680–694. [CrossRef]
263. Rafi, H.K.; Karthik, N.V.; Gong, H.; Starr, T.L.; Stucker, B.E. Microstructures and Mechanical Properties of Ti6Al4V Parts Fabricated by Selective Laser Melting and Electron Beam Melting. *J. Mater. Eng. Perform.* **2013**, *22*, 3872–3883. [CrossRef]
264. Facchini, L.; Magalini, E.; Robotti, P.; Molinari, A.; Höges, S.; Wissenbach, K. Ductility of a Ti-6Al-4V alloy produced by selective laser melting of prealloyed powders. *Rapid Prototyp. J.* **2010**, *16*, 450–459. [CrossRef]
265. Mertens, A.; Reginster, S.; Paydas, H.; Contrepois, Q.; Dormal, T.; Lemaire, O.; Lecomte-Beckers, J. Mechanical properties of alloy Ti–6Al–4V and of stainless steel 316 L processed by Selective Laser Melting: Influence of out-of-equilibrium microstructures. *Powder Met.* **2014**, *57*, 184–189. [CrossRef]
266. Yang, G.; Cui, B.; Wang, C.; Zhang, Y.; Guo, C.; Wang, C. Compound Structure–Composition Control on the Mechanical Properties of Selective Laser-Melted Titanium Alloys. *Materials* **2022**, *15*, 3125. [CrossRef]
267. Yu, G.; Li, Z.; Hua, Y.; Liu, H.; Zhao, X.; Li, W.; Wang, X. The Effects of Post Heat Treatment on the Microstructural and Mechanical Properties of an Additive-Manufactured Porous Titanium Alloy. *Materials* **2020**, *13*, 593. [CrossRef] [PubMed]
268. Liang, Z.; Sun, Z.; Zhang, W.; Wu, S.; Chang, H. The effect of heat treatment on microstructure evolution and tensile properties of selective laser melted Ti6Al4V alloy. *J. Alloys Compd.* **2018**, *782*, 1041–1048. [CrossRef]
269. Zhao, D.; Han, C.; Li, Y.; Li, J.; Zhou, K.; Wei, Q.; Liu, J.; Shi, Y. Improvement on mechanical properties and corrosion resistance of titanium-tantalum alloys in-situ fabricated via selective laser melting. *J. Alloys Compd.* **2019**, *804*, 288–298. [CrossRef]
270. Zhao, D.; Han, C.; Li, J.; Liu, J.; Wei, Q. In situ fabrication of a titanium-niobium alloy with tailored microstructures, enhanced mechanical properties and biocompatibility by using selective laser melting. *Mater. Sci. Eng. C* **2020**, *111*, 110784. [CrossRef]
271. Liu, Q.; Qiu, C. Variant selection of α precipitation in a beta titanium alloy during selective laser melting and its influence on mechanical properties. *Mater. Sci. Eng. A* **2020**, *784*, 139336. [CrossRef]
272. Nasirpouri, F.; Sanaeian, M.; Samardak, A.; Sukovatitsina, E.; Ognev, A.; Chebotkevich, L.; Hosseini, M.-G.; Abdolmaleki, M. An investigation on the effect of surface morphology and crystalline texture on corrosion behavior, structural and magnetic properties of electrodeposited nanocrystalline nickel films. *Appl. Surf. Sci.* **2014**, *292*, 795–805. [CrossRef]
273. Wang, J.C.; Liu, Y.J.; Qin, P.; Liang, S.X.; Sercombe, T.B.; Zhang, L.C. Selective laser melting of Ti–35Nb composite from elemental powder mixture: Microstructure, mechanical behavior and corrosion behavior. *Mater. Sci. Eng. A* **2019**, *760*, 214–224. [CrossRef]
274. Lu, W.; Liu, Y.; Wu, X.; Liu, X.; Wang, J. Corrosion and passivation behavior of Ti-6Al-4V surfaces treated with high-energy pulsed laser: A comparative study of cast and 3D-printed specimens in a NaCl solution. *Surf. Coat. Technol.* **2023**, *470*, 129849. [CrossRef]
275. Ge, S.-W.; Hu, P.; Deng, J.; Li, S.-L.; Xing, H.-R.; Han, J.-Y.; Hua, X.-J.; Wang, L.; Yang, J.-Z.; Jin, B.; et al. The effect of secondary phase on corrosion behaviors of the titanium–zirconium–molybdenum alloy. *Tungsten* **2024**, *6*, 342–354. [CrossRef]
276. Metalnikov, P.; Ben-Hamu, G.; Eliezer, D. Corrosion behavior of AM-Ti-6Al-4V: A comparison between EBM and SLM. *Prog. Addit. Manuf.* **2022**, *7*, 509–520. [CrossRef]
277. Pede, D.; Li, M.; Virovac, L.; Poleske, T.; Balle, F.; Müller, C.; Mozaffari-Jovein, H. Microstructure and corrosion resistance of novel β-type titanium alloys manufactured by selective laser melting. *J. Mater. Res. Technol.* **2022**, *19*, 4598–4612. [CrossRef]
278. Sharma, A.; Oh, M.C.; Kim, J.-T.; Srivastava, A.K.; Ahn, B. Investigation of electrochemical corrosion behavior of additive manufactured Ti–6Al–4V alloy for medical implants in different electrolytes. *J. Alloys Compd.* **2020**, *830*, 154620. [CrossRef]
279. Zhao, Y.; Wu, C.; Zhou, S.; Yang, J.; Li, W.; Zhang, L.-C. Selective laser melting of Ti-TiN composites: Formation mechanism and corrosion behaviour in H_2SO_4/HCl mixed solution. *J. Alloys Compd.* **2021**, *863*, 158721. [CrossRef]
280. Ju, J.; Li, J.-J.; Jiang, M.; Li, M.-Y.; Yang, L.-X.; Wang, K.-M.; Yang, C.; Kang, M.-D.; Wang, J. Microstructure and electrochemical corrosion behavior of selective laser melted Ti−6Al−4V alloy in simulated artificial saliva. *Trans. Nonferrous Met. Soc. China* **2021**, *31*, 167–177. [CrossRef]
281. Williams, J.C.; Starke, E.A. Progress in structural materials for aerospace systems11The Golden Jubilee Issue—Selected topics in Materials Science and Engineering: Past, Present and Future, edited by Suresh, S. *Acta Mater.* **2003**, *51*, 5775–5799. [CrossRef]
282. Tisza, M.; Czinege, I. Comparative study of the application of steels and aluminium in lightweight production of automotive parts. *Int. J. Light. Mater. Manuf.* **2018**, *1*, 229–238. [CrossRef]
283. Mutua, J.; Nakata, S.; Onda, T.; Chen, Z.-C. Optimization of selective laser melting parameters and influence of post heat treatment on microstructure and mechanical properties of maraging steel. *Mater. Des.* **2018**, *139*, 486–497. [CrossRef]
284. Bajaj, P.; Hariharan, A.; Kini, A.; Kürnsteiner, P.; Raabe, D.; Jägle, E.A. Steels in additive manufacturing: A review of their microstructure and properties. *Mater. Sci. Eng. A* **2020**, *772*, 138633. [CrossRef]

285. Mao, S.; Zhang, D.Z.; Ren, Z.; Fu, G.; Ma, X. Effects of process parameters on interfacial characterization and mechanical properties of 316 L/CuCrZr functionally graded material by selective laser melting. *J. Alloys Compd.* **2022**, *899*, 163256. [CrossRef]
286. Pan, T.; Zhang, X.; Flood, A.; Karnati, S.; Li, W.; Newkirk, J.; Liou, F. Effect of processing parameters and build orientation on microstructure and performance of AISI stainless steel 304 L made with selective laser melting under different strain rates. *Mater. Sci. Eng. A* **2022**, *835*, 142686. [CrossRef]
287. Zhao, Z.; Zhang, L.; Du, W.; Bai, P.; Li, J.; Zhang, W.; Yuan, X. Microstructure and Properties of Porous 17-4PH Stainless Steel Prepared by Selective Laser Melting. *Trans. Indian Inst. Met.* **2022**, *75*, 1641–1648. [CrossRef]
288. Campanelli, S.L.; Santoro, L.; Lamberti, L.; Caiazzo, F.; Alfieri, V. Nonlinear analysis of compressive behavior of 17-4PH steel structures with large spherical pores built by selective laser melting. *J. Mater. Sci.* **2022**, *57*, 3777–3806. [CrossRef]
289. Eskandari, H.; Lashgari, H.; Ye, L.; Eizadjou, M.; Wang, H. Microstructural characterization and mechanical properties of additively manufactured 17–4PH stainless steel. *Mater. Today Commun.* **2021**, *30*, 103075. [CrossRef]
290. Dutt, A.K.; Bansal, G.K.; Tripathy, S.; Krishna, K.G.; Srivastava, V.C.; Chowdhury, S.G. Optimization of Selective Laser Melting (SLM) Additive Manufacturing Process Parameters of 316 L Austenitic Stainless Steel. *Trans. Indian Inst. Met.* **2022**, *76*, 335–345. [CrossRef]
291. Modaresialam, M.; Roozbahani, H.; Alizadeh, M.; Salminen, A.; Handroos, H. In-Situ Monitoring and Defect Detection of Selective Laser Melting Process and Impact of Process Parameters on the Quality of Fabricated SS 316 L. *IEEE Access* **2022**, *10*, 46100–46113. [CrossRef]
292. Wang, F.Z.; Zhang, C.H.; Cui, X.; Zhou, F.Q.; Zhang, S.; Chen, H.T.; Chen, J. Effect of Energy Density on the Defects, Microstructure, and Mechanical Properties of Selective-Laser-Melted 24CrNiMo Low-Alloy Steel. *J. Mater. Eng. Perform.* **2022**, *31*, 3520–3534. [CrossRef]
293. Sufiiarov, V.; Erutin, D.; Kantyukov, A.; Borisov, E.; Popovich, A.; Nazarov, D. Structure, Mechanical and Magnetic Properties of Selective Laser Melted Fe-Si-B Alloy. *Materials* **2022**, *15*, 4121. [CrossRef]
294. Mao, Z.; Lu, X.; Yang, H.; Niu, X.; Zhang, L.; Xie, X. Processing optimization, microstructure, mechanical properties and nanoprecipitation behavior of 18Ni300 maraging steel in selective laser melting. *Mater. Sci. Eng. A* **2021**, *830*, 142334. [CrossRef]
295. Kučerová, L.; Jeníček, Š.; Zetková, I.; Burdová, K. Heat treatment of bimetals produced by selective laser melting of MS1 maraging steel on conventionally produced 42SiCr martensitic steel. *Arch. Civ. Mech. Eng.* **2022**, *22*, 152. [CrossRef]
296. Cruces, A.; Exposito, A.; Branco, R.; Borrego, L.; Antunes, F.; Lopez-Crespo, P. Study of the notch fatigue behaviour under biaxial conditions of maraging steel produced by selective laser melting. *Theor. Appl. Fract. Mech.* **2022**, *121*, 103469. [CrossRef]
297. Bučelis, K.; Škamat, J.; Černašejus, O. Surface laser processing of maraging steel parts manufactured by selective laser melting: Effect on pass geometry and hardness. *IOP Conf. Series Mater. Sci. Eng.* **2022**, *1239*, 012009. [CrossRef]
298. Lei, F.; Wen, T.; Yang, F.; Wang, J.; Fu, J.; Yang, H.; Wang, J.; Ruan, J.; Ji, S. Microstructures and Mechanical Properties of H13 Tool Steel Fabricated by Selective Laser Melting. *Materials* **2022**, *15*, 2686. [CrossRef] [PubMed]
299. Ferreira, D.F.; Vieira, J.S.; Rodrigues, S.; Miranda, G.; Oliveira, F.J.; Oliveira, J.M. Dry sliding wear and mechanical behaviour of selective laser melting processed 18Ni300 and H13 steels for moulds. *Wear* **2022**, *488–489*, 204179. [CrossRef]
300. Leo, P.; D'ostuni, S.; Perulli, P.; Sastre, M.A.C.; Fernández-Abia, A.I.; Barreiro, J. Analysis of microstructure and defects in 17-4 PH stainless steel sample manufactured by Selective Laser Melting. *Procedia Manuf.* **2019**, *41*, 66–73. [CrossRef]
301. Tekkaya, A.; Allwood, J.; Bariani, P.; Bruschi, S.; Cao, J.; Gramlich, S.; Groche, P.; Hirt, G.; Ishikawa, T.; Löbbe, C.; et al. Metal forming beyond shaping: Predicting and setting product properties. *CIRP Ann.* **2015**, *64*, 629–653. [CrossRef]
302. Hu, Z.; Chen, F.; Xu, J.; Ma, Z.; Guo, H.; Chen, C.; Nian, Q.; Wang, X.; Zhang, M. Fabricating graphene-titanium composites by laser sintering PVA bonding graphene titanium coating: Microstructure and mechanical properties. *Compos. Part B Eng.* **2018**, *134*, 133–140. [CrossRef]
303. Leo, P.; Cabibbo, M.; Del Prete, A.; Giganto, S.; Martínez-Pellitero, S.; Barreiro, J. Laser Defocusing Effect on the Microstructure and Defects of 17-4PH Parts Additively Manufactured by SLM at a Low Energy Input. *Metals* **2021**, *11*, 588. [CrossRef]
304. Hemmati, I.; Ocelík, V.; De Hosson, J.T.M. Microstructural characterization of AISI 431 martensitic stainless steel laser-deposited coatings. *J. Mater. Sci.* **2011**, *46*, 3405–3414. [CrossRef]
305. Nagay, B.E.; Cordeiro, J.M.; Barão, V.A.R. Alloy Materials for Biomedical Applications. *Alloy Mater. Their Allied Appl.* **2020**, 159–189. [CrossRef]
306. Papula, S.; Song, M.; Pateras, A.; Chen, X.-B.; Brandt, M.; Easton, M.; Yagodzinskyy, Y.; Virkkunen, I.; Hänninen, H. Selective Laser Melting of Duplex Stainless Steel 2205: Effect of Post-Processing Heat Treatment on Microstructure, Mechanical Properties, and Corrosion Resistance. *Materials* **2019**, *12*, 2468. [CrossRef]
307. Maurya, A.K.; Pandey, C.; Chhibber, R. Dissimilar welding of duplex stainless steel with Ni alloys: A review. *Int. J. Press. Vessel. Pip.* **2021**, *192*, 104439. [CrossRef]
308. Sarkar, S.; Mukherjee, S.; Kumar, C.S.; Nath, A.K. Effects of heat treatment on microstructure, mechanical and corrosion properties of 15-5 PH stainless steel parts built by selective laser melting process. *J. Manuf. Process.* **2020**, *50*, 279–294. [CrossRef]
309. Wang, C.-J.; Liu, C.; Zhang, M.-X.; Jiang, L.; Liu, Y.; Liu, Z.-B.; Liang, J.-X. Effect of Yttrium on the Microstructure and Mechanical Properties of PH13-8Mo Stainless Steels Produced by Selective Laser Melting. *Materials* **2022**, *15*, 5441. [CrossRef]
310. Sripada, J.; Tian, Y.; Chadha, K.; Saha, G.; Jahazi, M.; Spray, J.; Aranas, C. Effect of hot isostatic pressing on microstructural and micromechanical properties of additively manufactured 17–4PH steel. *Mater. Charact.* **2022**, *192*, 112174. [CrossRef]

311. Zhang, H.; Li, C.; Xu, M.; Dai, W.; Kumar, P.; Liu, Z.; Li, Z.; Zhang, Y. The fatigue performance evaluation of additively manufactured 304 L austenitic stainless steels. *Mater. Sci. Eng. A* **2020**, *802*, 140640. [CrossRef]
312. Zhai, W.; Zhou, W.; Zhu, Z.; Nai, S.M.L.; Mui, S.; Nai, L. Selective Laser Melting of 304 L and 316 L Stainless Steels: A Comparative Study of Microstructures and Mechanical Properties. *Steel Res. Int.* **2022**, *93*, 2100664. [CrossRef]
313. Ozsoy, A.; Aydogan, E.; Dericioglu, A.F. Selective laser melting of Nano-TiN reinforced 17-4 PH stainless steel: Densification, microstructure and mechanical properties. *Mater. Sci. Eng. A* **2022**, *836*, 142574. [CrossRef]
314. Lecis, N.; Beltrami, R.; Mariani, M. Binder jetting 3D printing of 316 stainless. steel: Influence of process parameters on microstructural and mechanical properties. *La Metall. Ital.* **2021**, *113*, 31–41.
315. Lv, B.; Wang, F.; Niu, X.; Zhang, L.; Wu, X.; Lai, Y.; Hong, B.; Cao, S. In-situ formed graded microstructure and mechanical property of selective laser melted 15–5 PH stainless steel. *Mater. Sci. Eng. A* **2022**, *847*, 143340. [CrossRef]
316. Zeng, F.; Yang, Y.; Qian, G. Fatigue properties and S-N curve estimating of 316 L stainless steel prepared by SLM. *Int. J. Fatigue* **2022**, *162*, 106946. [CrossRef]
317. Zhou, B.; Xu, P.; Li, W.; Liang, Y.; Liang, Y. Microstructure and Anisotropy of the Mechanical Properties of 316 L Stainless Steel Fabricated by Selective Laser Melting. *Metals* **2021**, *11*, 775. [CrossRef]
318. Garcia-Cabezon, C.; Castro-Sastre, M.A.; Fernandez-Abia, A.I.; Rodriguez-Mendez, M.L.; Martin-Pedrosa, F. Microstructure–Hardness–Corrosion Performance of 17–4 Precipitation Hardening Stainless Steels Processed by Selective Laser Melting in Comparison with Commercial Alloy. *Met. Mater. Int.* **2022**, *28*, 2652–2667. [CrossRef]
319. Tan, Q.; Yin, Y.; Wang, F.; Chang, H.; Liu, S.; Liang, G.; Wu, T.; Zhang, M.-X. Rationalization of brittleness and anisotropic mechanical properties of H13 steel fabricated by selective laser melting. *Scr. Mater.* **2022**, *214*, 114645. [CrossRef]
320. Bai, Y.; Zhao, C.; Zhang, Y.; Wang, H. Microstructure and mechanical properties of additively manufactured multi-material component with maraging steel on CrMn steel. *Mater. Sci. Eng. A* **2020**, *802*, 140630. [CrossRef]
321. Boes, J.; Röttger, A.; Mutke, C.; Escher, C.; Theisen, W. Microstructure and mechanical properties of X65MoCrWV3-2 cold-work tool steel produced by selective laser melting. *Addit. Manuf.* **2018**, *23*, 170–180. [CrossRef]
322. Geenen, K.; Röttger, A.; Feld, F.; Theisen, W. Microstructure, mechanical, and tribological properties of M3:2 high-speed steel processed by selective laser melting, hot-isostatic pressing, and casting. *Addit. Manuf.* **2019**, *28*, 585–599. [CrossRef]
323. An, W.; Park, J.; Lee, J.; Choe, J.; Jung, I.D.; Yu, J.-H.; Kim, S.; Sung, H. Correlation between Microstructure and Mechanical Properties of the Additive Manufactured H13 Tool Steel. *Korean J. Mater. Res.* **2018**, *28*, 663–670. [CrossRef]
324. Zhang, Y.; Song, B.; Ming, J.; Yan, Q.; Wang, M.; Cai, C.; Zhang, C.; Shi, Y. Corrosion mechanism of amorphous alloy strengthened stainless steel composite fabricated by selective laser melting. *Corros. Sci.* **2020**, *163*, 108241. [CrossRef]
325. Alnajjar, M.; Christien, F.; Barnier, V.; Bosch, C.; Wolski, K.; Fortes, A.D.; Telling, M. Influence of microstructure and manganese sulfides on corrosion resistance of selective laser melted 17-4 PH stainless steel in acidic chloride medium. *Corros. Sci.* **2020**, *168*, 108585. [CrossRef]
326. Laleh, M.; Hughes, A.E.; Yang, S.; Li, J.; Xu, W.; Gibson, I.; Tan, M.Y. Two and three-dimensional characterisation of localised corrosion affected by lack-of-fusion pores in 316 L stainless steel produced by selective laser melting. *Corros. Sci.* **2020**, *165*, 108394. [CrossRef]
327. Li, N.; Zhang, W.; Xu, H.; Cai, Y.; Yan, X. Corrosion Behavior and Mechanical Properties of 30CrMnSiA High-Strength Steel under an Indoor Accelerated Harsh Marine Atmospheric Environment. *Materials* **2022**, *15*, 629. [CrossRef] [PubMed]
328. Zhou, C.; Hu, S.; Shi, Q.; Tao, H.; Song, Y.; Zheng, J.; Xu, P.; Zhang, L. Improvement of corrosion resistance of SS316L manufactured by selective laser melting through subcritical annealing. *Corros. Sci.* **2020**, *164*, 108353. [CrossRef]
329. Loh, L.-E.; Chua, C.-K.; Yeong, W.-Y.; Song, J.; Mapar, M.; Sing, S.-L.; Liu, Z.-H.; Zhang, D.-Q. Numerical investigation and an effective modelling on the Selective Laser Melting (SLM) process with aluminium alloy 6061. *Int. J. Heat Mass Transf.* **2015**, *80*, 288–300. [CrossRef]
330. Illies, O.; Li, G.; Jürgens, J.-P.; Ploshikhin, V.; Herzog, D.; Emmelmann, C. Numerical modelling and experimental validation of thermal history of titanium alloys in laser beam melting. *Procedia CIRP* **2018**, *74*, 92–96. [CrossRef]
331. Khan, K.; De, A. Modelling of selective laser melting process with adaptive remeshing. *Sci. Technol. Weld. Join.* **2019**, *24*, 391–400. [CrossRef]
332. Favoretto, B.; de Hillerin, C.; Bettinotti, O.; Oancea, V.; Barbarulo, A. Reduced order modeling via PGD for highly transient thermal evolutions in additive manufacturing. *Comput. Methods Appl. Mech. Eng.* **2019**, *349*, 405–430. [CrossRef]
333. Alexopoulou, V.E.; Papazoglou, E.L.; Karmiris-Obratański, P.; Markopoulos, A.P. 3D finite element modeling of selective laser melting for conduction, transition and keyhole modes. *J. Manuf. Process.* **2022**, *75*, 877–894. [CrossRef]
334. Sani, I.; Auricchio, F. Selective Laser Melting Process Simulation: Advancements towards a Cost-Effective Model. PhD. Thesis, Istituto Universitario di Studi Superiori di Pavia, Pavia, Italy, 2017. Available online: https://compmech.unipv.it/wp-content/uploads/2020/10/sani_phd.pdf (accessed on 28 July 2024).
335. Frostevarg, J.; Volpp, J.; Thompson, C.; Prasad, H.S.; Fedina, T.; Brückner, F. Influence of the vapour channel on processing in laser powder bed fusion. *Procedia Manuf.* **2019**, *36*, 80–87. [CrossRef]
336. Ganeriwala, R.; Zohdi, T.I. Multiphysics modeling and simulation of selective laser sintering manufacturing processes. *Procedia CIRP* **2014**, *14*, 299–304. [CrossRef]
337. Soylemez, E.; Koç, E.; Coşkun, M. Thermo-mechanical simulations of selective laser melting for AlSi10Mg alloy to predict the part-scale deformations. *Prog. Addit. Manuf.* **2019**, *4*, 465–478. [CrossRef]

338. Yin, J.; Zhu, H.; Ke, L.; Lei, W.; Dai, C.; Zuo, D. Simulation of temperature distribution in single metallic powder layer for laser micro-sintering. *Comput. Mater. Sci.* **2012**, *53*, 333–339. [CrossRef]
339. Ghnatios, C.; El Rai, K.; Hascoet, N.; Pires, P.-A.; Duval, J.-L.; Lambarri, J.; Hascoet, J.-Y.; Chinesta, F. Reduced order modeling of selective laser melting: From calibration to parametric part distortion. *Int. J. Mater. Form.* **2021**, *14*, 973–986. [CrossRef]
340. GuoMing, H.; Jian, Z.; JianQang, L. Dynamic simulation of the temperature field of stainless steel laser welding. *Mater. Des.* **2007**, *28*, 240–245. [CrossRef]
341. Rajan, A.N.R.; Krochmal, M.; Wegener, T.; Biswas, A.; Hartmaier, A.; Niendorf, T.; Moeini, G. Micromechanical Modeling of AlSi10Mg Processed by Laser-Based Additive Manufacturing: From as-Built to Heat-Treated Microstructures. *Materials* **2022**, *15*, 5562. [CrossRef] [PubMed]
342. Sun, S.; Zheng, L.; Liu, Y.; Liu, J.; Zhang, H. Selective laser melting of Al-Fe-V-Si heat-resistant aluminum alloy powder: Modeling and experiments. *Int. J. Adv. Manuf. Technol.* **2015**, *80*, 1787–1797. [CrossRef]
343. Song, B.; Dong, S.; Liao, H.; Coddet, C. Process parameter selection for selective laser melting of Ti6Al4V based on temperature distribution simulation and experimental sintering. *Int. J. Adv. Manuf. Technol.* **2012**, *61*, 967–974. [CrossRef]
344. Deng, C.; Zhang, Y.P.; Gao, J.C. Numerical simulation of temperature field for bioceramic coating cladded by laser. *J. Mater. Sci. Eng.* **2003**, *21*, 503–506.
345. Markl, M.; Körner, C. Multiscale Modeling of Powder Bed–Based Additive Manufacturing. *Annu. Rev. Mater. Res.* **2016**, *46*, 93–123. [CrossRef]
346. Li, C.-J.; Tsai, T.-W.; Tseng, C.-C. Numerical simulation for heat and mass transfer during selective laser melting of titanium alloys powder. *Phys. Procedia* **2016**, *83*, 1444–1449. [CrossRef]
347. Panwisawas, C.; Qiu, C.; Anderson, M.J.; Sovani, Y.; Turner, R.P.; Attallah, M.M.; Brooks, J.W.; Basoalto, H.C. Mesoscale modelling of selective laser melting: Thermal fluid dynamics and microstructural evolution. *Comput. Mater. Sci.* **2017**, *126*, 479–490. [CrossRef]
348. Yang, J.; Yu, H.; Yang, H.; Li, F.; Wang, Z.; Zeng, X. Prediction of Microstructure in Selective Laser Melted Ti 6Al 4V Alloy by Cellular Automaton. *J. Alloys Compd.* **2018**, *748*, 281–290. [CrossRef]
349. Rappaz, M. Modelling of microstructure formation in solidification processes. *Int. Mater. Rev.* **1989**, *34*, 93–124. [CrossRef]
350. Dezfoli, A.R.A.; Hwang, W.-S.; Huang, W.-C.; Tsai, T.-W. Determination and controlling of grain structure of metals after laser incidence: Theoretical approach. *Sci. Rep.* **2017**, *7*, 41527. [CrossRef]
351. Ping, W.S.; Rong, L.D.; Jie, G.J.; Yun, L.C.; Qing, S.Y.; Zhi, F.H. Numerical simulation of microstructure evolution of Ti-6Al-4V alloy in vertical centrifugal casting. *Mater. Sci. Eng. A* **2006**, *426*, 240–249. [CrossRef]
352. Vrancken, B.; Thijs, L.; Kruth, J.-P.; Van Humbeeck, J. Microstructure and mechanical properties of a novel β titanium metallic composite by selective laser melting. *Acta Mater.* **2014**, *68*, 150–158. [CrossRef]
353. Simonelli, M.; Tse, Y.Y.; Tuck, C. On the Texture Formation of Selective Laser Melted Ti-6Al-4V. *Met. Mater. Trans. A* **2014**, *45*, 2863–2872. [CrossRef]
354. Ahmad, B.; van der Veen, S.O.; Fitzpatrick, M.E.; Guo, H. Residual stress evaluation in selective-laser-melting additively manufactured titanium (Ti-6Al-4V) and inconel 718 using the contour method and numerical simulation. *Addit. Manuf.* **2018**, *22*, 571–582. [CrossRef]
355. Shu, Y.; Galles, D.; Tertuliano, O.A.; McWilliams, B.A.; Yang, N.; Cai, W.; Lew, A.J. A critical look at the prediction of the temperature field around a laser-induced melt pool on metallic substrates. *Sci. Rep.* **2021**, *11*, 12224. [CrossRef]
356. Ansari, P.; Rehman, A.U.; Pitir, F.; Veziroglu, S.; Mishra, Y.K.; Aktas, O.C.; Salamci, M.U. Selective Laser Melting of 316 L Austenitic Stainless Steel: Detailed Process Understanding Using Multiphysics Simulation and Experimentation. *Metals* **2021**, *11*, 1076. [CrossRef]
357. Zhang, Z.; Huang, Y.; Kasinathan, A.R.; Shahabad, S.I.; Ali, U.; Mahmoodkhani, Y.; Toyserkani, E. 3-Dimensional heat transfer modeling for laser powder-bed fusion additive manufacturing with volumetric heat sources based on varied thermal conductivity and absorptivity. *Opt. Laser Technol.* **2019**, *109*, 297–312. [CrossRef]
358. Liu, S.; Zhu, H.; Peng, G.; Yin, J.; Zeng, X. Microstructure prediction of selective laser melting AlSi10Mg using finite element analysis. *Mater. Des.* **2018**, *142*, 319–328. [CrossRef]